NTNU

Norwegian University of
Science and Technology

Design and fabrication of micro-nano enhanced surfaces for controlling Leidenfrost point

Eivind Grøstad

EPT-M-2016-46

MASTER THESIS

for

Student
Eivind Grøstad

Spring 2016

Design and fabrication of micro-nano enhanced surfaces for controlling Leidenfrost point

Design og fabrikasjon av mikro konstruerte overflater for kontroll av Leidenfrost punktet

Background and objective

The need for high heat flux removal has been triggered by the development of new technologies ranging from computers, data centers, medical applications, electric cars, radars, satellite and lasers, to mention some applications. Today it is recognized that manufacturability is not the limiting factor with regards to the small size of the devices, and that the major challenge is the power dissipation problem, i.e. how to remove the heat from a confined space. Spray cooling is being considering a possible solution for cooling of high heat fluxes system such as of diode array, large radar and laser transmitters because it allows a low superheat, no temperature overshoot, no contact thermal resistance, less flow rate demand.

The main objective in this work is to identify and fabricate structures for enhancing the Leidenfrost point. The secondary objective is to design and fabricate a test facility for studying impacting droplet over a micro-nano structure surface.

The following tasks are to be considered:

1. Identify optimal structures to enhance Leidenfrost point from published literature
2. Identify the essential aspects to successfully fabricate the optimal structures
3. Develop a fabrication method for micro pillars
4. Develop a fabrication method for cones and exploit its dimensional limits
5. Identify a convenient fabrication method for carbon nanowires
6. Develop a fabrication method for a hierarchical structure
7. Identify the wetting characteristics of the hierarchical structure
8. Design and fabricate a test facility for studying impacting droplet over a micro-nano structure surface

-- " --

Within 14 days of receiving the written text on the master thesis, the candidate shall submit a research plan for his project to the department.

When the thesis is evaluated, emphasis is put on processing of the results, and that they are presented in tabular and/or graphic form in a clear manner, and that they are analyzed carefully.

The thesis should be formulated as a research report with summary both in English and Norwegian, conclusion, literature references, table of contents etc. During the preparation of the text, the candidate should make an effort to produce a well-structured and easily readable report. In order to ease the evaluation of the thesis, it is important that the cross-references are correct. In the making of the report, strong emphasis should be placed on both a thorough discussion of the results and an orderly presentation.

The candidate is requested to initiate and keep close contact with his/her academic supervisor(s) throughout the working period. The candidate must follow the rules and regulations of NTNU as well as passive directions given by the Department of Energy and Process Engineering.

Risk assessment of the candidate's work shall be carried out according to the department's procedures. The risk assessment must be documented and included as part of the final report. Events related to the candidate's work adversely affecting the health, safety or security, must be documented and included as part of the final report. If the documentation on risk assessment represents a large number of pages, the full version is to be submitted electronically to the supervisor and an excerpt is included in the report.

Pursuant to "Regulations concerning the supplementary provisions to the technology study program/Master of Science" at NTNU §20, the Department reserves the permission to utilize all the results and data for teaching and research purposes as well as in future publications.

The final report is to be submitted digitally in DAIM. An executive summary of the thesis including title, student's name, supervisor's name, year, department name, and NTNU's logo and name, shall be submitted to the department as a separate pdf file. Based on an agreement with the supervisor, the final report and other material and documents may be given to the supervisor in digital format.

X Work to be done in lab (Water power lab, Fluids engineering lab, Thermal engineering lab)
☐ Field work

Department of Energy and Process Engineering, 13. January 2016

Olav Bolland
Department Head

Carlos A. Dorao
Academic Supervisor

Research Advisor:
Espen Rogstad
Il-Woong Park
Manuel Auliano

Acknowledgement

E.G.

iv

Preface

This thesis is the result of my work performed the spring of 2016 to earn the degree of Master of Science in environmental and energy engineering at the Norwegian University of Science and Technology (NTNU) in Trondheim. My supervisor during this work has been Carlos A. Dorao, and my research advisors have been Espen Rogstad, Il-Woong Park and Manuel Auliano.

The topic of this master thesis is an experimental study of design and fabrication of micro-nano surfaces with the goal of controlling the Leidenfrost point, a subject of study important for e.g. the future cooling of small size electronic equipment.

This master thesis is a continuation of my specialization project, which I conducted during the fall of 2015. The thesis has been built on both a literature study, including a part based on the theoretical and experimental work from the specialization project along with experimental work performed during the semester.

Trondheim, 10.06.2016

Eivind Grøstad

eivind.grostad@gmail.com

Summary

The technological revolution has driven the need for faster microprocessors. In order to fabricate faster microprocessors the trend has been to increase the amount of transistors and increase the clock speed. Microprocessor clock speed reached a point of saturation in 2006 because of the thermal challenges related to the transistors. As microprocessor power densities are increasing beyond air cooling limits, liquid cooling will become necessary. Spray cooling turn out to be the best candidate.

Spray cooling have shown the ability to remove large amounts of energy due to latent heat of evaporation in addition to single-phase convection effects at low operational temperatures. A fundamental drawback with spray cooling is the limit of operation temperature due to the Leidenfrost effect, a vapour cushion forming in between the liquid and the solid and hence a spontaneous reduction in heat transfer. It is therefore essential to understand how to control at which temperature the Leidenfrost effect occur. Engineered micro-nano structures have shown the capability to manipulate the Leidenfrost point.

The main objective in this work is to identify and fabricate structures for enhancing the Leidenfrost point. The secondary objective is to design and fabricate a test facility for studying impacting droplet over a micro-nano structure surface.

In this work optimal structures for enhancing the Leidenfrost point have been identified from the literature. Techniques for fabricating the selected structures have been carried out and the structures have been characterized by available equipment at the NTNU Nanolab. Micro pillars, micro cones, Carbon nanowires and a hierarchical combination of small and big scale structures of the same type have been developed. In addition, a hierarchical combination of Carbon nanowires and micro cones. Furthermore, design and fabrication of a test section for studying impacting droplets over a micro-nano structure surface has been completed.

Important results uncovered in this work are the following. Helium flow rate has been identified as an essential tool for post fabrication analysis of the etching process and the

height limit of the cone fabrication has been revealed. Anomalous wetting characteristics has been identified for a sample with hierarchical structures consisting of two cones of different scale.

This work has shown that lithography and deep reactive ion etching have the ability to fabricate surfaces with controllable structures to enhance the characteristics of the surface. Such structures will help to improve the understanding of how surface structures can enhance the Leidenfrost point. Spray cooling as a possible candidate for liquid cooling of microprocessors and other devices with high heat flux and restrictions on operational temperature is strengthened.

Sammendrag

Den teknologiske revolusjonen har drevet et behov for raskere mikroprosessorer. For å utvikle raskere mikroprosessorer har trenden vært å øke antallet transistorer og øke klokkefrekvens. Klokkefrekvensen nådde et tak i 2006 som følge av termiske utfordringer knyttet til transistorene. Når effekttettheten blir høyere enn egenskapene til luft blir det helt nødvendig med kjøling ved bruk av væske. Spray-kjøling har vist seg å være den beste kandidaten.

Spray-kjøling har vist evne til å fjerne store mengder energi ved latent fordampningsvarme i tillegg til enfase konveksjonseffekter ved lave driftstemperaturer. En fundamental bakside med spray-kjøling er begrensningen på driftstemperatur på grunn av Leidenfrost effekten, et dampteppe som former seg mellom væsken og overflaten, og dermed spontant reduserer varmetransporten. Det er derfor viktig å forstå hvordan man kan kontrollere når dette skjer. Overflater med konstruerte mikrostrukturer har vist seg å kunne manipulere nettopp dette.

Denne oppgaven tar for seg å identifisere og fabrikkere optimale strukturer for å øke Leidenfrost punktet. Sekundært skal det designes og fabrikkeres et instrument for å kunne studere dråper som treffer en slik optimal overflate.

I denne oppgaven har optimale strukturer for å øke Leidenfrost punktet blitt identifisert fra tilgjengelig publisert litteratur. Teknikker for fabrikasjon av de utvalgte strukturene har blitt utviklet og strukturene har blitt karakterisert ved hjelp av tilgjengelig utstyr på Nanolaben ved NTNU. Mikrosøyler, mikrokjegler, karbon nanotråder og en hierarkisk kombinasjon av liten- og stor-skala strukturer av samme type har blitt utviklet. I tillegg har det blitt utviklet en hierarkisk kombinasjon av karbon nanotråder og mikrokjegler. Videre har design og fabrikasjon av en testseksjon for studering av dråper som treffer en mikro-nano strukturert overflate blitt fullført.

Viktige resultater oppdaget i dette arbeidet er som følger. Strømningshastigheten til helium har blitt identifisert som et viktig verktøy for analyse av etseprosesse. Unormale

fukteegenskaper har blitt identifisert for en prøve bestående av hierarkisk kombinasjon av strukturer av to forskjellige kjegle størrelser.

Dette arbeider har vist at litografi og dyp reaktiv ioneetsing muliggjør fabrikasjon av overflater med kontrollerbare strukturer som forbedrer egenskapene til overflaten. Slike strukturer vil bistå forståelsen for hvordan slike overflate strukturer kan forbedre Leidenfrost punktet. Spray-kjøling som en mulig kandidat for væskekjøling av mikroprosessorer og andre objekter med høy varmefluks og med restriksjoner på operasjonell temperatur er styrket.

Table of Contents

List of Tables

List of Figures

List of Symbols

A_p Projected surface

A_t Top surface

A_a Actual surface

P   Pitch, micro level

D   Diameter/Width, micro level

H   Height, micro level

θ Apparent observed contact angle

θ_e Chemical angle / Youngs angle / Intrinsic contact angle / Equilibrium contact angle

θ_c Critical Contact Angle

θ_W Wenzel angle

θ_C Cassie-Baxter angle

f   Contact surface fraction

r   Surface roughness

We   Weber number

Nomenclature

TCL	=	Triple-phase Contact Line
sccm	=	Standard cubic centimeter per minute
mTorr	=	Milli Torr
CA	=	Contact Angle
CAH	=	Contact Angle Hysteresis
LFP	=	Leidenfrost Point
LP	=	Leidenfrost Phenomenon
IPA	=	Isopropyl Alcohol / Isopropanol
CTE	=	Coefficient of Thermal Expansion
DRIE	=	Deep Reactive Ion Etching
TIM	=	Thermal Interface Material
S	=	Spreading Parameter
EDS	=	Energy-Dispersive x-ray Spectroscopy
FIB	=	Focused Ion Beam
ICP	=	Inductively Coupled Plasma
SEM	=	Scanning Electron Microscope
ER	=	Etching Rate
DI	=	De-Ionized
fps	=	Frames per second
EBL	=	Electron-Beam Lithography

1. Introduction

1.1 Background and Motivation

The technological revolution has driven the need for faster microprocessors. In order to fabricate faster microprocessors the trend has been to increase the amount of transistors, from 2300 in Intel's first microprocessor, Intel 4004 (1971), to 3 billion transistors in 2015 (A8X) and increase the clock speed, i.e. the frequency, see Figure 1.1a and Figure 1.2. Microprocessor clock speed reached a point of saturation in 2006 at about 3.8 GHz because of the thermal challenges related to the transistors. A transistor has a peak temperature of 80 - 100°C [19] and the mean time to failure decreases exponentially with operation temperature [20]. With a thermal design power, TDP, above 115W for Pentium 4, see Figure 1.1b, it became a challenge to keep the transistors below peak temperature. The

(a)   (b)

Figure 1.1: (a) Intel Processor Clock Speed (MHz) i.e. frequency evolution over time [1]. X-axis in years and y-axis in logarithmic Mega Hertz. (b) Power consumption trends in microprocessors. TPD, Thermal Design Power. Graph from Intel.

limit of the frequency led to a inevitable shift in paradigm for microprocessors. Instead
of increasing clock speed, increase in the number of cores, multicore systems, became the
solution. In a multicore system the performance increase is achieved by increasing the
number of microprocessors and optimizing the usage of them by software. The develop-
ment of multicore systems cannot proceed forever due to the limit of the transistor size.
The transistor gate has gone from 10 μm to 14 nm, and is reaching the physical limit. The
length scale reduction increase leakage voltage, hence the heat dissipation and further-
more the temperature of the transistor. The world society are dependent on a continuously

| (a) | (b) |

Figure 1.2: (a) The Original Moore´s Law of Intel Processors [2]. (b) 2014 edition of
Moore´s Law of Intel Processors [3].

development in all academic disciplines and ever more complex challenges require con-
tinuously increasing computer power. Moreover, the technological evolution is dependent
on a thermal solution. Advanced flight systems such as laser-diode arrays and multi-chip
modules is required for future space exploration programs. High heat flux cooling ca-
pability, $\geqslant 100 W cm^{-2}$, is required for thermal management of these systems. Improved
thermal management, dense system packaging and reduced weight has gained substantial
attention in the military sector. Applications such as high power microwave systems, high
energy lasers and high power radar systems are dependent on a feasible thermal solution
to become available for mobile platforms [21].

High energy diode laser-pumped solid state lasers and weapons have been especially
popular the latest years [22]. With diode laser pumping, compact and high efficiency

(a)	(b)	(c)

Figure 1.3: (a) Laser Diode array from the Lawrence Livermore National Laboratory HAPLS project [4]. (b) S15 - QCW Laser Diode from Lasertel [5]. (c) Spray cooling concept[6].

lasers in an all solid-state device is possible to fabricate. Advantages such as narrower frequency linewidth, better beam quality, higher peak powers and different wavelengths is a consequence [22]. The diode laser-pump contains several arrays of diodes like the one from Lasertel in Figure 1.3b. National Aeronautics and Space Administration and their Lidar missons have expressed their interest in this area several times [23]. U.S. Navy has deployed a 30 kW fibre solid state laser on the ship *USS Ponce* [24]. Boeing has developed a High Energy Laser Mobile Demonstrator, 10 kW fibre solid state laser, for the U.S. Army [25] and Lockheed Martin developed a Area Defense Anti-Munitions system in 2014 [26], an Advanced Test High Energy Asset, 30 kW fibre solid state laser weapon in 2015 [27] and is currently been testing a platform for aircrafts [28]. Initially the goal was to develop a megawatt laser weapon during the cold war. A megawatt laser weapon became never a reality. Now the goal is in the kilowatt range, 100 - 300 kW.

Lawrence Livermore has become the global leader in design and operation of high energy and high power lasers since the founding of its laser program in the 1970s. Lawrence Livermore National Laboratory deployed world's highest peak-power laser diode arrays in 2015, see Figure 1.3a, with a total peak power of 3.2MW. [4].

All the high energy laser systems mentioned require laser diode arrays with increasing peak power. As the peak power increase new cooling technology will be necessary, especially for space limited applications.

1.2 Problem Formulation

As power densities are increasing beyond air cooling limits, $O(h)$ ~$100 W m^{-2} k^{-1}$, up to $20\ W cm^{-2}$ with heat sink, liquid cooling will become necessary. Several different liquid cooling methods have been proposed, e.g. microchannel liquid cooling, immersion flow boiling, spray cooling, jet impingment cooling, thermosyphons and heat pipes. Spray cooling, see concept Figure 1.3c, turn out to deliver the best combination of heat flux, isothermality and fluid inventory [29]. Tilton et al and Konpchikov et al demonstrated heat fluxes greater than $1000 W cm^{-2}$ and $500 W cm^{-2}$ already in 1989 and 1968 respectively with the spray cooling concept [30] [31].

Additionally, spray cooling has advantages such as low superheat, no temperature overshoot, no contact thermal resistance, less flow rate demand and spray cooling has become the preferred solution in thermal control of diode arrays, large radar and laser transmitters [32]. The spray cooling technology has been applied in supercomputers, i.e. Cray X1/SV2, and spacecraft with success and is sold as a commercial product from, among others, Parker Aerospace Inc. [29, 33, 21, 34, 23]
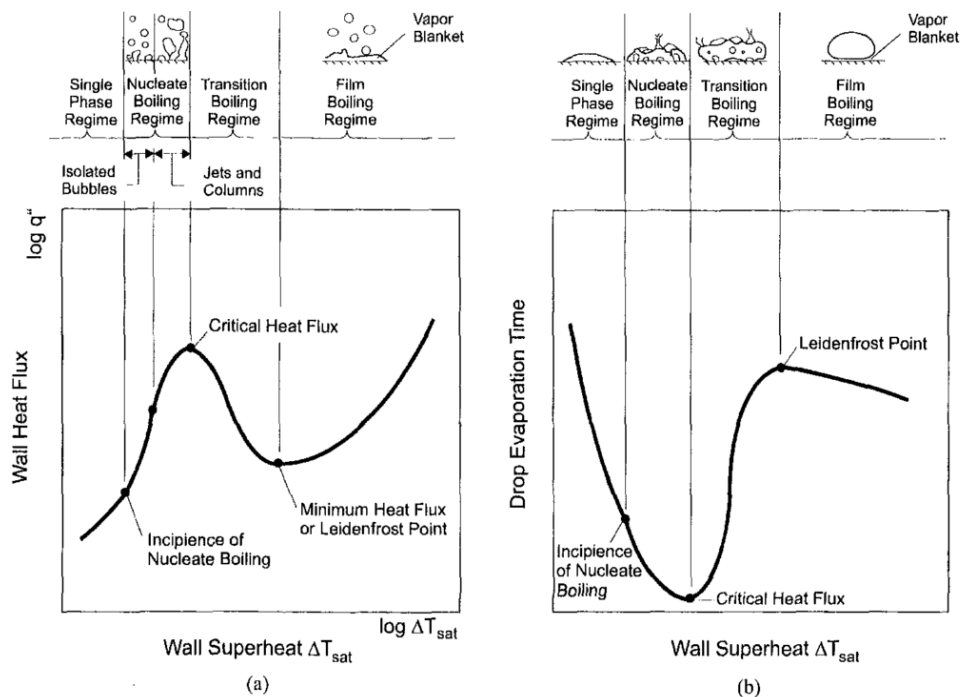
Figure 1.4: Leiden Frost Point [7].

In Figure 1.4(a), the typical pool boiling curve with four recognizable heat transfer regimes can be seen. Figure 1.4(b) displays a droplet evaporation lifetime versus surface temperature. Spray cooling occurs when a dispersion of fine droplets impact a heated surface with a low impact velocity. The droplets evaporate immediately or form a thin film, dependent on the characterisation of the surface and the temperature. The droplets can remove large amounts of energy due to latent heat of evaporation in addition to single-phase convection effects [29]. The mechanisms by which heat is removed during spray cooling is rather complex due to its dependence on many dependent parameters and they are therefore not further discussed here. The reader is refereed to [29] and [32].

However, the optimal heat transfer occurs at the critical heat flux (CHF), Figure 1.4 and when the surface temperature goes beyond the Leidenfrost Point (LFP), the droplets hovers ~100 μm above the surface and the contact with the surface is lost due to a vapor layer between the surface and the droplet i.e. film boiling [35]. At LFP the cooling is ineffective due to the vapor layer, the heat flux is at a minimum. Hence controlling at which temperature the leidenfrost effect occurs and further at which temperature heat flux is maximum is the problem one will find an answer to. Recent studies have identified the importance of surface roughness, surface wettability and surface contact fraction on controlling the Leidenfrost temperature. Development in fabrication techniques and equipment have made micro fabrication of structures on a surface for custom roughness and surface contact fraction by photolithography and deep etching, popular.

1.3 Goal and Objectives

The long term goal in the field of research is to understand the relationship between micro-nano enhanced surfaces and the temperature at the Leidenfrost point. The main objective in this work is to identify and fabricate structures for enhancing the Leidenfrost point. The secondary objective is to design and fabricate a test facility for studying impacting droplet over a micro-nano structure surface.

The following main tasks are to be considered in this work:

I. Identify optimal structures to enhance Leidenfrost point from published literature

II. Identify the essential aspects to successfully fabricate the optimal structures

III. Develop a fabrication method for micro pillars

IV. Develop a fabrication method for cones and exploit its dimensional limits

V. Identify a convenient fabrication method for Carbon nanowires

VI. Develop a fabrication method for a hierarchical structure

VII. Identify the wetting characteristics of the hierarchical structure

VIII. Design and fabricate a test facility for studying impacting droplet over a micro-nano structure surface

In task I a review of previous results in the research area was presented. In particular "Leidenfrost Phenomenon on Textured Surfaces", "Wettability on Textured Surfaces" and "Anisotropic Wettability". The optimal structures to enhance Leidenfrost point are concluded in Chapter 3.

For task II intensive training hosted NTNU Nanolab as required to operate the necessary equipment in the NTNU Cleanroom is carried out, best-practice and experience from

technical staff and other experienced users of the same instruments are transferred, literature of the process is reviewed and experiments are performed to gain knowledge and experience.

The skills necessary to fabricate the surface structures required to do task VI are developed stepwise by mastering the fabrication of cylindrical pillars (III), cones (IV), wires (V) and finally a combination of scale: micro and nano together. The precision for fabrication success is vital for solving the challenge. The need to attack the objective with stepwise progression is therefore absolute.

Task VII is done by testing samples from task VI with an optical tensiometer. Together with engineers at the NTNU EPT lab task VII is completed as a iterative project to optimize the facility.

1.4 Scope of Work

The scope of the review is limited to experiments done with micro pillars and micro pillars combined with nano structures with Silicon as substrate material and deionized water. Nano structures in no combination with micro structures are not considered. Further, proposed theoretical models and equations are not considered or discussed. The author is seeking empirical results and experience.

The scope of the fabrication design is limited to micro pillars and cones. Pillars with a shape, diameter, height and pitch of cylindrical, $25\mu m$ - $40\mu m$, $10\mu m$ - $50\mu m$ and $20\mu m$ - $40\mu m$ respectively, fabricated with a 2" silicon wafer provided by NTNU Nanolab and deep cryogenic etching. The etching process will not consider different power values of the ICP and CCP, chamber pressure, table temperature, gas flow rates or gas ratio.

Cones with a shape, diameter, height and pitch of cone, $15\mu m$ - $73\mu m$, $3\mu m$ - $142\mu m$ and $5\mu m$ - $350\mu m$ respectively, fabricated with a 4" silicon wafer provided by NTNU Nanolab and deep cryogenic etching. The etching process will not consider different power values of the ICP and CCP, chamber pressure, table temperature, gas flow rates or gas ratio.

Coatings for manipulating the surface chemistry will not be considered in this work.

1.5 Structure

In Chapter 2, first fundamental definitions used in the field are clarified. Further, fundamental droplet theory is presented. Then previous results in the research area "Leidenfrost Phenomenon on Structured Surfaces", "Wettability on Textured Surfaces" and "Anisotropic Wettability" are reviewed. Finally, in Chapter 3, an optimal surface geometry is proposed.

Fundamental aspects of micropillar fabrication are discussed based on literature and experience built up during work at the NTNU Nanolab in Chapter 4. Recipe and background theory for cone fabrication are presented in Chapter 5. Carbon nanowire fabrication and the pyrolysis process are presented in Chapter 6. Results from the work done by the author is presented and discussed in Chapter 7. Concluding remarks are presented in Chapter 8.

2. Literature Review

2.1 Definitions

2.1.1 Leidenfrost

The temperature at which the evaporation time of a drop reaches its maximum is called the Leidenfrost temperature, Figure 2.1, or the static Leidenfrost temperature [35] [36]. The minimum temperature of the surface at which a developing vapor layer causes an impinging droplet to bounce when the drop is impacting the surface with a certain velocity is know as the dynamic Leidenfrost phenomenon (LP). The lowest temperature for which the vapor cushion causes the drop bouncing without secondary atomization or splashing is known as the dynamic Leidenfrost temperature [37] [38] [39]. In this paper the critical temperature of film boiling will be refereed to as the Leidenfrost Temperature, T_L or LFP [40].
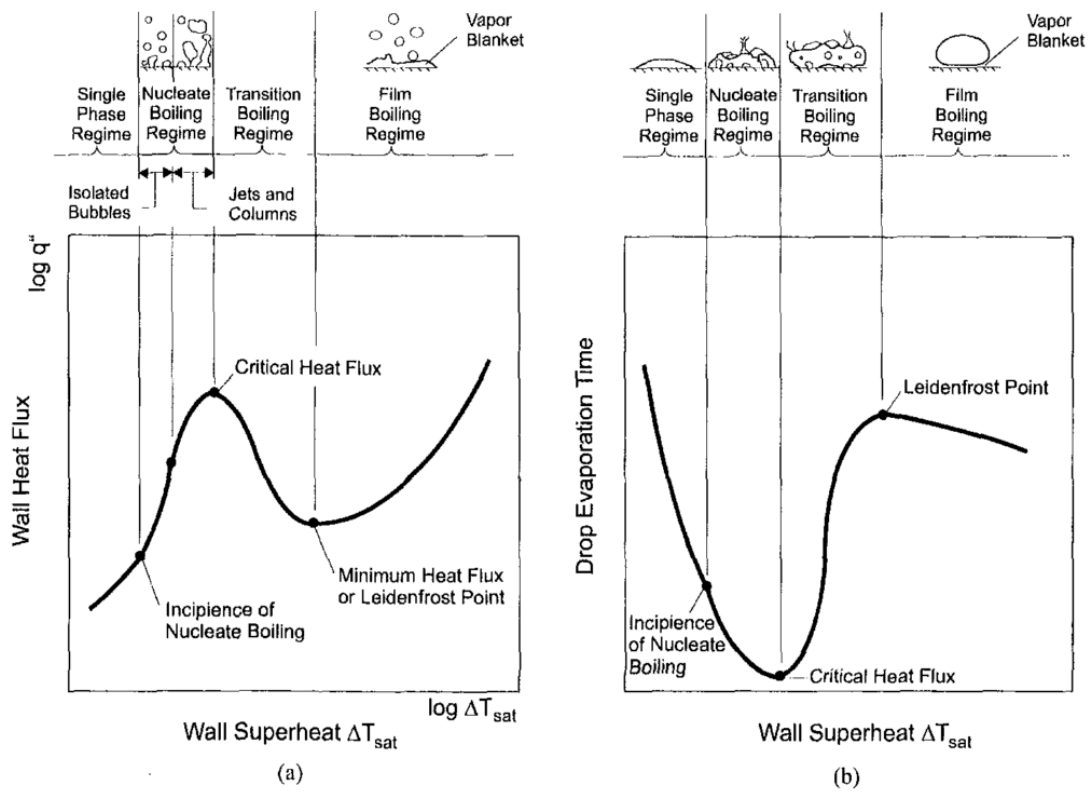
Figure 2.1: (a) Critical Heat Flux (CHF). (b) Leidenfrost Point [7].

2.1.2 Surface Definitions

Control of the surface causing roughness and surface contact fraction is important. Especially the top surface, projected surface and the actual surface area. They are therefore further defined with the following subscripts t, p and a for relevant geometries. Both cylindrical and cone pillars will be fabricated in this work. Cylindrical and cone pillars will be referred to as pillars and cones respectively.
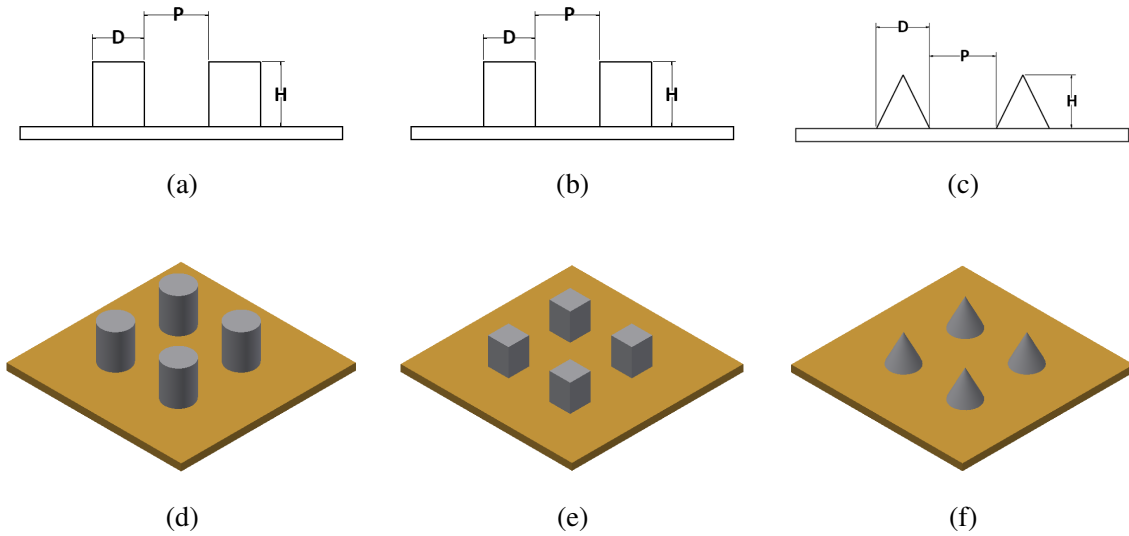
Figure 2.2: (a) Cylindrical pillars. Diameter, Pitch and Height. (b) Square pillars. Diameter, Pitch and Height. (c) Cone pillars. Diameter, Pitch and Height. (d) Cylindrical pillars. (e) Square pillars. (f) Cone pillars.

Cylindrical pillar:

$$A_p = (P + D)^2 \tag{2.1}$$

$$A_t = \frac{\pi D^2}{4} \tag{2.2}$$

$$A_a = A_p + \pi D h \tag{2.3}$$

Square pillar:

$$A_p = (P + D)^2 \tag{2.4}$$

$$A_t = D^2 \tag{2.5}$$

$$A_a = A_p + 4D h \tag{2.6}$$

Cone pillar:

$$A_p = (P + D)^2 \tag{2.7}$$

$$A_t \approx 0.00001 \tag{2.8}$$

$$A_a = A_p - \frac{\pi D^2}{4} + \frac{\pi D}{2}\sqrt{H^2 + \frac{D^2}{4}} \tag{2.9}$$

Conical Frustum:

$$D_L = \text{Lower Diameter}$$

$$D_U = \text{Upper Diameter}$$

$$A_p = (P + D_L)^2 \tag{2.10}$$

$$A_t = \pi D_U^2 4^{-1} \tag{2.11}$$

$$A_a = A_p + \frac{\pi\left(D_U^2 - D_L^2\right)}{4} + \frac{\pi}{2}(D_L + D_U)\sqrt{H^2 + \left(\frac{D_L - D_U}{2}\right)^2} \tag{2.12}$$

Contact surface fraction:

$$f = \frac{A_t}{A_p} \tag{2.13}$$

Surface roughness factor:

$$r = \frac{A_a}{A_p} \tag{2.14}$$

2.1.3   Droplets Fundamentals

Surface Wettability

Wetting is the ability of a liquid to maintain contact with a solid surface. Wettability, the degree of wetting, is determined by a force balance between adhesive and cohesive forces [41] [42]. A substrate surface can have the properties of complete wetting or non-wetting and everything in between. If a liquid is brought in contact with a substrate and the liquid spontaneously make a film on the substrate, then the substrate is complete or total wetting. If a liquid is brought in contact or partially in contact with the substrate, but do not form a film on the substrate, the state is called the Wenzel mode, Figure 2.3. If a liquid remains as spherical drops without making any contact with the substrate, the surface is

non-wetting. This state is also called the Cassie mode, Figure 2.3. Surface wettability can be characterized by a static contact angle (CA) between liquid and solid surface at the triple-phase contact line [43].
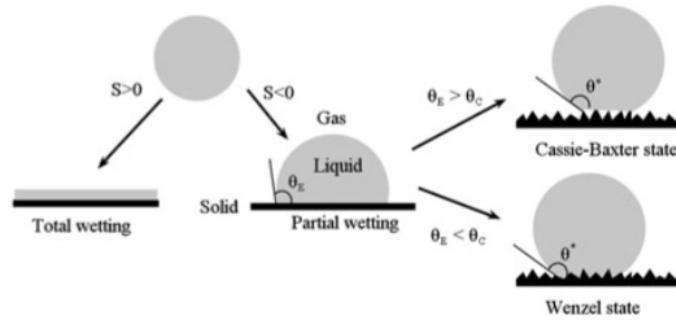
Figure 2.3: Possible wetting states of a droplet on a substrate [8].

Surface Morphology

If the surface morphology is uniform (non-uniform) in different directions, the surface is considered to be isotropic (anisotropic). An isotropic (anisotropic) surface has usually isotropic (anisotropic) wettability [44].
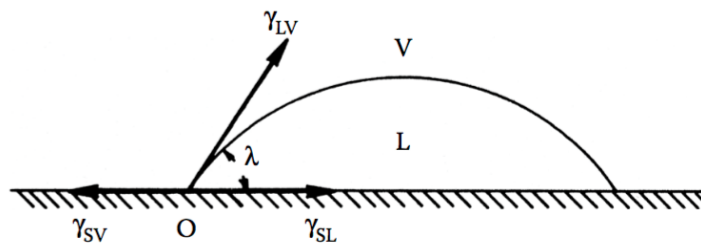
Figure 2.4: Contact Angle.

Contact Angle

The CA is the angle formed by a liquid an the three phase boundary where the liquid, gas and solid intersect. A static or dynamic CA can be measured. The advancing and receding CA are examples of dynamic CA´s. The intrinsic or the equilibrium CA is given by Young´s equation,

$$\cos\theta_e = \frac{\gamma_{SV} - \gamma_{SL}}{\gamma_{LV}} \tag{2.15}$$

were γ represent the surface tension, i.e. the interfacial free energy per unit area, and the indices's S, L and V refer to Solid, Liquid and Vapor. γ_{SV}, γ_{SL} and γ_{LV} are solid/vapor, solid/liquid and liquid/vapor interfacial tensions respectively. Yong´s equation is assuming an ideal solid surface, i.e. the influences of roughness, chemical heterogeneity, swelling ans dissolution are neglected.

Contact Angle Hysteresis

$$\Delta\theta = \theta_a - \theta_r \tag{2.16}$$

Contact Angle Hysteresis (CAH) is a phenomenon that characterizes surface heterogeneity, roughness and mobility. When a pipette injects a liquid onto a solid, the liquid will form a CA. As the pipette injects more liquid, the droplet will increase in volume, the CA will increase, but its three phase boundary will remain stationary until it suddenly advances outward. The CA the droplet had immediately before advancing outward is termed advancing CA. The receding CA is measured by pumping the liquid back out of the droplet. The droplet will decrease in volume, the CA will decrease, but its three phase boundary will remain stationary until it suddenly recedes inward. The CA the droplet had immediately before receding inward is termed the receding CA. The difference between the advancing and receding CA is termed CAH [43].

Spreading Parameter

A droplet will completely wet the substrate if $S > 0$, i.e. $\theta_e = 0°$. When $S < 0$, i.e. $\theta_e > 0°$ a droplet will partially wet the substrate or don´t wet the substrate at all [8].

$$S = \gamma_{SV} - \left(\gamma_{SL} + \gamma_{LV}\right) \tag{2.17}$$

Superhydrophillic

A surface can be inter alia hydrophobic or hydrophilic. A hydrophobic surface is water repelling and has a CA more than 90° on a smooth surface. A hydrophilic surface has affinity for water and has a CA less than 90° on a smooth surface. 65° is also proposed as the limit between a hydrophobic and hydrophilic surface [45]. If the CA is more than 150° and the CAH is less than 5°, we call it superhydrophobic. If the CA is $< 20°$ and the CAH is high, we call it superhydrophilic.

A superoleophobic surface repel oil. If the hydrophobic surface resist wetting from water and organic liquids (superoleophobic) e.g. oils, we call it superamphiphobic or superomniphobic.

Wenzel relation

Wenzel improved the Young´s equation (2.15) in 1936, known as the Wenzel relation,

$$\cos\theta_W = r\cos\theta_e, \tag{2.18}$$

by introducing a surface roughness factor, r. It predicts that roughness, r, enhances wettability. If r is larger than 1, a hydrophilic solid ($\theta_e < 90°$) becomes more hydrophilic when rough ($\theta < \theta_e$). A hydrophobic solid ($\theta_e > 90°$) becomes more hydrophobic ($\theta > \theta_e$) [46]. Drops should be much larger than the defects causing the roughness r to use the model [43].

Cassie and Baxter

Cassie and Baxter proposed another relation describing CAH for composite surfaces consisting of various heterogeneity [47]. The relation has later been modified to be used with textured solid surfaces when $r\cos\theta_e > 1$ and therefore the Wenzel relation not valid [48],

$$\cos\theta_C = f(r\cos\theta_e + 1) - 1. \tag{2.19}$$

Critical Contact Angle

Given a rough surface in contact with a liquid reservoir with a film propagating inside the grooves. Assume the Young relation for locally valid. If the imbition front rises by dz, the inferfacial energies change with a quantity dE per unit width of the sample,

$$dE = (\gamma_{SL} - \gamma_{SV})(r - f)dz + \gamma_{LV}(1 - f)dz \qquad (2.20)$$

were SL, SV and LV are as defiend in (2.15). Gravity was ignored in (2.20) which requires textures smaller than the capillary length,

$$l_c = \sqrt{\frac{\gamma}{\rho g}} \qquad (2.21)$$

were γ is the surface tension, ρ is the liquid density and g is the gravity. The liquid should rise if dE is negative. Combining (2.20) with (2.15) gives a condition for imbibition,

$$\cos\theta_c = \frac{1 - f}{r - f} \qquad (2.22)$$

$$\theta_e < \theta_c \qquad (2.23)$$

were θ_e is the eqilibrium CA of the liquid on an ideal flat surface of the same chemical composition. I.e. with a $\theta_e > \theta_c$ the surface will be hydrophobic and with a $\theta_e < \theta_c$ the surface will be hydrophilic. This is though not always the case due to meta-stable modes [49]. The typical intrinsic CA (θ_e) of organically contaminated SiO_2 surfaces is ~38-42°[50], some limits on r are therefore obvious, see Figure 2.5a

Weber

The Weber number is the ratio of the inertia force and surface tension. For a droplet with density ρ, velocity before impact v^2, characteristic length e.g. the initial droplet diameter l and surface tension σ the Weber number is,

$$We = \frac{\rho v^2 l}{\sigma}. \qquad (2.24)$$

We is an important parameter when comparing CA measurements and evaporation lifetime of a droplet on a heated surface due to their dependence of the inertia force [51] [52]. A We ~1 is therefore often used.
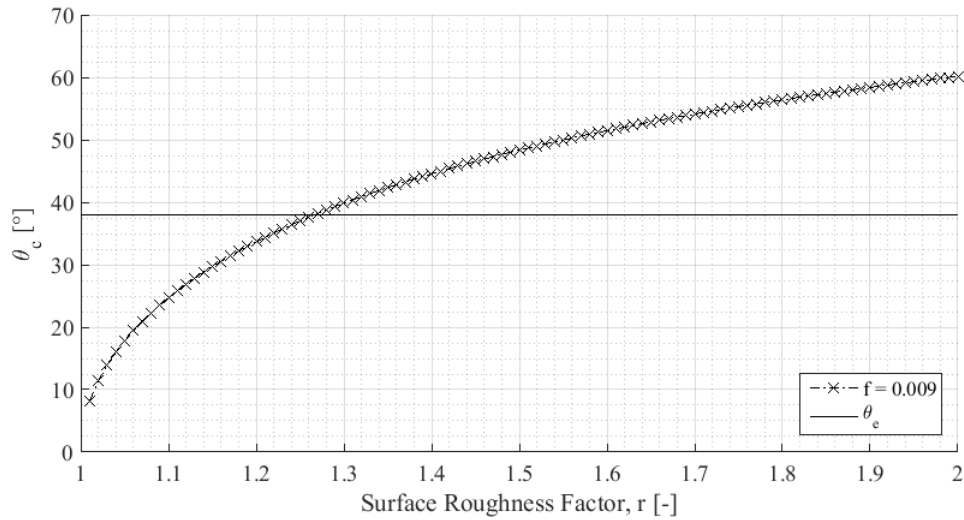
(a)
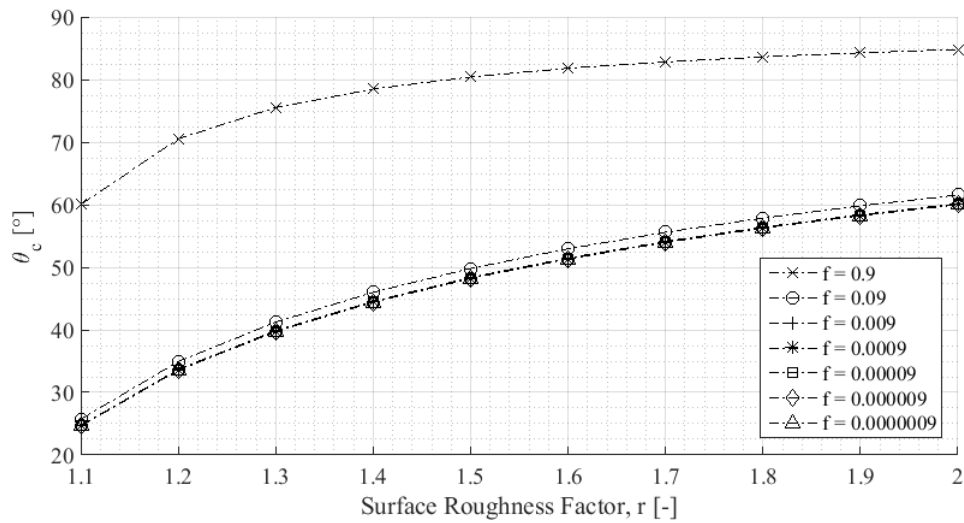
(b)

Figure 2.5: (a) Critical CA versus roughness factor at constant surface contact fraction f = 0.009. A constant value of $\theta = 38°$ is plotted as a upper limit. The critical CA increase with roughness factor. (b) The critical CA approaches a 1/r as f becomes very small. As seen from the plot, the critical CA model cannot handle f < 0.009.

2.2 Previous Results: The Leidenfrost Phenomenon on Structured Surfaces

In forthcoming papers, the sessile drop method has been used in order to measure the CA and/or drop evaporation time. The material used is Silicon if nothing else is stated. When a droplet impacts upon a surface heated above the liquid boiling point, the droplet either comes into contact with the surface and boils spontaneously or is supported by a vapor cushion and bounces on the surface i.e. the Leidenfrost effect [51]. An overview of the characteristics of the geometry's in the experiments are given in Table 2.1 and Table 2.2. It is worth to note that the CA and the drop evaporation time is dependent on environmental factors such as ambient temperature, pressure, humidity, atmosphere and weber number, the properties and temperature of the fluid, surface material, cleanness of the surface, time from fabrication and the heat capacity of the Silicon plate [53]. Since all those factors are not the same through all experiments, they cannot directly be compared.

	Year	D $[\mu m]$	H $[\mu m]$	P $[\mu m]$	V $[\mu L]$	T_{amb} $[^\circ C]$
Feng et al	2011	2.5, 5, 10*	5	2.5 - 35*	-	23
Kim et al	2012	5	0, 5, 10*, 15	500	-	-
Kwon et al	2013	10	10	3.3 - 100*	30	-
Tran et al	2013	9	0*, 2, 4, 8	4, 20	-	-
Duursma et al	2014	5, 10*	10	5 - 100*	8, 15, 24*	-
Li et al	2016	20	20	25 - 100*	16.5	-

Table 2.1: Previous results found in the literature. Diameter/width, height, pitch, initial droplet volume and ambient temperature. A * is used to mark the result with highest LFP.

Bernardin and Mudawar performed sessile drop evaporation experiments with aluminium surfaces to observe the influence of fluid properties, surface roughness and surface contamination on the LFP in 1999. Different results than predicted with theoretical models were observed and a theoretical model to accurate and robust capture the LFP mechanisms was concluded to currently be unavailable. Surface roughness were reported to be a

(a)   (b)   (c)
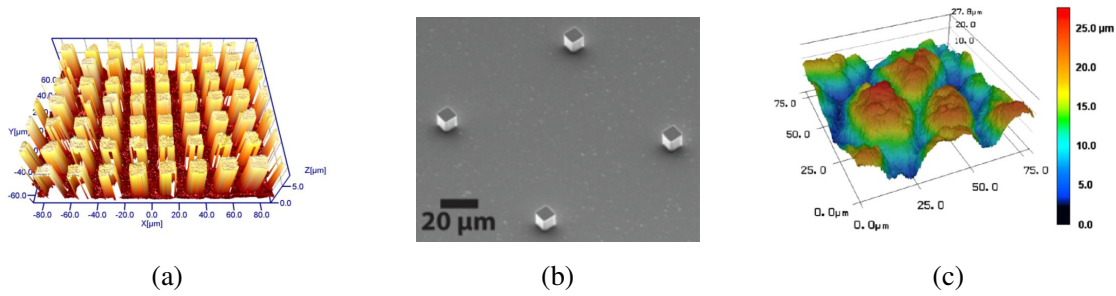
Figure 2.6: (a) 3D interferometer projection of a region with 10 μm pillars and 10 μm spacing, Duursma et al (2014). (b) Micropost array with 10 μm width and height. 75 μm pitch, Kwon et al (2013). (c) 3D surface profile of a substrate from Kruse et al (2013).

dominant parameter in controlling the Leidenfrost behavior. T_L of 171°C on polished Al surface, and $T_L = 263$°C on rough sanded surface were reported. The study was limited to finishing methods and could therefore not give any accurate relationship between the surface geometry and the LFP. [36]

Feng et al (2011) investigated the effect of diameter, pitch and ambient temperature on the LFP by depositing droplets on textured surfaces fabricated by photolithography of Silicon plates. The experiments demonstrated a proportional LFP to diameter and pitch, but inversely proportional to ambient temperature. In the same pillar-size group LFP temperature decreased with f and increased with increasing pillar size. [54]

Kim et al (2012) investigated the effects of surface roughness height, wettability and nanoporosity on LFP of surfaces fabricated with photolithography and reactive etching. The effect of a hierarchical structure i.e. microstructure and nanostructure was studied. The high pitch, 500μm, was chosen in order to avoid secondary effects such as capillarity. The result was a LFP of $T_L = 330$°C independent of the micro pillar height (5-15 μm) without any nano structures. When a nano-porous SiO_2 layer was added by Silicon oxide nanoparticles the surface with highest microposts (15μm) reported the highest LFP. The hierarchical effect was proven positive with an increase in T_L of > 100 °C. [55]

Kwon et al (2013) investigated the effect of surface texture on the LFP by depositing mm droplets onto heated Silicon surface textured with square micropillars, see Figure 2.6b. The surfaces was fabricated using standard lithography techniques. A post fabrication cleaning process with Sulfuric Acid and Hydrogen Peroxide was used and proven to enable the Silicon surface to become more hydrophilic. Kwon et al discovered that surface

texture not always increase LFP. The pitch, i.e. the space between pillars, have a significant importance. A hierarchical textured surface was also fabricated with a micropillar array with a 75 μm pitch and 220 nm diameter Silica particles. The LFP increased to 370°C with micropillars and to above 400°C with both micro and nano structures. [56]

	We [-]	Shape	f [-]	r [-]	H/D [-]	P/D [-]	T_l [°C]
Feng et al	-	Square	0.05	1.1	0.5	3.47	235
Kim et al	-	Cylindrical	0.00008	1.001	2	0.5	330
Kwon et al	~1	Square	0.008264	1.03	1	10	370
Duursma et al	~1	Square	0.008264	1.03	1	10	410
Li et al	1 - 27	Cylindrical	0.02182	1.087	1.0	5.0	290

Table 2.2: Previous results reported in the literature. Weber number, shape, contact surface fraction, surface roughness factor, aspect ratio H/D, aspect ratio P/D and highest LFP temperature with only microstructures.

Tran et al (2013) studied the effect of impact velocity, surface temperature and controlled roughness. For a fixed pitch and pillar width, the dynamic Leidenfrost temperature was decreasing with increasing pillar height. They also discovered that the dynamic Leidenfrost temperature increased with *We*. [51] [38]

The work of Kruse et al (2013) demonstrated a controlled increase of the Leidenfrost temperature. Shifts in the Leidenfrost temperature were attributed to reduction in CA and substantial capillary wicking due to nanoporosity during intermittent contacts of the droplet with the heated surface. A series of surfaces were fabricated by femtosecond laser surface processing on stainless Steel substrate, see Figure 2.6c. Because of the fabrication process, the surface areas cannot easily be calculated. [57]

Duursma et al (2014) used a digital goniometer to measure the CA´s of water droplets on structured Silicon surfaces with different micro-structured regions of square-pillars, see Figure 2.6a. The results revealed that both droplet size and microstructure have significant influence of the LFP. The results indicates a relationship between the surface area fraction, *f*, and the LFP. [58]

del Cerro et al (2012) present a micro patterned surface, fabricated with a picosecond

pulsed laser source, significantly reducing the LFP. The temperature required to reach the LFP was 70% lower than on the flat surface. The CA at room temperature is reported to be ~115°, i.e. hydrophobic. Since the width of the structures is not given in the paper, it is not possible to calculate an accurate r and f. [59]

Li et al (2016) investigated droplets with two concurrent thermal states; Leidenfrost and contact-boiling, further called Janus state. The Janus state was initiated by pinned droplet at the intersection of four patterns with posts of same height and diameter, but different pitch, fabricated with Silicon Dioxide mask on a Silicon wafer. As a part of this work, the LFP for each pattern was reported. [60]

2.3 Previous Results: Wetting on Textured Surfaces

In this section, cases where LFP is not measured, but the transition from Cassie to Wenzel state are investigated. The topic, motivated by producing superhydrophobic surfaces, has been very popular the last ten years and there is therefore done a lot of work in the area.

The wettability of solid surfaces have gained interest for a long time and are being explored still because it remains not fully understood. Motivated by a desire to produce materials with superhydrophobic and syperhydrophilic properties [41].

Yoshumitsu et al (2012) investigated the hydrophobic and sliding behaviour of water droplets on various hydrophobic pillar like and groove structures prepared on a Silicon wafer by dicing and coating it with Fluoroalkylsilane. It could be observed that water contacts the whole surface including the bottom of the groove when the roughness, r, is low, i.e. the droplet is in Wenzel mode. Conversely, when the roughness is high ($r > 1.23$), the water CA becomes high and constant. Trapped air could be observed at the interface between water and solid, indicating the dominance of the Cassie mode. A surface roughness of 1.3 was required to obtain a superhydrophobic state. [61]

Adera et al (2012) demonstrated a non-wetting Cassie state for a superheated hydrophilic Silicon surface. The superheat required to sustain a Cassie droplet after the initial deposition was found to decrease with the square of the droplet radius. [62]

Adera et al (2013) report an unexpected behaviour where non-wetting droplets are formed by slightly heating a superhydrophilic surface beyond the saturation temperature. Silicon micropillar arrays were fabricated using standard photolithography and deep reactive etching. [50]

Liu et al (2013) prepared an array of micropillars on modified hydrophobic Silicon substrate. Wetting transition from a Cassie state to a pseudo-Wenzel state is found with the increase in pitch to with ratio. [63]

2.4   Previous Results: Anisotropic Wettability

Nature inspired (shark skin, butterfly wings, water striders legs and rice leaf [64] [44]) biomimetic surfaces have attracted significant attention in recent years thanks to new microfabrication techniques.

He. et al (2014) investigated the effect of the geometric parameter of micropillar on anisotropic wettability. It was found that anisotropic wettability is related to wetting state and micropillar height plays an important role on the anisotropic-isotropic wettability switch. The surface may switch from anisotropic wettability to isotropic wettability by increasing the micropillar height. Anisotropic wetting seems to cause Wenzel state and isotropic Cassie state. [65]

Another work by He. et al, inspired by the rice leaf, investigated the effect of dual-scale microstructure on anisotropic wettability. Nano-rods were prepared by using galvanic etching. Experimental measured CA´s from orthogonal orientation were used to characterize the anisotropy. The results indicated that dual-scale rods showed isotropic wettability and single-scale micro-rods showed anisotropic wettability. The dual-scale rods was observed in Cassie state and the single-scale rods was observed in Wenzel state. [44]

Ma et al (2013) investigated the wettability on Silicon carbide substrates with laser processed micro-groove structures. Water CA in both parallel and perpendicular direction to grooves were measured. With the increase of the cycle length, CA became larger on the perpendicular direction to the groove, and became smaller on the parallel direction. The CA in the parallel direction was larger than the perpendicular direction which indicates that the anisotropy was significant on the groove textures. The less the size of groove spacing and width was, the more obvious the anisotropy became. [66]

3. Optimal Design of Surface

Previous results reported in the literature do not give any clear overview of an optimal surface geometry for increased LFP. Even though it is obvious that T_l for a given material and liquid can be changed. In Figure 3.1 an aspect ratio plot is used in order to compare the results. Although the results cannot be compared due to not reported or different conditions such as weber number, ambient temperature, cleaning process pre measurement and droplet size, the results will be studied. The, often used, aspect ratio plot, which do not take different geometries such as cylindrical, square or cone (Fig. 2.2) into account, do not show a clear trend. The author of this work suggest to rather use a surface contact fraction versus roughness factor plot, i.e. $f - r$ plot, Figure 3.2. To the best of the authors knowledge, no $f - r$ plot have been reported in the literature before. First of all, it is independent of the pillar shape, second, a trend for the results with the highest Leidenfrost temperature can be observed. The lack of A_t and hence f definition for a cone is though a weakness of the plot. The optimal geometry for Kim et al (2012), Feng et al (2011), Duursma et al (2014) and Kwon et al (2013) are gathered in the south west corner of a $f - r$ plot, see Figure 3.2.
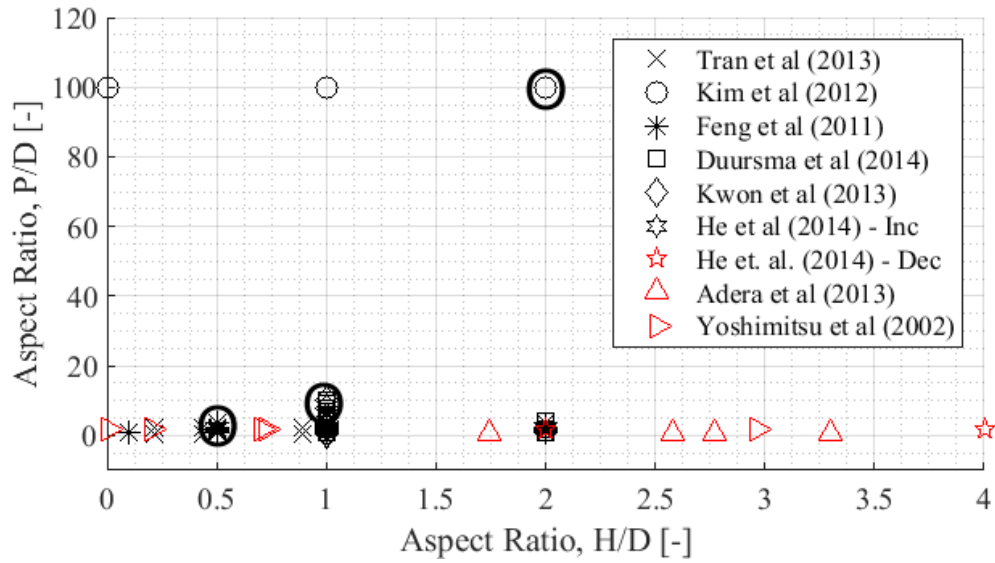
Figure 3.1: Previous results. Aspect ratio P/D versus aspect ratio H/D. Highest LFP are marked with a bold circle. Red values are observed to be hydrophobic. All data included in Appendix B.
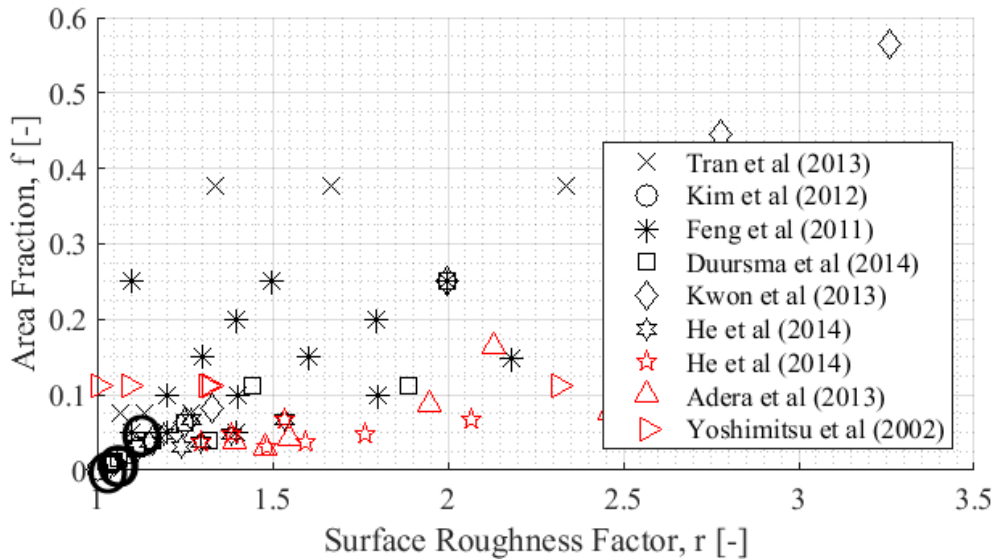
Figure 3.2: Previous results. Surface contact fraction versus roughness factor. Highest LFP are marked with a bold circle. Red values are observed to be hydrophobic. All data included in Appendix B.
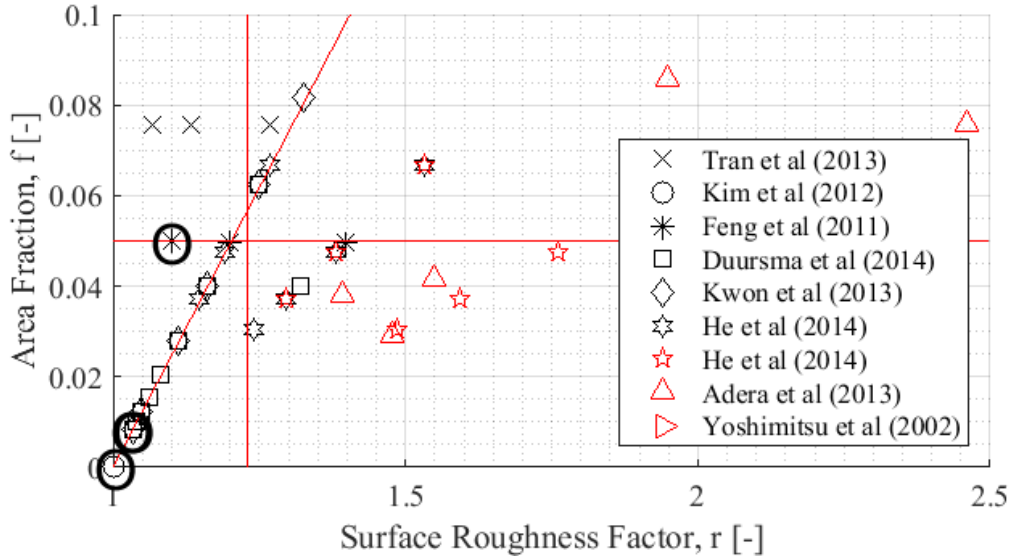
Figure 3.3: Previous results. Surface contact fraction versus roughness factor. Highest LFP are marked with a bold circle. Red values are observed to be hydrophobic. Red horizontal and vertical lines propose upper limits for r (1.23) and f (0.05). A suggested trend line is plotted inclining in red. All data included in Appendix B.

It can be suggested that the surface roughness factor, r, has a upper limit of ~1.23 as seen from Figure 2.5a and proposed by Yoshumitsu et al (2012) [61]. Furthermore, in addition minimization of the contact surface fraction, f. The condition proposed by Lafuma and Quéré [67] $\cos\theta < (f-1)/(r-f)$ will always be true for a hydrophilic surface. The proposed requirement, $r > 1/|\cos\theta|$ for a hydrophobic surface is also a indication of a $r \to 1$ for a hydrophilic surface. This might indicate a reason for the unexpected results from Adera et al (2013). Figure 3.3 underpins the proposed limits of the pillar geometry. All the optimal geometries for Kim et al (2012), Feng et al (2011), Duursma et al (2014) and Kwon et al (2013) are located west of the proposed limit $r < 1.23$. Therefore an optimal surface roughness factor can be found in the interval $1 < r < 1.23$. Furthermore, since Kim et al (2012), Duursma et al (2014) and Kwon et al (2013) all ended up with a higher LFP than Feng et al (2011), minimizing f can be proposed as a goal for optimized results.

Several researchers have indicated a combination of micro and nano structures: a hierarchical structure, as essential for optimal surface [55] [56] [68] [69]. An optimal surface should therefore include a combination of micro structures in one scale and structures in a

lower height scale on the surface between the micro structures, on the top area of the micro structures, on the wall area of the micro structures or a combination of the mentioned suggestions.

Based on the presented discoveries a surface shape as a cone with nanowires on its surface is proposed for further investigations due to its very small top surface and hence low f.

4.   Micro Pillar Fabrication

In this chapter the fabrication method chosen for fabricating micro pillar will be presented. Different choices made will be argued for by experience, best practice and/or by empirical results from other papers. The evolution of the fabrication recipe will be found in Appendix C. Special attention will be given to the etching process due to its importance and complexity. All fabrication is done in an ISO 5 nanolab area, i.e. maximum 100 particles $\geq 0.5\mu m$ pr. ft^3.

4.1   Clarifications

In order to quantify the ability to accomplish a successful etching process, the following figures of merit are defined:

Etch rate (ER),

$$ER = \frac{x}{t},$$ (4.1)

where x is the etched thickness of the substrate and t is the time of etching in minutes. As the aspect ratio of the etched trench increases, the etch rate decline as seen in Figure 4.9a. This is known as the aspect ratio dependent etching (ARDE) effect. The ARDE effect decrease with increased diameter of the micro pillar. [70]

Selectivity,

$$S_{\frac{A}{B}} = \frac{ER_A}{ER_B}$$ (4.2)

the ability to etch only the substrate (A), relative to the etching of the mask (B) used.

Uniformity,

$$Uniformity = \frac{ER_{max} - ER_{min}}{2 \sum_{i=1}^{n} ER_i / N} 100 \tag{4.3}$$

the ability to reproduce the same result.

Anisotropy, the process ability to etch more or only in one direction.

Isotropic   **Anisotropic**   **Completly Anisotropic**
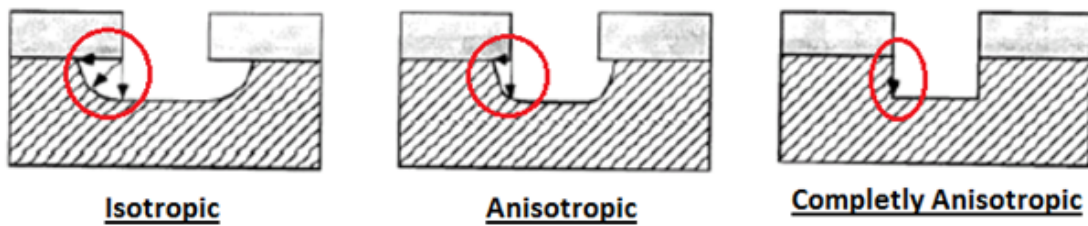
Figure 4.1: Isentropic, anisotropic and completely anisotropic etching. Borrowed from vlsi-expert.com

4.2 Material: Silicon

Silicon is the most studied and the second most available element, in the form of Silica, on earths crust. For that reason, Silicon is both cheap and available. [71]

The wafer used is a CZP<100> (Czochralski, P-type) single side polished (SSP) due to a higher etch rate compared to <111> [72].

4.3 Fabrication

The transfer of micro- and nano patterns onto a Silicon wafer require two processes; (1) photolithography for masking and (2) etching i.e. copying of the mask pattern into the underlying Silicon. There exists methods for making patterns onto a Silicon wafer without photolithography, e.g. focused ion beam (FIB) milling. This method and other direct etching methods are not further considered here due to their slow etching speed.

The reader should notice that two different wafer sizes are used. The cylindrical pillars

Supplier	University Wafer
ID	#444 / #452
Diameter	2" - 50.8 mm
	4" - 100 mm
Polish	SSP
Dopant	B
Fabrication Method	Czochralski (CZ)
Thickness	2" - 320+/-25 μm
	4" - 525+/-25 μm
Orientation	<100>
Type	P
Resistivity	0-100
Grade	Test

Table 4.1: Characteristics of the Silicon wafer used.

are fabricated with 2" wafers and cone pillars are fabricated with 4" wafers. That is due to the authors increased experience during the development of a fabrication method for cylindrical pillars when it comes to the etching step. Though, all steps before the etching process will remain the same, and the only difference with the etching step is the lack of carrier wafer and TIM for the 4" process.

4.3.1 Photomask

For the photolithography process a photomask with the pattern wanted to transfer is required. The photomask is first designed with a convenient software e.g. CleWin and then printed on a thin film or a chrome glass mask, with a 5 μm and 0.8 μm feature resolution respectively. The photomask layout is made by first setting up wafer edge lines and alignment marks, Figure 4.2a. Further, the pattern is made by designing the top surface of one particular shape, Figure 4.2b, and then the first surface is duplicated with wanted pitch in x and y direction, Figure 4.2c, 4.2d. When the wafer layout is finished, the design files from the software are sent to a supplier of high resolution photomasks, e.g. Micro Lithography Services Ltd, for printing. The photomask for cylindrical pillars was made by wax printing on a thin 2" transparent film while a 4" chrome glass photomask, see Appendix E, was used for the cone fabrication.

(a)

(b)

(c)

(d)
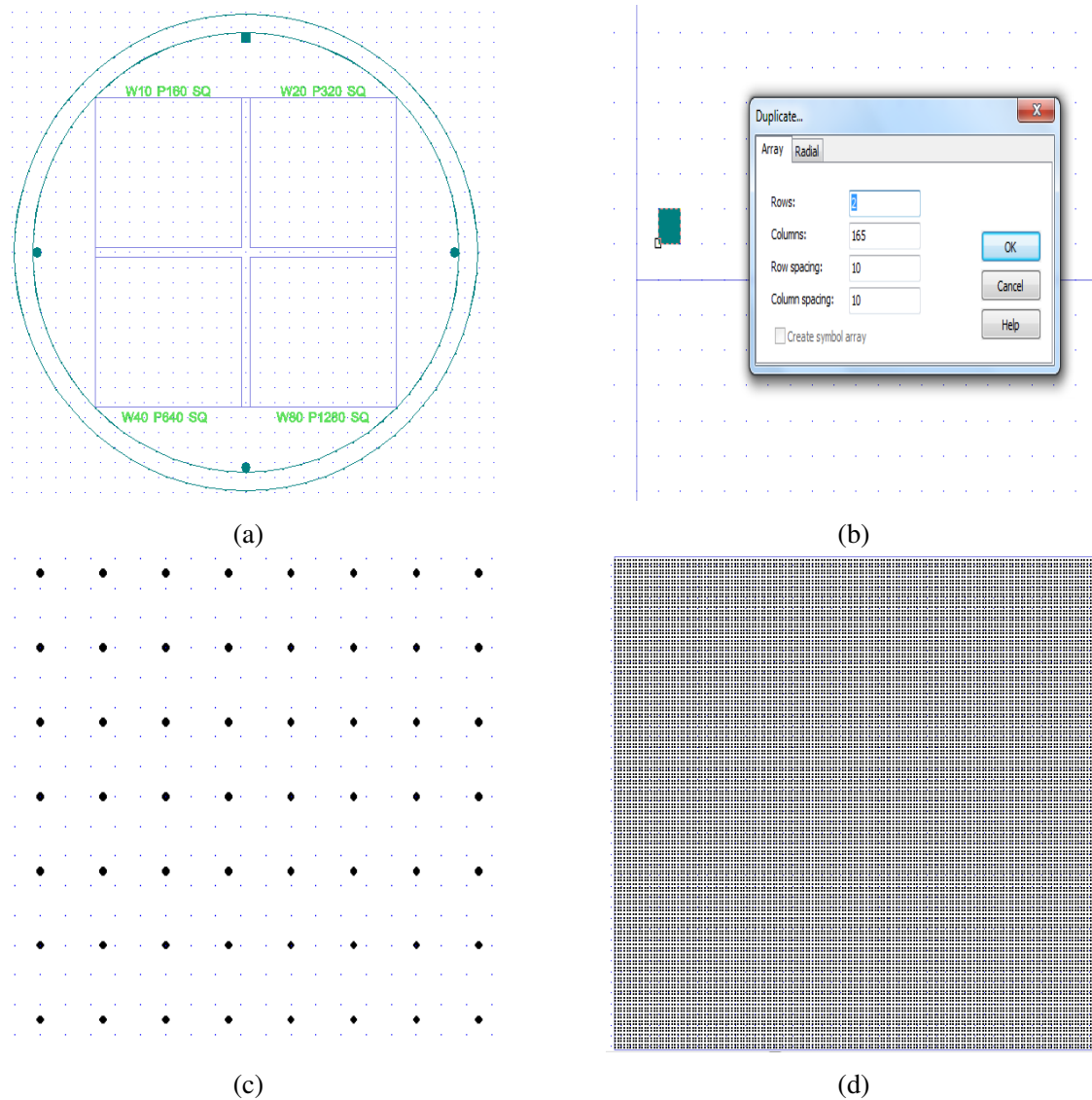
Figure 4.2: (a) Wafer layout. (b) Drawing of one feature. (c) Duplication of the feature. (d) Finished layout with a feature pattern. All Figures from the CleWin software.

4.3.2   Mask

When creating specific geometries on the surface of a Silicon wafer, some parts of the wafer must be protected while the unprotected parts are etched. The protective material is known as an etch mask. An etch mask can be either, what is called hard or soft. A hard mask is made of a metal, nitride or oxide, with coefficient of thermal expansion (CTE) close to the wafer material, has good mechanical properties and a very high selectivity. A soft mask is often made of a photoresist and is used when the etching process is performed

at room temperature. A familiar problem with soft masks is the cracking of the photoresist at cryogenic, i.e. low, temperatures, due to a CTE mismatch. The selectivity is neither as high as with hard masks which restricts the etching depth. Hard masks are therefore often preferred for the cryogenic etching process. [73]
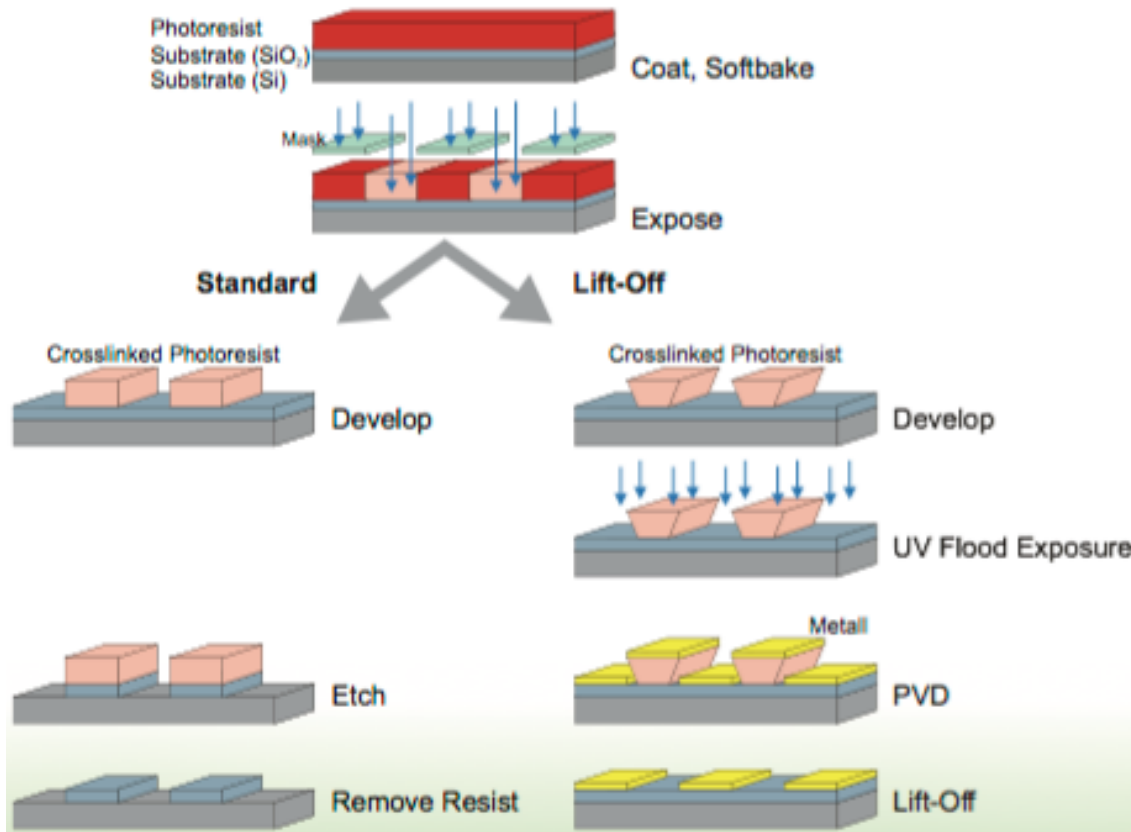
Figure 4.3: Standard and lift-off process. [9]

The lift-off method seen in Figure 4.3 has to be used when a hard mask is fabricated. First a photoresist, preferably one easy to remove with Acetone for the lift-off part, is spin coated, exposed and developed. Then the wafer is sputtered (Custom ATC-2200V, AJA International Inc.) with e.g. Aluminium. Before etching, the Aluminum covering the photoresist is removed with Acetone in an ultrasonic bath, called the lift-off step.

The lift-off method adds two more steps to the mask process; sputtering and lift-off. The sputtering step is time consuming and both the developing step and the lift-off step have a high probability of failure. The developing step is sensitive to the developing time when a photoresist easy to remove has to be used. If the development is too short or too

long, the lift-off step will fail.

High cross-linking density leads to better mechanical strength. With a pre exposure and post exposure bake step, the cross-linking density of the photoresist SU-8 5 can be increased. Therefore a standard method, see Figure 4.3, with the photoresist SU-8 5 is proposed for this case. SU-8 5 is insensitive to the development step, but it is often not used due to the fact that it is challenging to remove after etching. A soft mask with SU-8 5 is further used due to its fabrication convenience.

A typical photolithography process consists of the following steps: cleaning, spin coating, UV exposure, development, etching and characterisation. All of them, and more will be undergone further.

4.3.3 Cleaning

The first and a very important step of the fabrication process is to clean the wafer. That is because any contamination of the wafer will follow the wafer in the process and can affect the end result. To obtain maximum process reliability, the wafer need to be clean and dry before applying photoresist. Without a proper cleaning process, the photoresist will not remain attached to the wafer and the transfer of pattern from photomask to photoresist will fail.

| (a) | (b) | (c) |
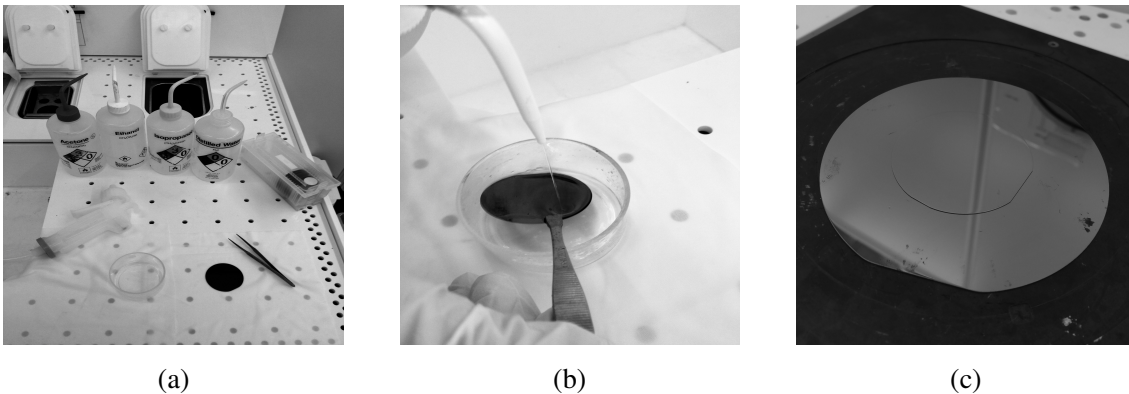
Figure 4.4: (a) Setup for cleaning step. (b) Ethanol cleaning step. (c) Dehydration.

The wafer is first cleaned in a flat beaker by splashing the wafer with Acetone. The wafer is then splashed with Ethanol and, at the same time, lifted up with a tweezer as seen in Figure 4.4b. It is important to start showering the wafer with Ethanol before the wafer is

lifted up from the beaker in order to avoid any Acetone residue on the surface of the wafer. The wafer must continuously be showered with Ethanol, Isopropanol (IPA) and deionized water (DI water). Without any break, the wafer is immediately dried with N_2 until no droplets can be seen on the surface. The wafer should not be dried above the sink, but flat on the bench on a polyester wipe, since it easily can fall in to the sink by the pressurized Nitrogen air when holding it with a tweezer.

4.3.4 Dehydration

The wafer is dehydrated on a hot plate after the cleaning with a temperature of 200°C for 5 minutes. A clean Silicon carrier wafer is used to avoid any contamination from the hot plate as seen in Figure 4.4c. At this stage all OH bonds apparent on the oxidized Silicon surface are thermally cracked. These OH bonds otherwise form a hydrophilic surface with inferior resist adhesion. Applying adhesion promoters such as HMDS or TI PRIME gives a similar result. [9]

4.3.5 Plasma Cleaning

The wafer is further cleaned in a plasma cleaner (Femto, Diener Electronic) for 3 minutes with 50sccm (50%) O_2 and 50W (50%) power to remove any other species on the wafer i.e. make the wafer even more hydrophilic to increase adhesion.

4.3.6   Spin Coating of Photoresist

A negative photoresist, i.e. a photoresist that will not be removed after the photolithography process when exposed to UV light, SU-8 5 from MicroChem is used because of its simplicity since the standard method, Figure 4.3, can be used and its robustness to development. It is a high contrast photoresist based on epoxy, ideally suited for imaging near vertical sidewalls. A spin coater (SPIN150, SPS-Europe B.V.) is programmed with the following speed, time and acceleration respectively; 3000 rpm, 40 seconds and 300 rpm/second (Fig. 4.5a). The program cause a 12.5 μm thick mask. 1000 rpm, 40 seconds and 100 rpm/second was used for the Carbon nanowire fabrication due to a need for thicker mask: 17 μm. The programs is as recommended by MicroChem.

A 2" modified chuck seen in Figure 4.5c is used with the spin coater for the fabrication of cylindrical pillars. The original, Figure 4.5b, is for 4" wafers and therefore used for the fabrication of cones. The one seen in Figure 4.5d is for very small samples, i.e. 5mm x 5mm and not used in this work. A vacuum pump is used to make sure the wafer stick to the top of the spinner. When the wafer is attached to the 2" or the 4" chuck and vacuum is applied, the spinner is tested with manual force to check if the wafer is centered on the spinner top (Fig. 4.5e). This is to make sure of even spreading of the photoresist. Before starting the spin coating process, the wafer is cleaned with N_2 to avoid any particles on the surface before adding the resist (Fig. 4.5f).
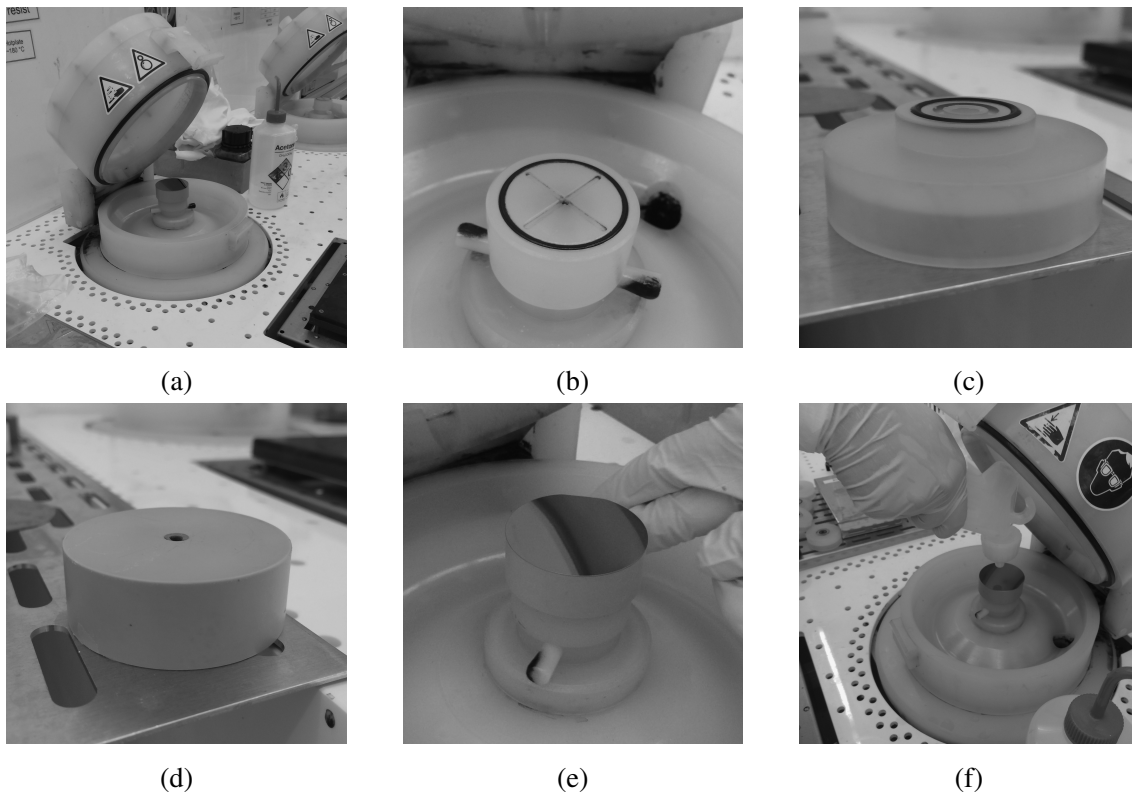
Figure 4.5: (a) SPIN150 SPS-Europe B.V. (b) Original 4" top. (c) 2" top. Can be attached on top of the original 4" top. (d) Modified 4" top. (e) Spin check. (f) Nitrogen cleaning before spinning.

For each inch wafer, 1 ml of SU-8 5 is added to the top surface of the wafer with a pipette. The pipette is inserted into the SU-8 5 container vertically and left there to be fully filled. The pipette is moved to the wafer until the tip is just above the wafer, kept vertically at all time. The first drop and air, if any, is released in the spinner, but not on the wafer. The rest of the SU-8 5 is released on the top of the wafer, slowly. All the photoresist is not used in order avoid air bubbles with the last drops. The pipette is then emptied in the specified waste container, cleaned twice with Acetone and left for evaporation. The pipette is not re-used for the next wafer. The spin program is then executed.

4.3.7 Pre Exposure Soft Baking

Immediately after the spin program is finished, the wafer is transferred to a pre heated (65°C) hot plate for pre exposure soft baking, i.e. baking with low temperatures. A Silicon carrier wafer is used to avoid contamination from the hot plate. The wafer is heated at 65°C

for 1 minute, then the temperature is ramped up to 95°C, as recommended by MicroChem, and baked on 95°C for 3 minutes. The baking time is related to the photoresist thickness. Recommendations are given from MicroChem.

Even though not recommended by MicroChem due to minimize stress, wafer bowing and resist cracking, two hot plates pre heated to 65°C and 95°C and kept constant at the set temperature can also be used. With this setup, no ramp in the temperature will be achieved. Any difference in the result is though not discovered. In both cases, after the baking it is cooled down for 3 minutes on a thick metal disk.

Before exposure the backside of the wafer is cleaned with Acetone in order to avoid contamination on the Mask Aligner chuck.

4.3.8 UV Exposure

A mask aligner (MA6) (Karl SUSS MA6 Mask Aligner UV400, SUSS MicroTec) with the original 2" chuck and mask holder seen in Figure 4.6a and wavelength of 365 nm, the recommended wavelength from MicroChem, is used for exposure, i.e. transfer of the pattern from the photomask to the photoresist. The exposure dose is given by the MicroChem Film thickness - Exposure Energy plot. 200 $mJcm^{-2}$. The intensity [$mWcm^{-2}$] from the UV lamp is measured with an UV-Optometer from SUSS MicroTec, Figure 4.6d, pre exposure once a day. That is because as the lamp gets older, more power is necessary to output the same intensity. Since a constant power is used, the intensity from the lamp will decrease as it gets older. From the exposure energy and the exposure intensity the exposure time can be calculated, $t = mJcm^{-2}/mWcm^{-2}$.

Attention is given when placing the wafer on to the MA6 chuck, especially the height of the screws seen in Figure 4.6b (lower than top of the wafer) and vacuum for holding the wafer on place, Figure 4.6c. If the vacuum is not turned on before exposure, the wafer can attach to the photomask.

(a)

(b)

(c)

(d)
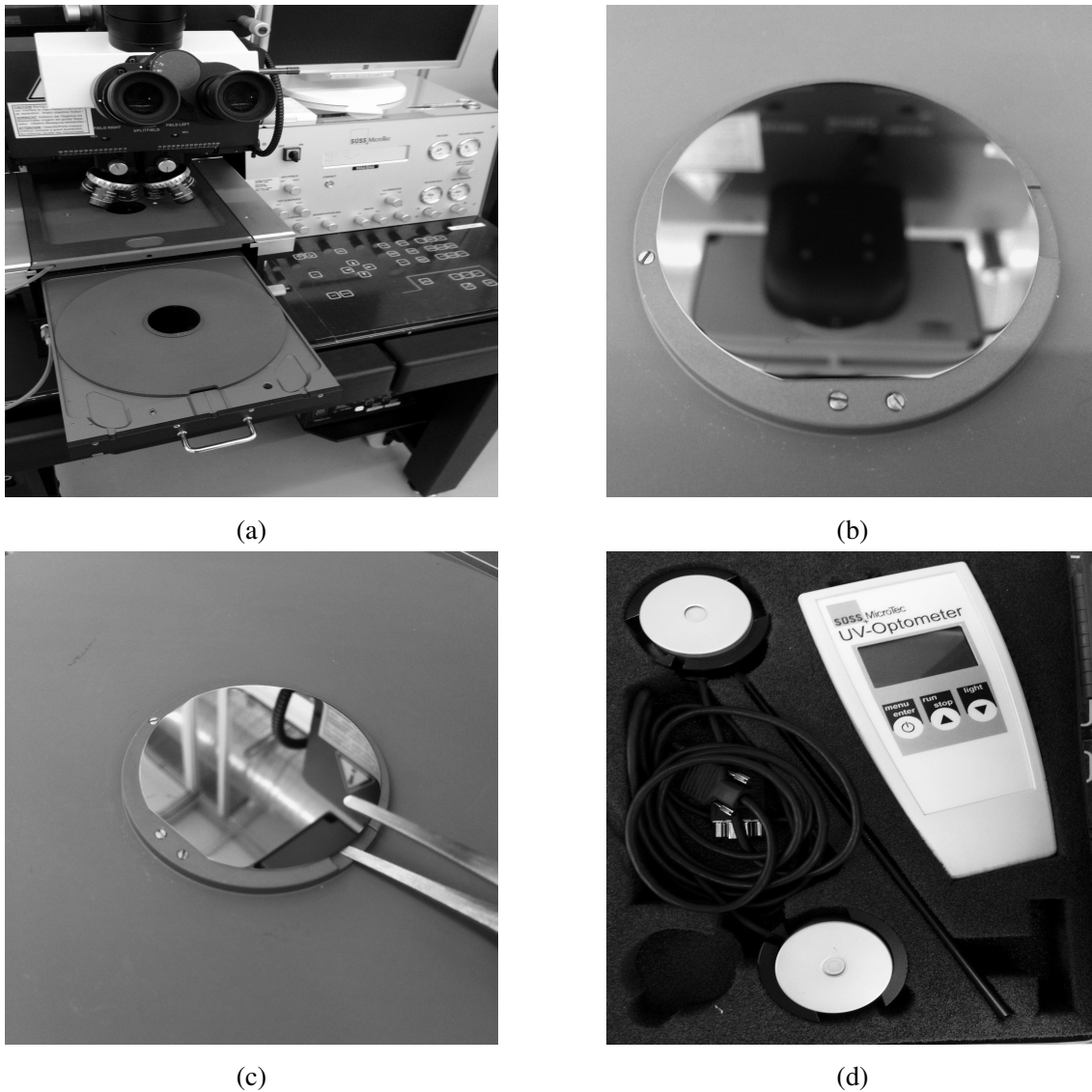
Figure 4.6: (a) Karl Suss MA6 Mask Aligner UV400. (b) MA6 Chuck. (c) Vacuum Check. (d) UV-Optometer.

4.3.9 Post Exposure Soft Baking

After the exposure, a post exposure bake is necessary to selectively cross-link the exposed portions of the photoresist. Immediately after exposure, the wafer is transferred to a pre heated hot plate (65°C) and baked for 1 minute. The temperature is then ramped to 95°C while keeping the wafer on plate. It is baked on 95°C for 1 minute. A Silicon carrier wafer is used between the plate and the substrate to avoid contamination. After the baking, the wafer is cooled down for 3 minutes. It is essential that the post exposure soft baking step

is carried out immediately after exposure since the cross-linking is dependent on it. The cross-linking is highly related to the mechanical strength of the SU-8 5 and hence the ability to not crack under cryogenic temperatures.

4.3.10   Development

The developer mr-Dev 600 (D600) (Micro Resist Technology GmbH) is used to remove the unexposed resist. Two beakers, one with D600 and one with IPA, and a continuously flowing DI water bath is necessary. A sift is used to lower the wafer down in the D600 bath for 1 minute and then raised for a 30 seconds water bath. A 5 seconds IPA bath is given and then the wafer is dried with N_2. If any marks or "oil-film" is observed on the surface of the wafer, the procedure is repeated. The developing time is related to the photoresist thickness. Recommendations are given from MicroChem.

4.3.11   Inter Fabrication Characterisation

Before proceeding in the production, it is convenient to control the photoresist on the wafer. If the photoresist is not showing the wanted pattern, the process should be aborted and restarted with a new wafer. The height of the photoresist geometries is measured with a profilometer (Veeco Dektak 150). The pattern is controlled with a microscope (Nikon Eclipse LV150).

4.3.12   Cleaning

The cryogenic etching process is sensitive to uniformity of temperature on the substrate, hence to any contamination on the back of the wafer [74]. Therefore, the wafer is cleaned with Acetone, Ethanol, IPA, DI water and dried with N_2 before etching.

4.3.13   Dehydration

The wafer is dehydrated before etching to avoid increased humidity in the ICP-RIE Cryo etching chamber. The wafer is dehydrated on a hot plate with a temperature of 200°C for 5 minutes. A clean Silicon carrier wafer is used to avoid any contamination.

4.3.14   Etching

Silicon etching is divided into at certe two categories; wet and dry etching. In wet etching, the Silicon wafer is etched with an aqueous solution. In dry etching, gas is used to etch the Silicon. Wet etching is not further considered by cause of anisotropic etching challenges and its potential of chemical handling hazards due to the use of e.g. HF. For Silicon high aspect-ratio (H/D) geometries i.e. deep reactive ion etching (DRIE), 10 to 500 μm, two dry etching processes are mainly used; the Bosh process [75] and the cryogenic process [76], hereafter referred to as cryoetching.

The Bosch process operates at ambient temperature and is a robust process, therefore it has been preferred for industrial applications [74]. The process uses a combination of a Fluorine, Sulphur Hexafluoride (SF_6), based plasma chemistry to etch the Silicon and Fluorcarbon, Octofluorocyclobutane ($c - C_4F_8$), plasma to provide sidewall protection i.e. passivation layer and improved selectivity. The process cycles between the etching- and the passivation-step, hence called a cyclic etching process, to obtain vertical walls. By adjusting the etch step efficiency, the deposition step efficiency and/or the ratio of times of the two steps, control the etch rate, profile and selectivity. The main drawbacks of the process is the scalloping of the sidewalls as a result of the alternating etching and passivation steps, see Figure 4.7b, and CF_x deposition everywhere in the chamber requiring cleaning steps. Fast pumping and fast response mass flow controllers are required in order to achieve high etch rates, equipment not available at the NTNU NanoLab. [11]

(a)   (b)   (c)
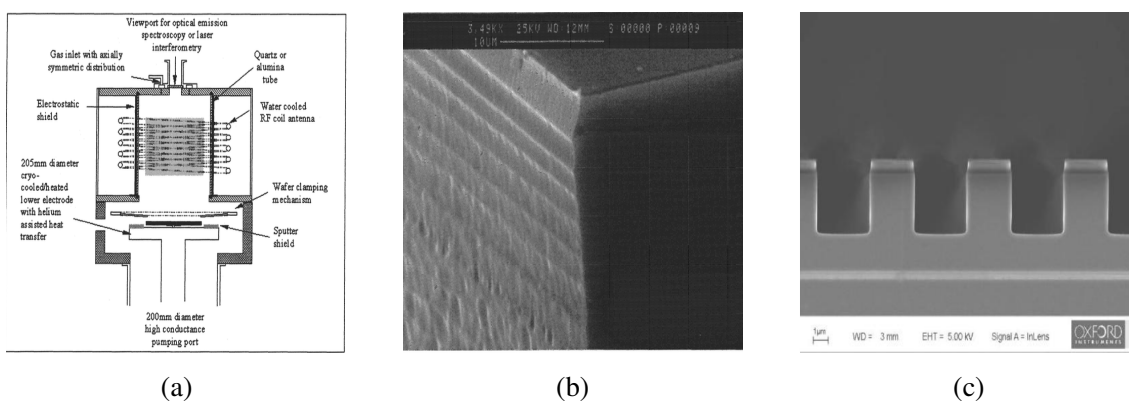
Figure 4.7: (a) Schematic diagram of the ICP system. (b) The Bosh process: scalloping. (c) The Cryoetch process: Smooth walls.

An inductively coupled plasma reactive ion etcher, ICP-RIE Cryo (Plasmalab 100 - ICP180, Oxford Instruments, U.K.) with Aluminium Oxide (Al_2O_3) dome, wafer carrier and clamp is used with the cryoetching method, with SF_6 and O_2, first described by d'Agostino et al [77], at -120°C. The cryoetching method is used due to its capability to etch smooth sidewalls (Fig. 4.7c). An ICP-RIE has two independent powered plasma RF sources. One is an ICP source to create a high radical and ion density i.e. strike the plasma (3000W, 13.56MHz). The other is a coupled plasma source (CCP), also known as forward RF power, to create a DC bias which direct the ions from the plasma glow region towards the wafer surface (300W, 13.56MHz). The ICP-RIE Cryo is further described in detail in [70] and [11]. Liquid Nitrogen is used to reach the cryogenic temperature. A very low temperature is used in order to avoid isotropic etching (Fig. 4.1). Since the Plasmalab is designed to handle 4" wafers, a carrier wafer is necessary to etch 2" wafers. A clean Aluminium Oxide carrier wafer is used when etching 2" samples due to its extreme selectivity and its ability to accentuate the etch rate of Silicon [73].
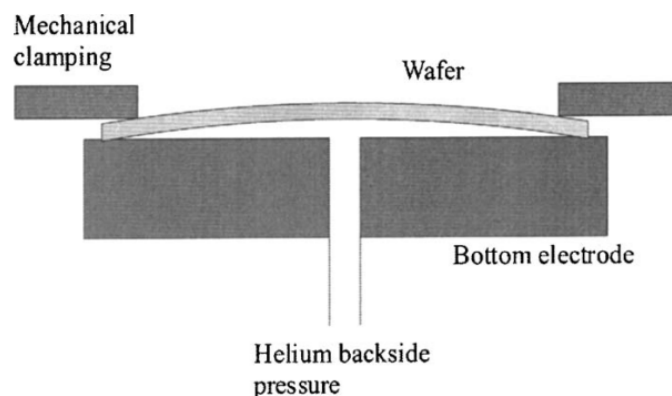
Figure 4.8: Helium Cooling. Helium is transferring heat from the wafer and to the table top, which is cooled by liquid nitrogen. [10]

A Fomblin oil (BOC Edwards) is used as thermal interface material (TIM) because it is easy to handle and can easily be removed with IPA [70]. Other TIMs such as vakuum grease, photoresist or a thermally conductive elastometer pad can be used. A thin film of Fomblin oil is applied to the backside of the sample wafer. When attaching the sample wafer to the carrier wafer; (a) No Fomblin oil can be left on the carrier wafer surface not covered with the sample wafer. (b) No air pockets can be left between the sample wafer

and carrier wafer. Uncovered Fomblin oil on the carrier wafer can be removed with IPA and air pockets between the wafers can be removed by pressing the sample wafer gently against the carrier wafer. The main drawback of the cryoetching process is the sensitivity to substrate temperature [74]. Helium is therefore used between the carrier wafer and the chuck, see Figure 4.7a and Figure 4.8, to increase the thermal conductivity due to its good thermal conductivity. It is very important to ensure that the Helium is sealed adequately underneath the wafer, otherwise the thermal contact to the temperature-controlled table will be degraded. The wafer will then heat up more than expected and the process results may suffer.

When an etching process is to be done, often the table temperature is much higher than necessary by cause of closed liquid Nitrogen valve at standby mode of the ICP-RIE system. It can take a while before the preferred etching temperature is reached. The time should be used to run a chamber cleaning procedure to avoid any memory effect, i.e. remaining gasses from processes previously done by other users of the instrument.

The process can fabricate $\approx 90°$ walls i.e. completely anisotropic walls as seen in Figure 4.1. If the wall angle is $< 90°$ or $> 90°$ it is called "reetrant" or "retrograde" respectively. In the cryoetching method Sulphur Hexafluoride (SF_6) is used to provide Fluorine radicals for Silicon etching. SF_6 is used as etchant because of its proven high etching rate [78]. The Silicon is removed as SiF_4. A blocking layer of SiO_xF_y on the sidewall along with the low temperature inhibits attack on the sidewalls by the Fluorine radicals. The shape of the wall is therefore sensitive to the amount of O_2 added. Typically a proportion of 10% Oxygen in the mixture of SF_6/O_2 is necessary to create a passivation layer at low temperature [79]. The shape of the etch profile becomes more retrograde as more Oxygen is added. Too much Oxygen cetris paribus will cause the formation of grass i.e. nano structures on the surface i.e. "black Silicon". It is called back Silicon since the wafer look black when micro or nano grass is present, see Figure 4.10b. The black Silicon will act as a micromask [80]. Black Silicon formation is also dependent of the ICP power and Bias voltage [81]. The stochiometry of SiO_xF_y i.e. the passivation film, varies with chamber pressure, gas flow, power level, wafer temperature and mask aspect ratio (H/D) [82].

(a)   (b)   (c)
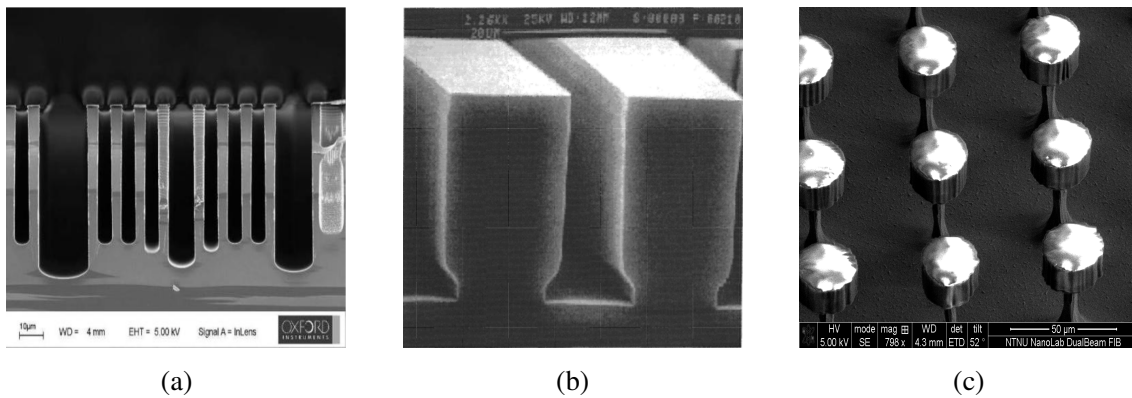
Figure 4.9: (a) The ARDE effect. (b) The notching defect. (c) Undercutting defect.

(a)   (b)   (c)
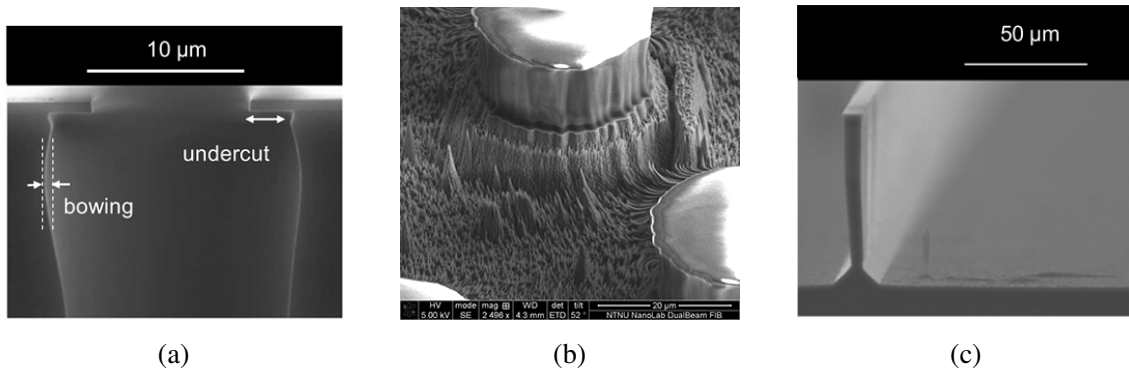
Figure 4.10: Cryoetch Defects. (a) Bowing and undercut defects. Figure borrowed from [11]. (b) Black Silicon defects. (c) CODE defect. Figure borrowed from [11].

Other defects observed in cryoetching are bowing, undercut, notching, loading and the crystal orientation dependent etching (CODE) effect.

Bowing defects can be seen in Figure 4.10a. Bowing defects occurs due to ion bombardment of the passivation layer. Radicals penetrate through voids created in the SiO_xF_y layer and assist ions in the destruction of the trench profile. A high ICP RF power (> 800W) and hence a high self-bias (> 30V) emphasizes the bowing defect. Experiments have shown that when its first initiated, it increases with process duration [83]. Boufnichel et al discovered that bowing is highly related to the O_2/SF_6 gas ratio. With an O_2/SF_6 ratio equal to or above 8%, local bowing is eliminated [83]. [11]

Undercut (Fig. 4.9c) defects can be due to spontaneous chemical reactions of radicals of the plasma and it keeps growing linearly with process time when first initiated. Undercutting is highly related to the temperature of the process. Cryogenic processes shows

an increasing amount of undercut at temperatures higher than -90°C, ceteris paribus [84]. A reduction of the SF_6/O_2 ratio also leads to less undercut [85] and undercut linearly increases with chamber pressure and RF power. It can be avoided by ramping the SF_6 flow the first minute of the process. [11]

Notching (Fig. 4.9b) is an etch into the oxide corners of the etched substrate by removing sidewall protection in the area. It can especially be caused by a burid oxide layer e.g. used for offset the ARDE effect [74]. The notching defect can be avoided by increasing the level of Oxygen in the mixture.

The Loading Effect is characterized by a decrease in etch rate as the quantity of substrate in the chamber is increased e.g. from 2" to 4", for a given set of etching conditions [86].

The CODE effect can be seen in Figure 4.10c. It appears as a 45° foot at the bottom of the pillar/substrate and a negative slope of the wall. The effect can be seen when etching at low temperatures. The effect can be avoided by rising the temperature some or with a alternating amorphization step by Ar/O_2. [11]

The cryoetching process depends highly on the following variables: CCP power, ICP power, chamber pressure, substrate temperature, O_2/SF_6 ratio, SF_6 flow rate, mask width, etching depth and Silicon crystal orientation. A 10 mTorr chamber pressure is kept through the pillar fabrication process as recommended by Walker [74]. A higher pressure can have severe effect on the profile. The ion energy controlled by the CCP power and the ion density controlled by the ICP power can be adjusted independent of each other, a great flexibility of an ICP-RIE. A recommended recipe from Oxford instruments is further used to fabricate pillars, see Appendix C for details.

4.3.15 Cleaning

After the etching process, the wafer is cleaned with IPA in order to remove any Fomblin oil. This is important to avoid any unnecessary contamination of the FIB stage in the characterisation process. The rest of the etching mask is removed with an Oxygen plasma cleaning recipe in the ICP-RIE Cryo, see Appendix C.9.

4.3.16 Characterisation

(a)   (b)   (c)
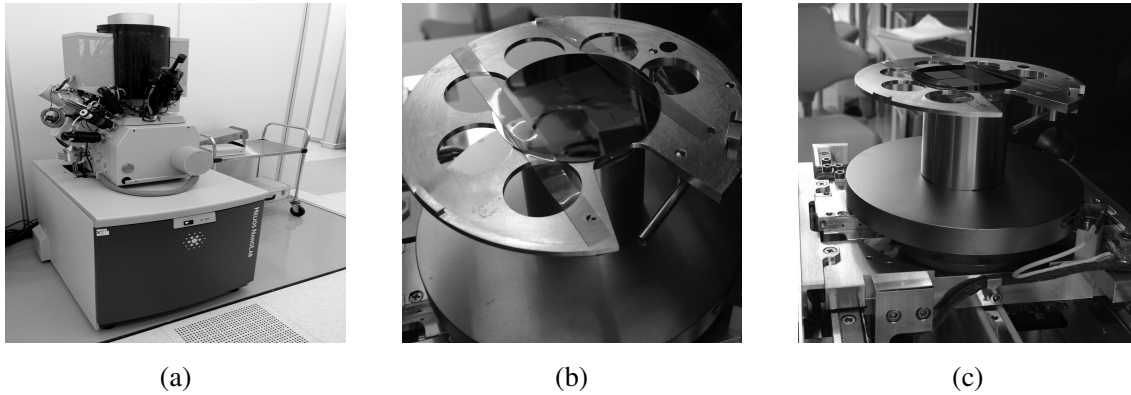
Figure 4.11: (a) The FIB. (b) 4" stage for wafers. 2" wafers can be used. Attached with tape. (c) Wafer stage, overview.

The Scanning Electron Microscope (SEM) of a Focused Ion Beam (FIB) (FEI Helios NanoLab DualBeam FIB) is used to measure height, pitch, width, wall and in general look at the fabrication post etching. A 4" wafer stage is used to hold the wafer in place when changing the angle of the stage. Tape is used to attach the 2" wafer to the stage as seen i Figure 4.11b and 4.11c

5. Cone Fabrication

A cone structured surface with very small top surface and hence low f can be suggested as a possible direction to go for increasing the LFP temperature. A relationship between low CA, $(\theta \approx 0°)$, and improved wetting can be seen from previous results reported in the literature [87] [88]. The *Ruellia devosiana* leaf (Fig. 5.1a) show impressive rapid spreading of water on its leaves and an interesting topography. There is no other plant known showing a better spreading of water on its surface. A water droplet will spread to a film with a CA of 0° within less than 0.3 s. The surface geometry of the *Ruellia devosiana* can therefore be used as inspiration on the path to the optimal surface topography for increased LFP temperature. Even though a hydrophilic surface may cause an improved wettability, it is not given that this will cause a improved LFP [52] [56]. The cause for improved LFP is more complex and not yet well enough understood. [12]

(a) (b) (c)
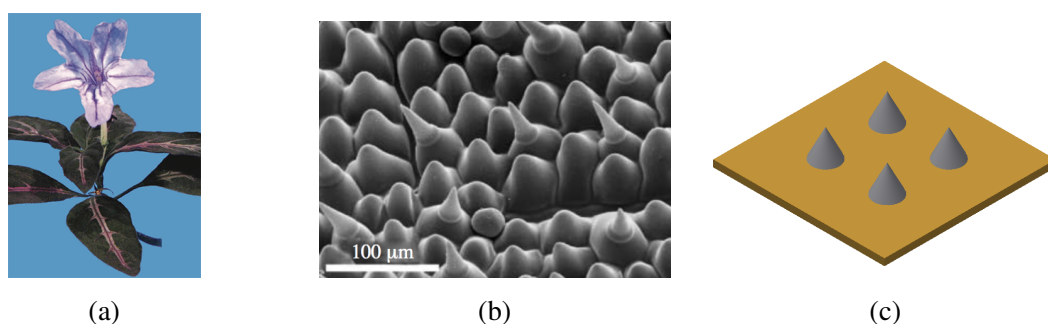
Figure 5.1: (a) Picture of the *Ruellia devosiana* [12]. (b) SEM micrographs of the super-hydrophilic leaves surface of *Ruellia devosiana* [13]. (c) Cones.

The *Ruellia devosiana* has a surface with several structures or cell types (Fig. 5.1b), though most of them are cone like (Fig. 5.1c). The author will therefore focus on the

fabrication of cone structures. Fabrication of cones will hence be the subject of this chapter. The stages until etching are the same as with fabrication of cylindrical pillars and the reader will therefore be referred to the previous chapter regarding the fabrication steps before etching.

Cones can be fabricated on silicon wafers by using standard lithographic techniques. Kondrashov and Rühe (2014) used a mask-free deep cryogenic reactive etching process [18]. Arce (2014) used a cryogenic reactive etching process with mask in his dissertation [17]. Our work require control of the pitch and hence the technique used by Kondrashov and Rühe cannot be used. Fabrication of cones is further based upon the results in [17] and investigated in regard to etching time.

The microcones fabricated in our work was using a cryogenic DRIE process, which was carried out in an ICP reactor (Plasmalab 100 - ICP180, Oxford Instruments, U.K). 100 sccm SF_6 and 17.5 sccm O_2 were simultaneously applied when the electrode temperature was kept at -50°C. I.e. $> 10\%$ O_2 and hence a retrograde profile will be etched. The plasma was generated using 500 W coil power, $\frac{P_{ICP}}{Q_{SF_6}} = 5$ [89], and 20 W coupled plasma power while the chamber was kept a pressure of 75 mTorr for smooth walls [90].

Below 5 mTorr and above 20 mTorr the plasma may not strike or strike with insufficient stability for certain gases. The strike of the plasma is also related to the ICP and CCP power [91]. The plasma may die if the pressure is increased, with a too big step, after the strike of the plasma is successfully completed. The pressure should therefore ramped e.g. 2 mTorr / 5 sec from striking pressure to etching pressure.

6. Carbon Nanowire Fabrication

Nanowires, one dimensional materials, of semiconductors exhibit often unique and superior electronic, optical, mechanical, thermal and chemical properties [92]. Silicon nanowires (Fig. 6.1a), Copper nanowires (Fig. 6.1b), Zirconium nanowires (Fig. 6.1c), Zirconium nano tubes and Carbon nano tubes have shown promising results for pool boiling [93, 94, 15, 95, 96, 97, 98], condensation [99] and impacting droplets on surfaces [100, 101, 102, 103]. Graphene sheets, fullerenes, nanotubes, diamond-like coatings and various types of Carbon nano structures have been fabricated earlier with valuable properties. Amorphous Carbon, short-range order of Carbon, have shown a high thermal conductivity [104, 105, 106]. It can therefore be expected that Carbon nanowires might show the same promising thermal characteristics.
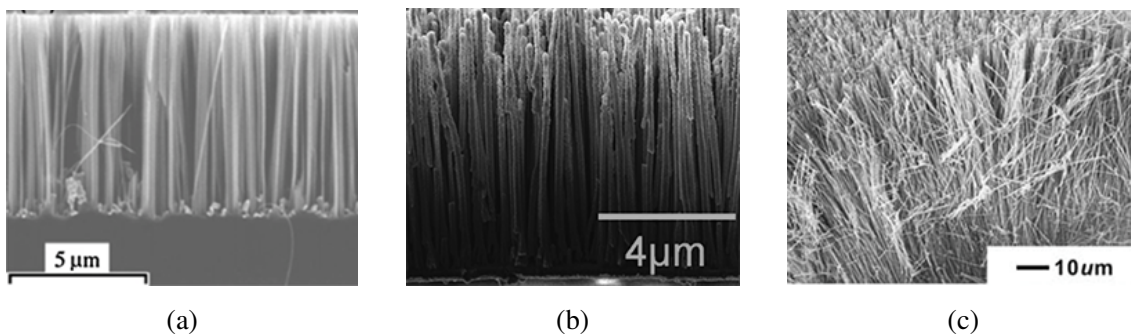
Figure 6.1: (a) Cross-sectional SEM image of an array of silicon single crystalline nanowires produced by solution metal assisted chemical etching [14]. (b) SEM image of 8 μm tall vertically aligned copper nanowires attached to a silicon substrate [15]. (c) SEM image of a 60 μm tall bundle of zirconium nanowires [16].

Copper, Zirconium and Silicon nanowires can be fabricated with several methods fur-

ther described in [92] and [14]. In this work a more convenient fabrication method is desired. Positive and negative photoresist, commonly used in the semiconductor industry, deposited on Silicon wafers, exposed and pyrolysed in an inert environment produce Carbon films [107]. If the photoresist is exposed for an Oxygen plasma before the pyrolysis process, one dimensional Carbon can be fabricated [108].

The pyrolysis process consists of several stages; (1) Precarbonization ($T < 300°C$), (2) Carbonization ($300°C < T < 500°C$), (3) Dehydrogenation ($500°C < T < 1200°C$) & (4) Annealing ($T > 1200°C$). When polymers are heated in an inert environment to temperatures above 300°C, Oxygen, Nitrogen, Chlorine, Hydrogen etc. are removed as gases and the polymer change form to Carbon. The process is further described elsewhere. [104] [109]
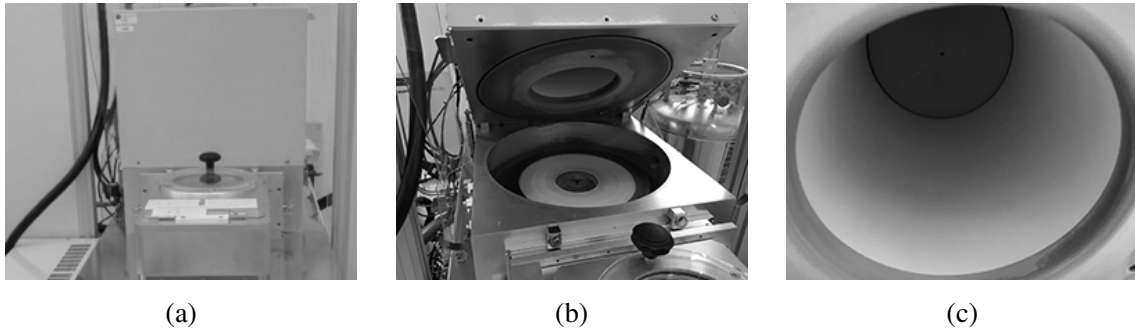
Figure 6.2: (a) ICP-RIE Cryo (Plasmalab 100 - ICP180, Oxford Instruments, U.K.) (b) Plasmalab 100 dome. (c) Dome

In this work the SU-8 layer is exposed to O_2 plasma (300W ICP, 40W CCP, 100 sccm O_2, 50 - 85 mTorr, 20°C) before the substrate is pyrolyzed. The Oxygen plasma create an anisotropic nanowire texture where the substrate is covered with a SU-8 layer. It is not clear why the Oxygen plasma is creating nanowires in the SU-8 layer. It is believed that antimoney from the SU-8 and Aluminium sputtered from the plasma chamber dome seen in Figure 6.2 can mask the SU-8 layer and furthermore create nanowires [108].
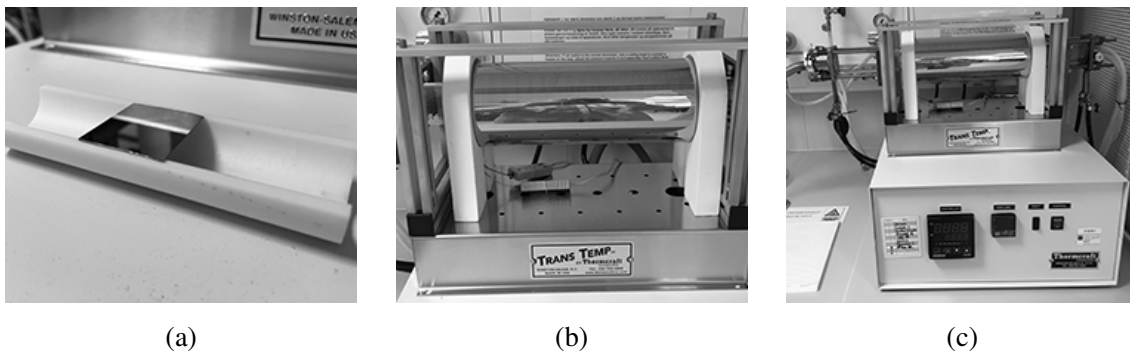
Figure 6.3: (a) Substrate carrier. (b) Calcination Gold Furnace. (c) Furnace overview with gas input/output.

After the Oxygen plasma exposure, the substrate is taken through a pyrolysis process; (1) heated to 300°- 40 min ramp, 30 min hold, (2) heated to 800 °C - 90 min ramp, 60 min hold, (3) cooled down to room temp - 12 hours ramp, all steps with a continuously N_2 flow at 1 bar [108]. A calcination gold furnace, Figure 6.3, (TTL-2,25-0-12-1B-J8961/ 1A, Thermcraft, US) with operating temperatures up to 800°C is used. Because of the upper temperature limit of the furnace, complete loss of non carbon elements is not achieved. 1000°C (900°C) is necessary according to Kim et al [110] (De volder et al [108]). The resulting material is termed a pyropolymer and has properties intermediate between a polymer and carbon [109].

7.   Results & Discussion

The main results regarding the fabrication of the structures will first be reviewed in this chapter. Then results from the fabrication of pillars, cones, nano structures and the combination of the two last will be reviewed in further detail, respectively in separate sections. A preliminary post fabrication analysis of the wetting condition of some substrates will end this chapter.

The following main results may be extracted from this work:

I. Process Guidelines, Section 7.1

   A summary of essential aspects for fabrication of relevant structures is given in this section.

II. Micro Pillar Fabrication Results, Section 7.2

   Micro pillars previously fabricated are presented [111] and valuable experience is discussed.

III. Micro Cones Fabrication Results, Section 7.3

   Determination of dimension limits for micro cones are presented. The work resulted in structures completing the $r - f$ plot presented in Chapter 3 and 142 μm high cones, the highest reported.

IV. Carbon Nanowires Fabrication Results, Section 7.4

   The novel pyrolysis Carbon Nanowire fabrication technique presented by De Volder et al [108] has been tested with success.

V. Hierarchical Structures Fabrication Results, Section 7.5

The combination of cones and nano structures from black silicon and pyrolysis will be presented in this section.

VI. Anomalous Wetting of Hierarchical Structure, Section 7.6

In this Section unexpected wetting characteristics of a hierarchical structure combined of $\approx 50 \mu m$ and $\approx 3 \mu m$ high cones are presented.

VII. Test Facility for Impacting Droplet, Section 7.7

The designed test facility for impacting droplets is presented in this section.

7.1   Process Guidelines

7.1.1   Etching - Helium

It is very important to ensure that the Helium gas is sealed adequately underneath the wafer, i.e. no or small Helium leakage, during the etching process otherwise the thermal contact to the temperature-controlled table will be degraded and the gas mix in the chamber will be affected. The wafer will then heat up more than expected, gas ratio may change and the process results may suffer. The Helium leakage is tested at 9.9 Torr before the etching procedure starts as a standard recipe step. The flow rate value from this test do not always reflect the actual Helium flow rate during etching. Therefore, it is better to look at the Helium flow rate during etching, booth the average value and a plot of the flow rate over time.

The average Helium flow rate for pillars and cones at 10 Torr is presented in Table 7.1 and 7.2 in Section 7.2 and 7.3 respectively. Helium flow rate plots can be found in Appendix A. It can be observed that the Helium flow rate is, in general, stable for a sample, but vary for both pillars and cones between samples. The pillar fabrication has an average minimum value of 8.9 sccm and an average maximum of 18.9 sccm, i.e. the average value over the whole etching step. The cone fabrication has an average minimum value of 20.1 sccm and an average maximum of 33.0 sccm.

The Helium flow rate should be lower than 6.5 sccm at 10 Torr when no leakage is
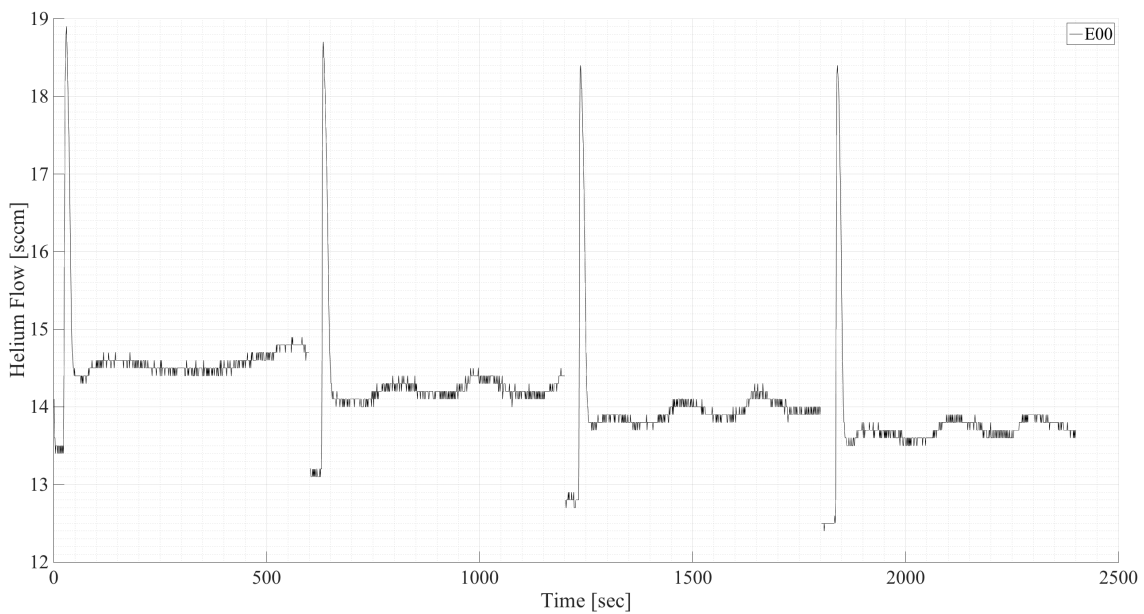
Figure 7.1: Flow rate of Helium to backside of wafer E00 as seen in Fig. 4.8. E00 is etched in four 10 min cycles.

present as recommended by Oxford Instruments [91]. Therefore a Helium leakage must be assumed to be present for all results. The varying leakage will affect the results presented later and influence ER and uniformity. The Helium flow rate is not correlated with etching time, see Table 7.1 and 7.2. The flow rates are all over higher while fabricating cones compared to when fabricating pillars.

The Helium flow rate plot is a useful tool for evaluation of an etching process. Each time the plasma ignite, the helium flow rate peak. With E00 the plasma ignite four times, since E00 is running a four cycle process. It can be verified by looking at Figure 7.1 where four peaks can be observed. The plot can verify if the plasma was running as expected. When several unexpected peaks can be observed, the run cannot be as planned. See Figure 7.2 and Figure 7.3 for example. Sample E04, who Figure 7.2 is related to, suffer from to high lateral etching known to be related to the substrate temperature. The temperature can increased due to the change in Helium flow rate at t = 600 s seen in Figure 7.2.
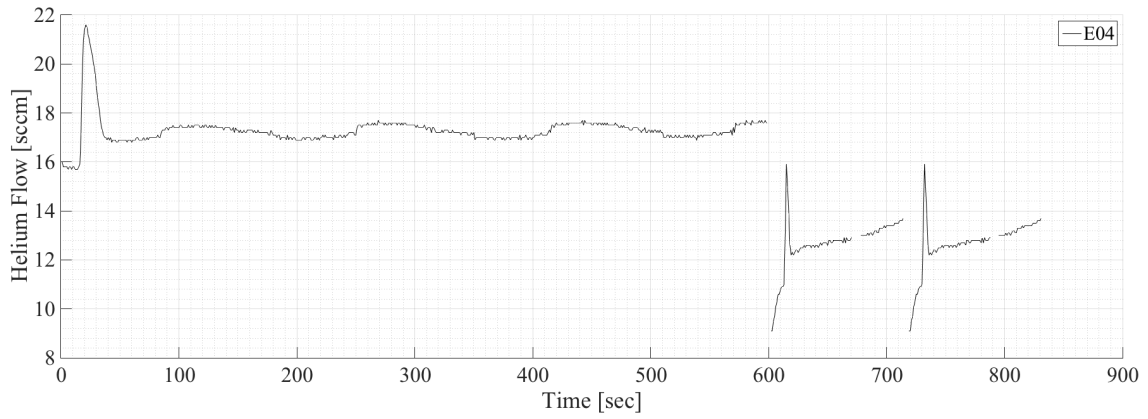
Figure 7.2: Flow rate of Helium to backside of wafer E04 as seen in Fig. 4.8. E04 is etched in two 10 min cycles.
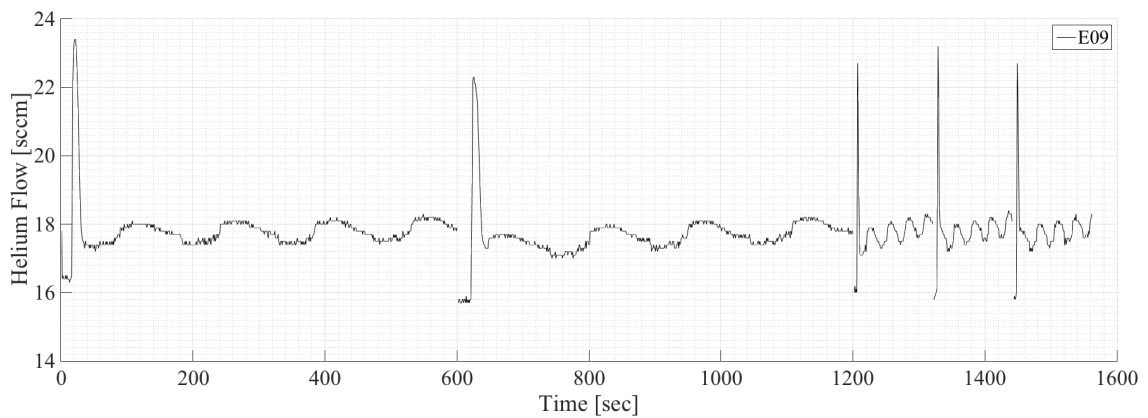
Figure 7.3: Flow rate of Helium to backside of wafer E09 as seen in Fig. 4.8. E09 is etched in five 10 min cycles.

(a)   (b)   (c)
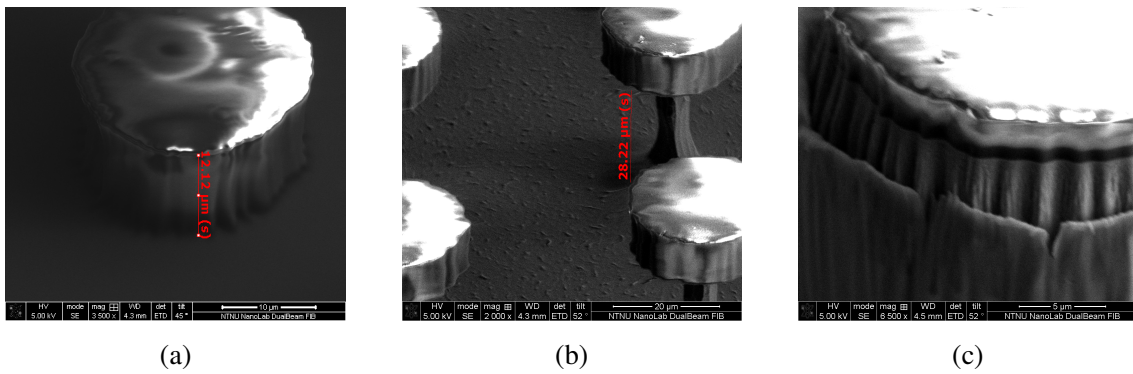
Figure 7.4: (a) SU-8 5 mask pre etching. (d) E04 SU-8 5 mask post etching. (g) E10 SU-8 5 mask post etching.

7.1.2 Mask

A soft mask of SU-8 is used by reason of fabrication convenience. SU-8 can provide mask thickness from 1.5 - 40 μm and is hence very appropriate for our work. A hard mask is often preferred due to cracking of soft masks. No cracking of the mask can be seen from Figure 7.4, where Figure 7.4a is the mask before etching and Figure 7.4b and Figure 7.4c are the mask after etching. That is for both 12.5 and 3.5 μm thick mask. The result is in accordance with the literature [10] and was observed for all substrates. Post etching the mask can be removed by an Oxygen plasma etching step, see Appendix C.9. The mask is removed from all cones, but pillars. The mask thickness is experienced to be consistent over samples with the same recipe (Fig. A.27).

7.1.3 Plasma Color

An important parameter recommended to be taken into consideration, but not considered in our work, is the color of the plasma. The gas mixture affect the color of the plasma and therefore a camera should be used to record the color changes of the plasma. Then failure in the gas delivering system to the chamber and/or Helium leakages can be discovered.

7.1.4 SEM Values

All data represented in Table 7.1 and Table 7.2 are collected with a SEM at an angle of 52°. The lengths are measured on the picture based upon values from the FIB. High accuracy

of the values reported should not be expected, but in the micro meter range, +/-10%.

7.1.5   Etching rate

The etching rate, ER, is tabulated in Table 7.1 and Table 7.2 and plotted in Figure 7.5 and Figure 7.6.

Pillars are fabricated with several different photomask's and hence different diameter of structures and pitch is present. Due to the ARDE effect the ER for the pillars cannot be compared and reviewed.

The ER for cones is close to linear, though decreasing with time, as expected. ER is much more consistent compared to when fabricating pillars. That might be due to less substrate temperature and bias voltage differences as a consequence of using 4" wafer and hence no carrier wafer and therefore a lower temperature difference from table top to wafer. The ER for cones and pillars are biased by the Helium leakage.

7.1.6   Process Optimization

Our experience, best practice advice from experienced Nanolab users and engineers, and by empirical results from other papers during fall 2015 and spring 2016 have resulted in an evolution of the fabrication recipe. Our conclusion can be found in Chapter 4 and are reflected in the recipes attached in Appendix C. Experience gathered regarding the cleaning, photolithography, choice of mask and etching have been absolute for success.
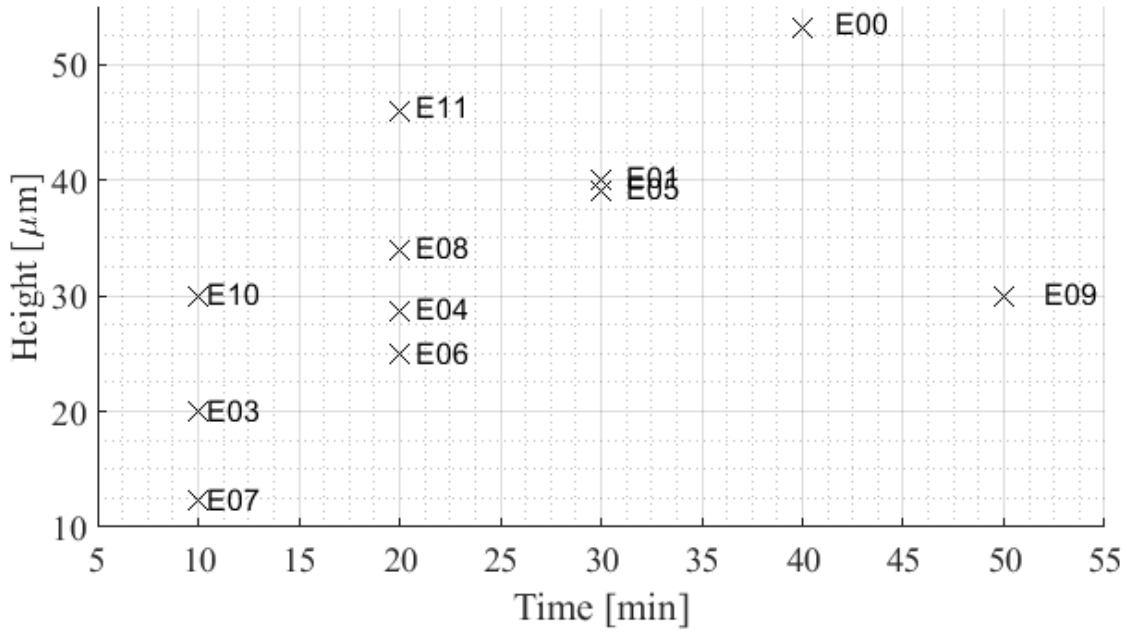
Figure 7.5: Etching depth/pillar height by etching time.
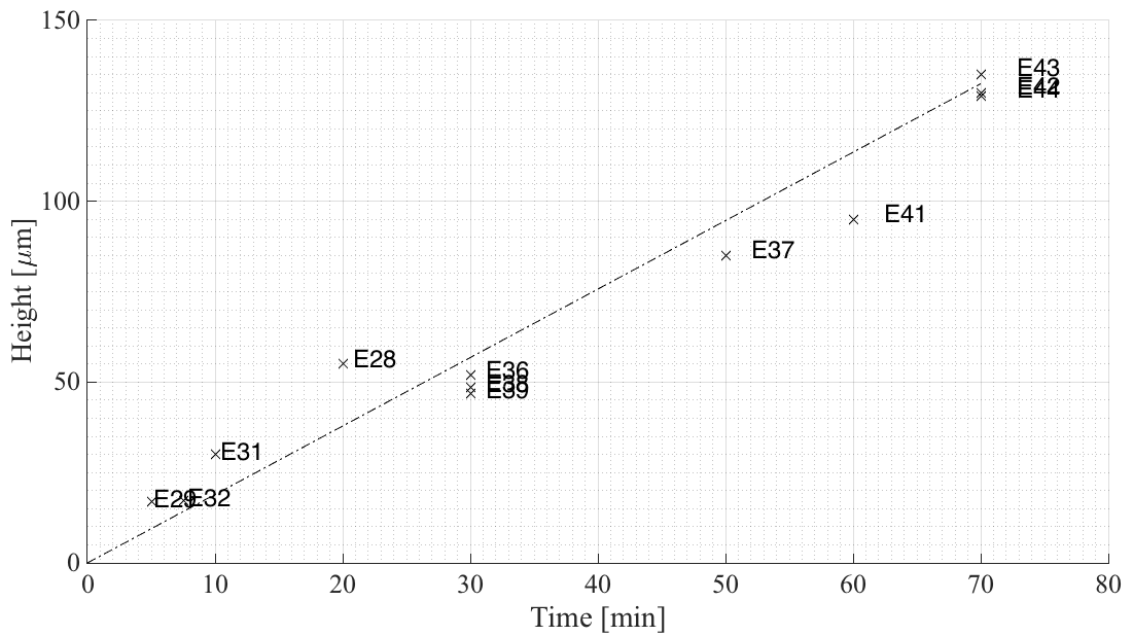
Figure 7.6: Etching depth/cone height by etching time. Linear helpline plotted, not related to data.

ID	t [min]	H [μm]	D [μm]	P [μm]	BS	ER [$\mu m s^{-1}$]	He [sccm]
E00	40	53.16	27.6	32	-	1.3	14.1
E01	30	40	27	29	-	1.3	14.9
E03	10	20	27.5	30	-	2	18.6
E04	20	28.7	26.5	30	-	1.4	16.0
E05	30	39	28.7	29	x	1.3	16.7
E06	20	25	27	27	-	1.3	16.0
E07	10	12.38	26.17	31.5	x	1.2	18.9
E08	20	34	38.4	21	-	1.7	18.6
E09	50	30	-	-	-	-	17.8
E10	10	30	28	40	-	3	9.2
E11	20	46	28.8	39.5	x	2.3	8.9

Table 7.1: Characterisation of the samples. Last column represent the average Helium flow rate during etching. t = etching time, H = height, D = diameter, P = pitch, BS = Black Silicon.

7.2 Micro Pillars Fabrication Results

The results presented in this section have been fabricated while working with the specialization project during the fall of 2015. [111]

All results are presented with numbers and figures in Table 7.1, Figure 7.8, Figure 7.9 and Figure 7.10. A 12.5+/-0.5 μm, and 3.5+/-0.5 μm thick mask is used with samples E00 - E07 and E08 - E11 respectively. The mask thickness was reduced by reason of the high selectivity of the mask. An additional etching step is required to remove the remains of the mask, a thin mask layer after the etching is therefore wanted when a wafer is etched for less than $\approx$ 50 minutes.

Sample E02 has no characterisation data because of a spontaneous end of the etching process due to to high ICP reflected power. The reason for the incident is failure of communication between the software and the hardware, the capacitor's. Hence a control system problem. A solution to the failure is known to be resetting the capacitors by disconnecting the communication cable for 10 seconds and then connect it again. Sample E09 etched through the mask and has therefore no diameter and pitch data. The height can neither be assumed correct.

The undercut defect and the bowing defect are causing most trouble in this context

since a predefined geometry is wanted, i.e. a cylindrical pillar. All wafers have been etched with the same recipe except the number of etching rounds of 10 minutes each, i.e. the etching time. All wafers have been etched with a 16.7% O_2/SF_6 ratio, -120°C and a bias voltage of $\approx$ 10V. Remark: the bias voltage is very sensitive due to its dependence of all the process parameters [91]. Since a carrier wafer is used, the bias voltage cannot be logged. Therefore a test has been done without any wafers, with the RF power (CCP and ICP) used in the recipe.

Undercut and bowing defects can be observed on E04 and E08. Black ilicon is formed on E05, E07 and E11. E10 has some Silicon structures between the pillars. E05 has a new defect not observed before, a second wall layer.

7.2.1   Discussion

The limit for the 3.5 μm mask is not established, but has to be in the interval 30 - 50 μm. A pattern shift in the Helium flow rate can be observed from Figure 7.7 between sample E09 and sample E10. As seen from Figure 7.5, sample E10 and sample E11 have a higher etch rate compared to other samples with the same etching time. This might be because of the lower Helium leakage and therefore less contamination of the gas mix in the chamber.

Even though the bias voltage has been measured without a sample, but with a carrier wafer, the bias voltage cannot be expected constant at 10V.

The etching depth for the samples etched for 10 minutes diverge. Sample E10 might be higher because of the wafer temperature. Sample E07 might be lower due to formation of black Silicon, see Figure 7.9j. Sample E03, E07 and E10 do have approximately the same diameter, though sample E10 has a 10 μm larger pitch. Due to the ARDE effect E10 will have a higher etch rate. The results can therefore not be compared.

Four wafers were etched for 20 minutes. Sample E04, E06 and E08 are gathered around 30+/-5 μm. Sample E04 and E06 have approximately the same pitch, E08 has a smaller pitch and E11 has larger pitch. This affect the etching rate, ref. the ARDE effect. Further E11 has a lower Helium leakage and black Silicon defect, E04 has both undercut and bowing defects. All reasons for a modified etch rate.

Sample E01 and E05 have been etched for 30 minutes. Sample E01 and E05 have the

same pitch and diameter. The black Silicon defect and a new defect not observed before, a second wall layer formed by a passivisation layer, are affecting the etch rate of E01, see Figure 7.8e.

Due to defects, varying conditions, only one data point for 40 and 50 minutes and not equal diameters and pitch, a conclusion of the etch rate cannot be stated. An indication of the etch slope can though be seen (Fig. 7.5).

Undercut and bowing defects can be observed on sample E04 and sample E08. That can be due to gas mixing offset from the Plasmalab 100. A common problem is other gasses from processes done pre etching, i.e. a memory effect. That cannot be the case here because sample E03 is etched just before sample E04. High self bias voltage and too high substrate temperature can also be reasons of the defects.

Since black Silicon is observed for some, but not all wafers, that can be due to the temperature of the wafer, or offset off or wrong gas mixing. Al is known to create micro or nanograss on the etched Silicon surface due to sputtering and redeposition of the Aluminium on the etch field [11] from the dome wall. The black Silicon defect can therefore be related to the carrier wafer. Furthermore, as recommended by Oxford Instruments, the use of a carrier wafer in the etching step should be considered due to the cryo process sensitivity to the wafer temperature. It is not possible to avoid air pockets between the sample wafer and the carrier wafer 100%, a homogeneous temperature in the sample wafer is therefore not reached. The use of a 4" wafer through out the process instead of a 2" wafer will not impact the convenience of the fabrication process noteworthy. Furthermore this will remove the need for a carrier wafer, thermal interface material and reduce grass grow due to Al if a Sapphire carrier wafer is used.
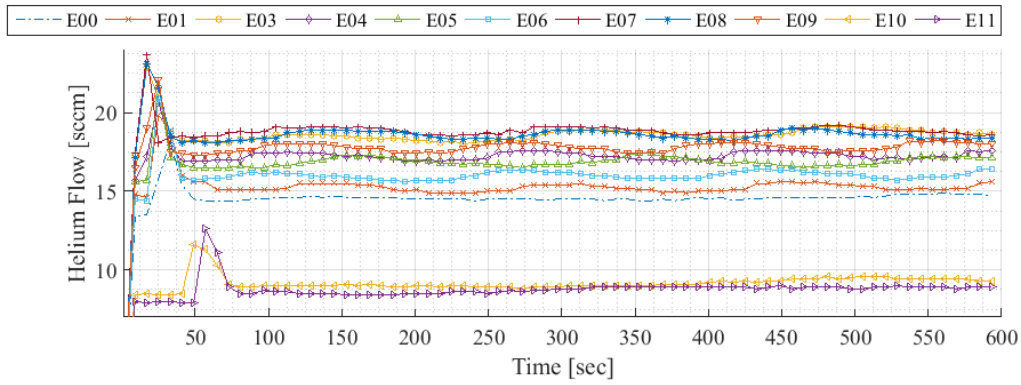
Figure 7.7: Flow rate of Helium to backside of wafer as seen in Fig. 4.8. The flow rate is used as a tool to detect leakages from the backside of the wafer to the chamber. A leakage will affect both wafer temperature and chamber gas mixture.
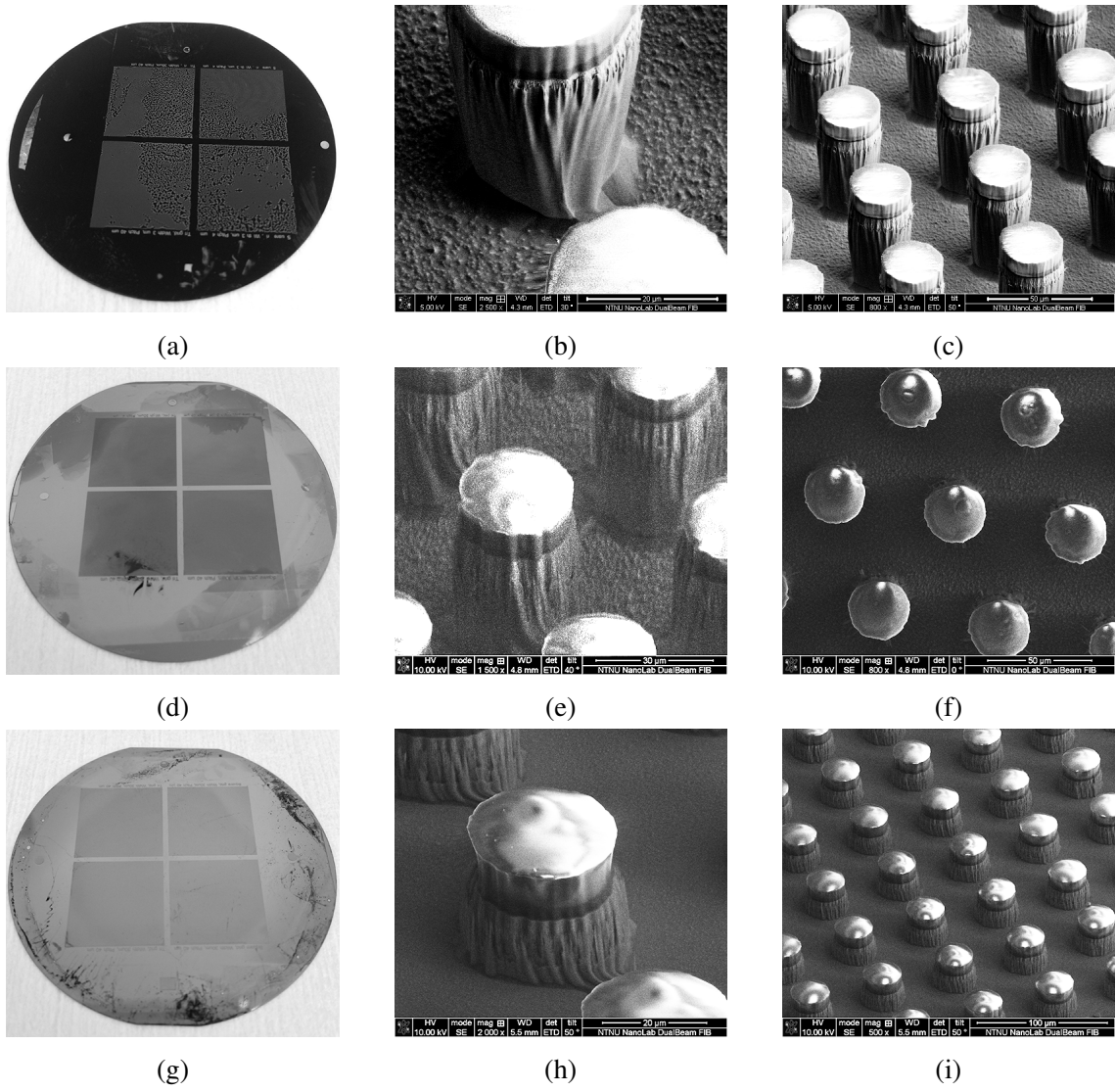
Figure 7.8: (a) E00. (d) E01. (g) E03.
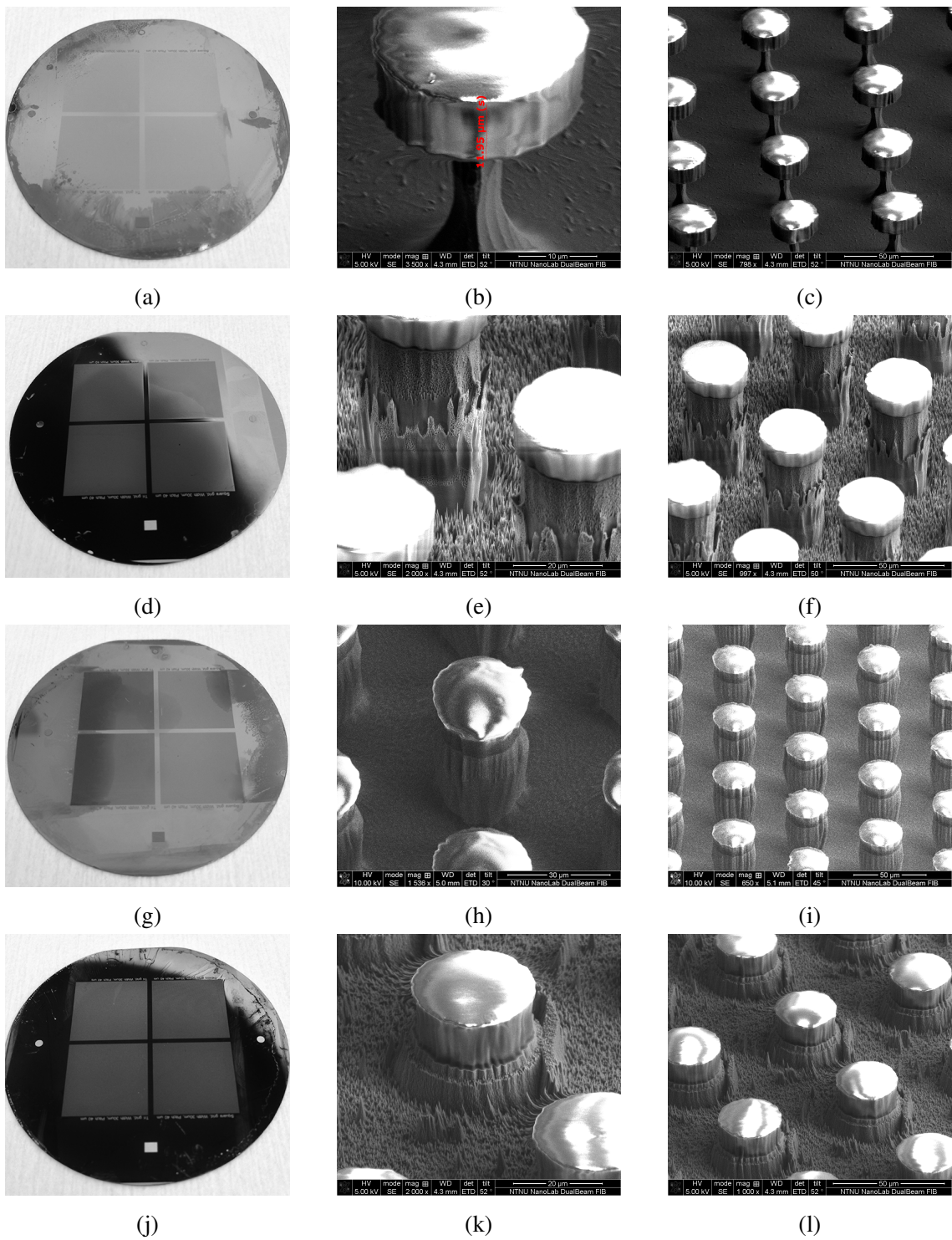
Figure 7.9: (a) E04. (d) E05. (g) E06. (j) E07.
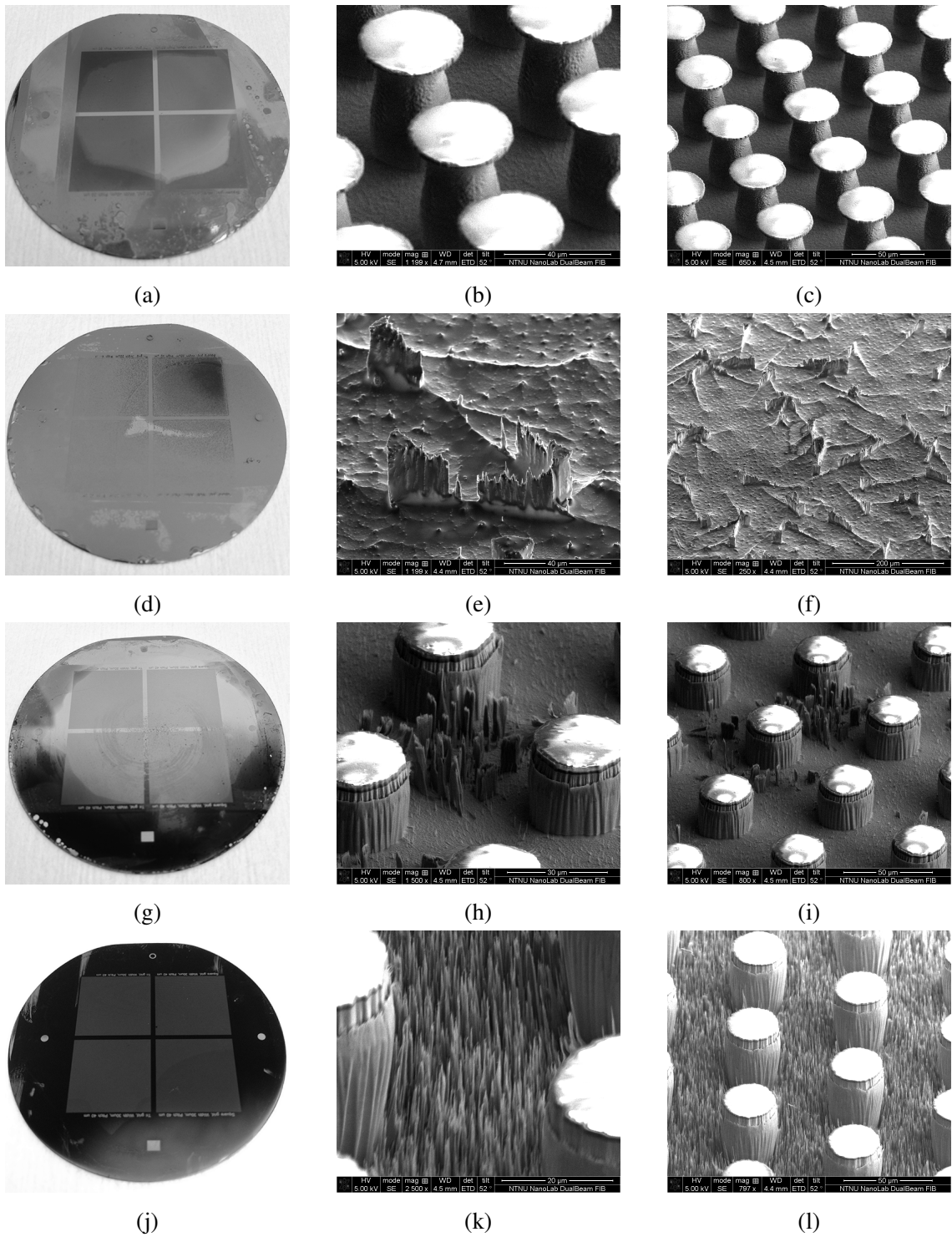
Figure 7.10: (a) E08. (d) E09. (g) E10. (j) E11.

7.3   Micro Cones Fabrication Results

All cones are presented with numbers and figures in Table 7.2, Figure 7.15, Figure 7.16 and Figure 7.17. A 4" chrome glass photomask with 16 different patterns and a 12.5+/-0.5 μm thick SU-8 etching mask is used with all wafers presented in Table 7.2 except sample E45 where no mask is used. All patterns have the same diameter, 10 μm, and shape, circle. The pitch is changing from 5 to 350 μm, see Appendix E for details.

The samples have been fabricated with the same cone recipe as presented earlier and described in detail in Appendix C.10, but with different etching time. It is noteworthy to the reader that cone etching in our work do not use a cyclic etching process as with etching pillars earlier in this work. The mask is removed (cleaned) with a standard ICP-RIE recipe, see Appendix C.9, except samples E29 and E36, where the SU-8 5 mask is etched with a harsh Oxygen plasma to fabricate wires on the cone top surface, Appendix C.12. E39 is etched first in 30 minutes and then 10 minutes with a lower temperature, $-120°C$ to get black Silicon, see Appendix C.13, and then finally cleaned.

ID	t [min]	H [μm]	D_U [μm]	D_L [μm]	ER [$\mu m s^{-1}$]	He [$sccm$]
E28	20	55.2	9	28.8	2.8	26.1
E29	5	16.8	9	19	3.4	29.7
E31	10	30	9.1	24.7	3	23.0
E32	7.5	17.3	7.6	15	2.3	21.7
E36	30	52	6.9	31	1.7	25.9
E37	50	85	5.9	65	1.7	22.8
E38	30	48.4	6.8	44	1.6	20.1
E39	30	46.9	6.4	44	1.6	20.7
E41	60	95	5.0	39.6	1.6	26.3
E42	70	130	-	72.9	1.9	26.6
E43	70	142	-	60	1.9	32.7
E44	70	129	-	58.13	1.8	30.4
E45	10	3	-	-	0.3	33.0

Table 7.2: Characterisation of the samples. t = etching time. H = Height. D_U = Upper Diameter. D_L = Lower Diameter. ER = etching rate. Last column represent the average Helium flow rate during etching.

The samples have a consistent shape and holds none of the typical defects seen while

fabricating pillars. Black Silicon was not observed for any samples while etching at $-50°C$, $t < 60$ and with 2OW CCP. Black Silicon is observed on samples E41 - E44.

The surface between the cones is not equal through the series. Sample E39 cannot be compared in that subject since it has been through a extra process exactly to achieve black Silicon. The surface is more rough on E28 than E29, E32 and E31. The same can be seen from E38, E36 and E37.

As the etching time reach 10 minutes, steeper cone walls can be observed, compare E29, E32 and E31 with E38, E39, E36 and E37. The thickness of the cone top decrease in diameter with etching time. The ideal top can be seen from sample E42, Figure 7.17e

The samples E41 and E42 had to be etched with 30W CCP due to a dying plasma at 20W CCP because of the high pressure. The increased CCP power caused formation of black Silicon on the surface between the cones. The shape of E41 and E42 are consistent with the other samples.

With the samples E43 and E44 the pressure was increased step by step from 50 mTorr at strike to 75 mTorr at etching while holding a CCP power of 20 W to avoid formation of black Silicon. This resulted in less unwanted formations due to black Silicon.
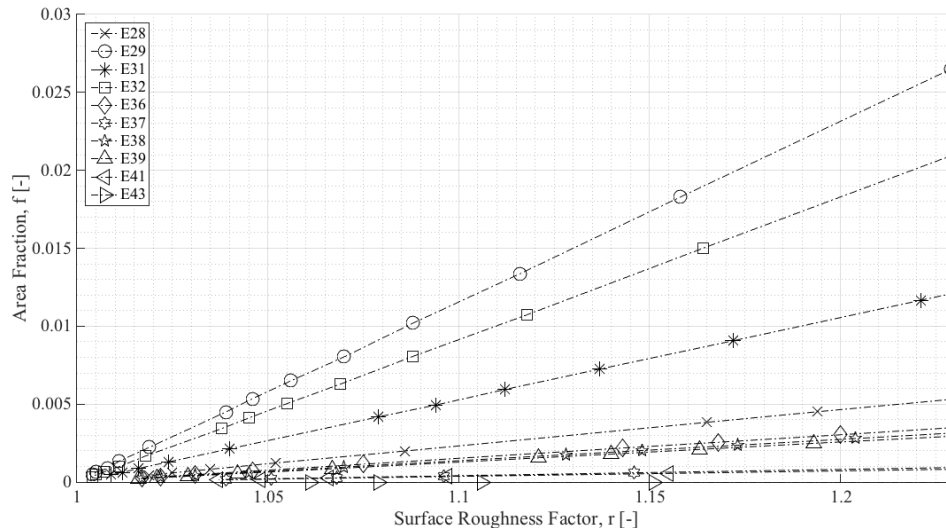
Figure 7.11: Results - Cones. All calculations in Appendix B. See Chapter 2 for r and f definitions.

The top, projected and actual surface, and hence r and f as described in Chapter 2,

for all cones are calculated, see Appendix B, and plotted in Figure 7.11 within the limit, $r < 1.23$, as proposed in Chapter 3. The plot can be explored in detail in the appendix, see Figure A.31 and Figure A.30 in Appendix A.

7.3.1 Discussion

The direct helium cooling on the backside of the wafer, avoided carrier wafer and TIM can be a reason for the consistent shape and the absence of undercut defects. The high O_2/SF_6 gas ratio help avoiding bowing defects.

The cause for the surface defects between the cones can be the amount of sputtered Al onto the substrate at ignition of the plasma, hence 40W CCP power at ignition. The samples E41 and E42 are also etched with with a higher CCP power, 30 W, and the shape of E41 and E42 might therefore be biased by the change in CCP power. A smoother surface or a rougher surface can be adjusted by changing the parameters, e.g. the CCP power. The author suggest to investigate an even lower CCP power for ignition and etching, to avoid unwanted formations.

It can be suggested to use a photomask pattern with a smaller diameter for cones with sub 30 μm height, if a small top diameter is wanted. The cones range in height from 16.8 μm to 142 μm. To the best of the authors knowledge, no cones with such heights have been reported in the literature before. The height, with the recipe used in this work, might reach its limit at 142 μm by reason of lateral etching and hence detaching of the etching mask as seen in Figure 7.17e, where the etching mask has detached and can be observed on the cone wall. The limit can be explored further by increasing the diameter of the photomask pattern, nevertheless out of scope of this work.

Cones fabricated in this work cover the area in the $r - f$ plot proposed in Chapter 3 good. This work is therefore a valuable basis for further work in the subject area. If a smooth surface is wanted between the main cones, the CCP power and etching temperature should be further investigated. That is because those parameters are main driver of Al sputtering from the ICP-RIE dome and hence creation of an Al mask on the substrate. It can be difficult to ignite the plasma at a high pressure, e.g. 75 mTorr, and a low CCP power. We then suggest to set the CCP power low, e.g. 8W, and the pressure low at ignition, e.g.

50 mTorr. Furthermore, increase the pressure stepwise increasing with 2 mTorr at each step to keep the plasma alive.

When a smooth surface and wanted big cones are fabricated with success, small structures with a controllable height, but non controllable pitch and pattern, can be fabricated by changing the CCP power and etching temperature so Al is sputtered from the dome and hence black Silicon is fabricated. Then the height of the structures between the big cones can be controlled.

If structures between the big cones in a given pattern are wanted, another photomask with a given pattern fitting the first one used 100% can be used, or the fabrication process can be done with an Electron-beam lithography system (EBL) instead. With an EBL system, custom shapes can be drawn into the photoresist with a focused electron beam, typically with smaller feature size than possible with UV exposure.

The cones conducted in our work are fabricated with a continuous etching process in contrast to the cyclic etching process used while fabricating pillars earlier in our work. The argument for etching with a cyclic etching process is to avoid temperature increase of the substrate while etching. A higher etching temperature will increase the lateral etching and hence reduce the possible cone height, but also influence the cone wall angle. It can therefore be suggested to run the cone recipe at a higher temperature with 10 min cyclic etching to attain cones with a sharper shape.
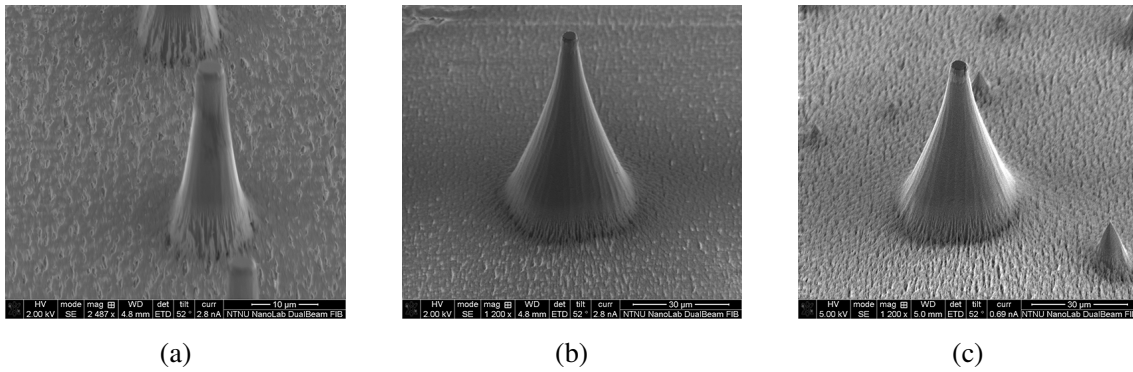
Figure 7.12: (a) E37 - 50 μm pitch. (b) E37 - 200 μm pitch. (c) E37 - 350 μm pitch.
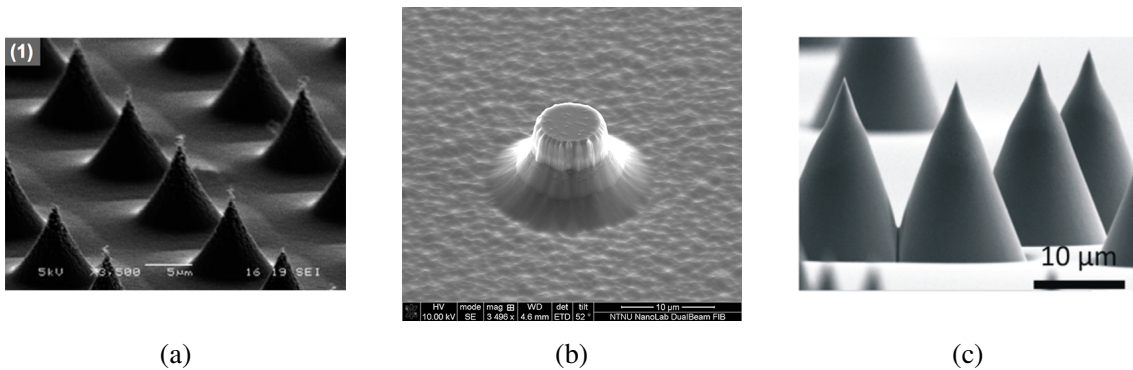
Figure 7.13: (a) Cones fabricated by Arces [17] Etched for 5 min. Height not reported. 10 μm estimated by picture. (b) E29. (c) Cones fabricated by Kondrashov and *Rühe*. [18] Hight not reported. 20 μm estimated by picture.

7.3.2 The ARDE effect

Characterisation of each wafer with SEM is time consuming, 30 min for each pattern, 8 hours for each wafer. The booking rules and availability of the instrument force us to only characterize one pattern of each wafer with the SEM. The pattern with 90 μm pitch is represented in Figure 7.15, Figure 7.16 and Figure 7.17. Because of the ARDE effect, described in Chapter 4, the cone height for each pattern on the same wafer will vary. Three different patterns, 50, 200 and 350 μm pitch are compared in Figure 7.12. They are all from sample E37. In addition we have the values for the 90 μm pitch: 85 μm height. The height of the cones; 34.2 μm, 78.0 μm, 68.5 μm, respectively, underpins the ARDE effect. As CA and LFP are measured after fabrication, the interesting patterns have to be characterized with SEM afterwards.

7.3.3   Comparison With Previous Results

The etching recipe used for the cones in this work uses the same parameters as Arce (2014) [17]. Arce do not mention the size or shape of the mask pattern. Information related to mask removal is either included. The mask thickness is reported to be 1.7 μm and the etching time is 5 minutes. Etching through the mask can therefore be assumed. An Adixen AMS100 SE ICP system is reported to be used in Arces work, equal results can therefore not be expected. As seen from Figure 7.13 the results with equal etching time is quite different. It can be due to different ICP system, photoresist, mask shape diameter or mask thickness. Kondrashov and *Rühe* [18] used a recipe with a lower pressure, 9.75 mTorr, lower temperature, flow rates and CCP power. Their recipe have not been explored since it is based on forming black Silicon and hence no control over pitch. The shape of the cone, see Figure 7.13c, is similar to Figure 7.13a. Since small Al particles sputtered from the dome is the fundamental etching mask for Figure 7.13c, a smaller mask pattern diameter in the work of Arce than in our work is underpinned.

7.3.4   Etching At Room Temperature

The cone recipe has been explored with an ICP-RIE Chiller (Plasmalab 100 - ICP180, Oxford Instruments), the same system as the Cryo, except operating temperature range: $5 - 70°C$, at room temperature condition. Due to too high lateral etching rate, the cone becomes pointed after short time and the SU-8 5 mask detach from the Silicon cone. If the etching continuous after the mask has detached, the result becomes unwanted due to movement of the mask.

The end product after 10, 20 and 30 min can be observed in Figure 7.14c, Figure 7.14a and Figure 7.14b. The etching time with the chiller is therefore limited to sub 10 min and hence the height of the cone is bounded. The height of the samples etched at room temperature could not be measured with accuracy. Observations from Figure 7.14d, Figure 7.14e and Figure 7.14f limit the height to the thickness of the mask. The mask is initially ~12 μm and decrease in thickness as it is etched. The cones observed in Figure 7.14d and Figure 7.14f are therefore limited to 12 μm.
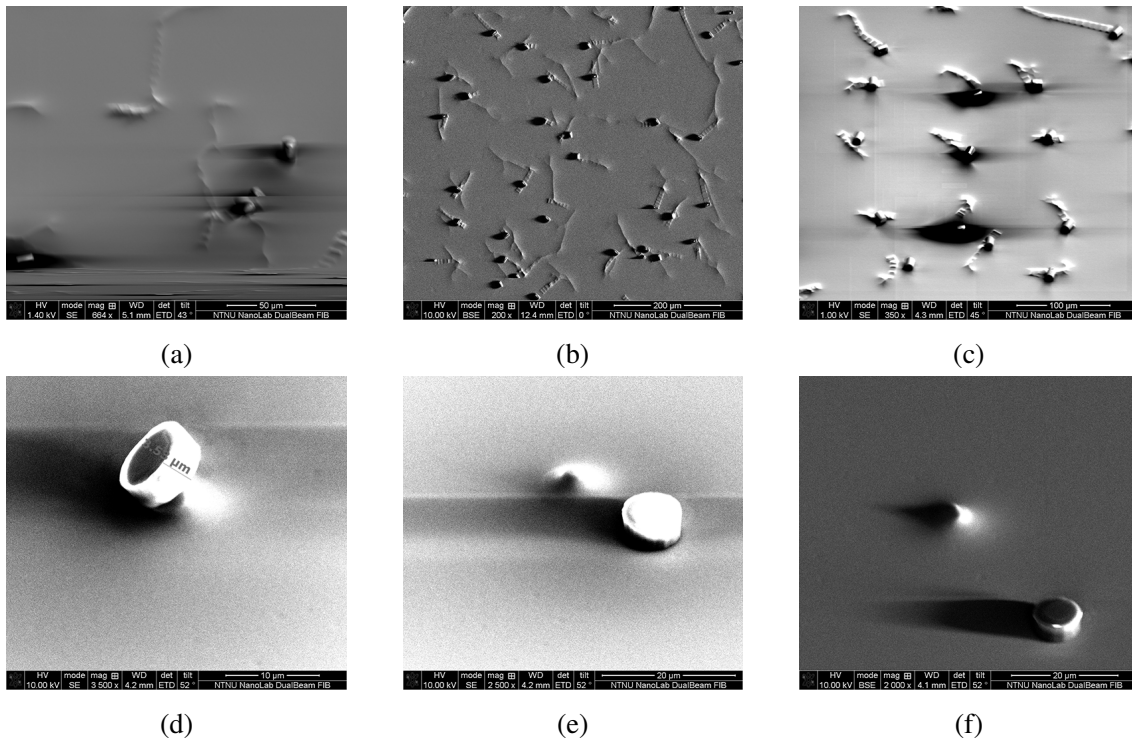
Figure 7.14: (a) E24. (b) E25. (c) E26. (d) - (e) E27. (f) E30

ID	t [*min*]	T [°*C*]	He [*sccm*]
E24	20	20	6.5
E25	30	20	6.5
E26	10	20	6.5
E27	5	10	7
E30	4	10	7

Table 7.3: Wafers etched with the ICP-RIE Chiller at room temperature. t = etching time, T = etching temperature, He = Helium flow rate.
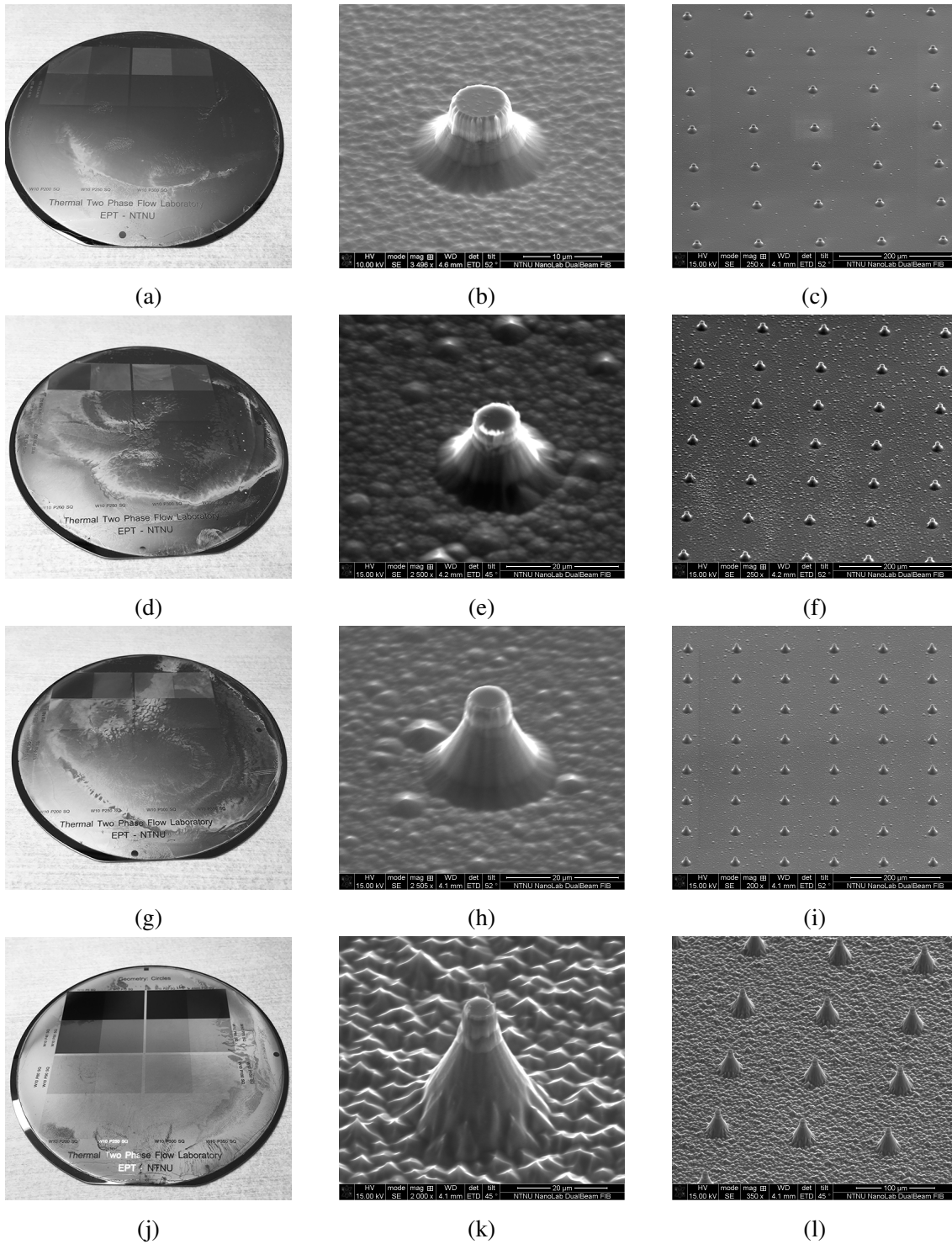
Figure 7.15: (a) - (c) E29 - etched for 5 min. (d) - (f) E32 - etched for 7.5 min. (g) - (i) E31 - etched for 10 min. (j) - (l) E28 - etched for 20 min.
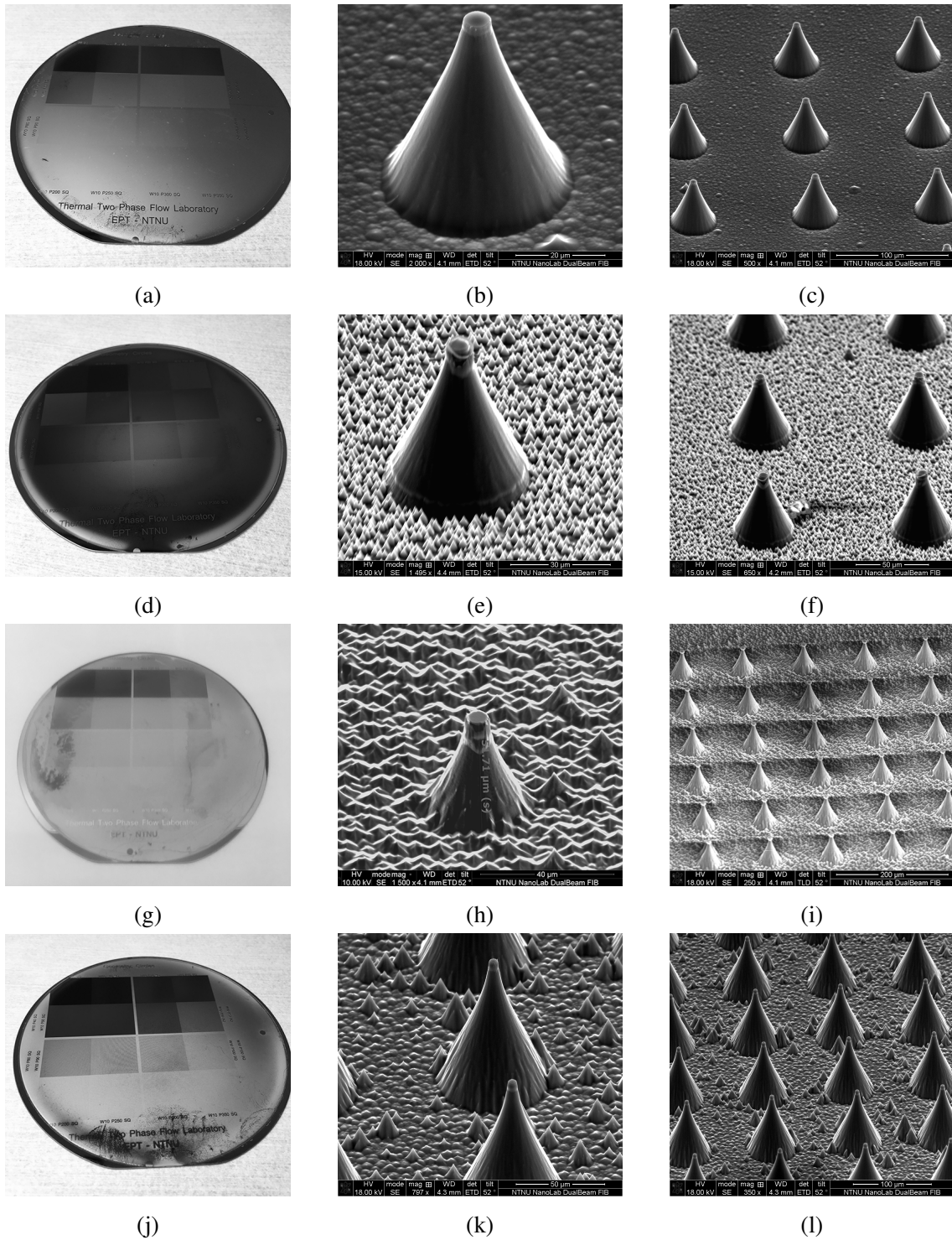
Figure 7.16: (a) - (c) E38. (d) - (f) E39. (g) - (i) E36. All etched for 30 min. (j) - (l) E37 - etched for 50 min.
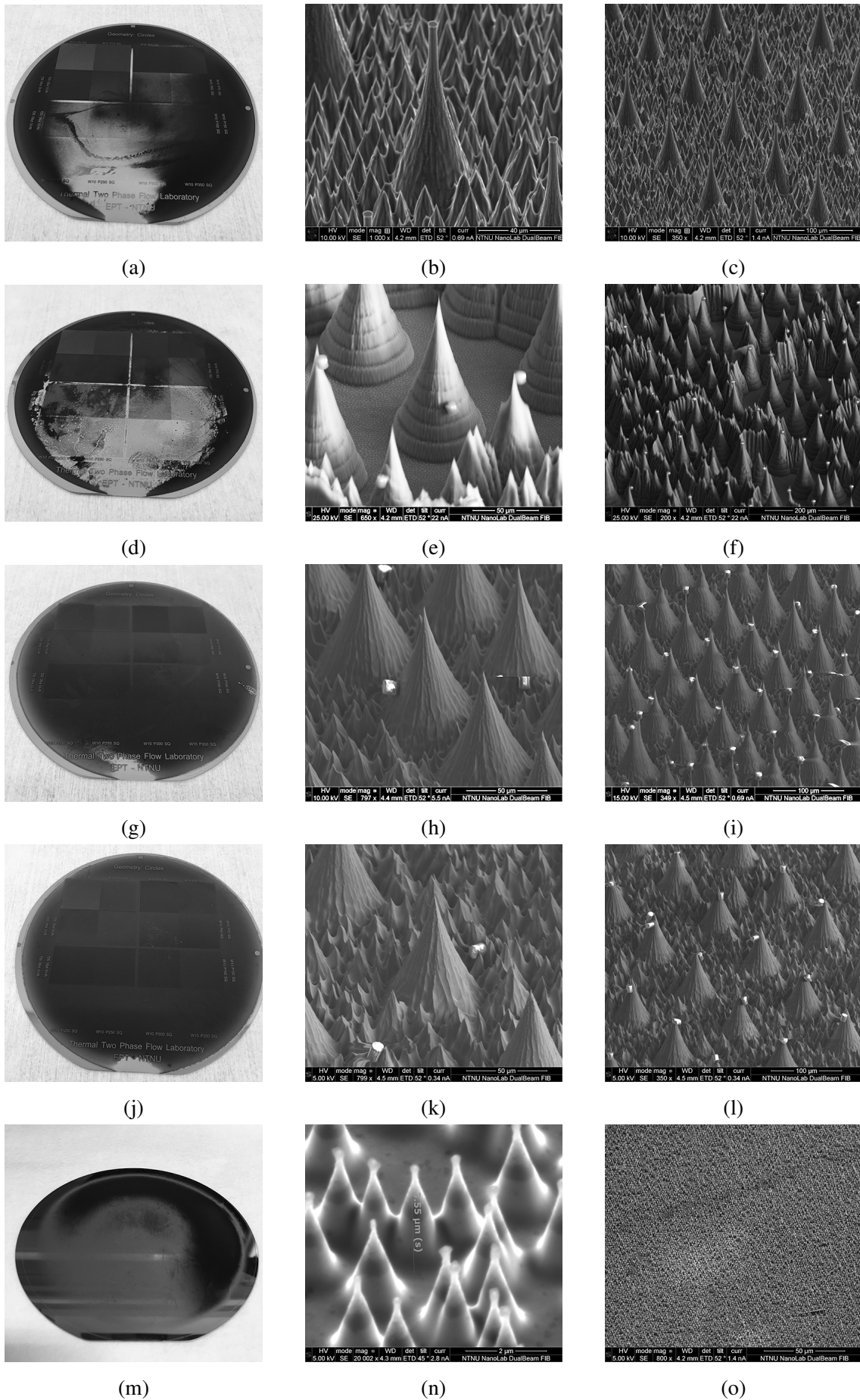
Figure 7.17: (a) - (c) E41 - etched for 60 min. (d) - (f) E42. (g) - (i) E43. (j) - (l) E44. (m) - (o) E45 - etched for 10 min. E42 - E44 are etched for 70 min.
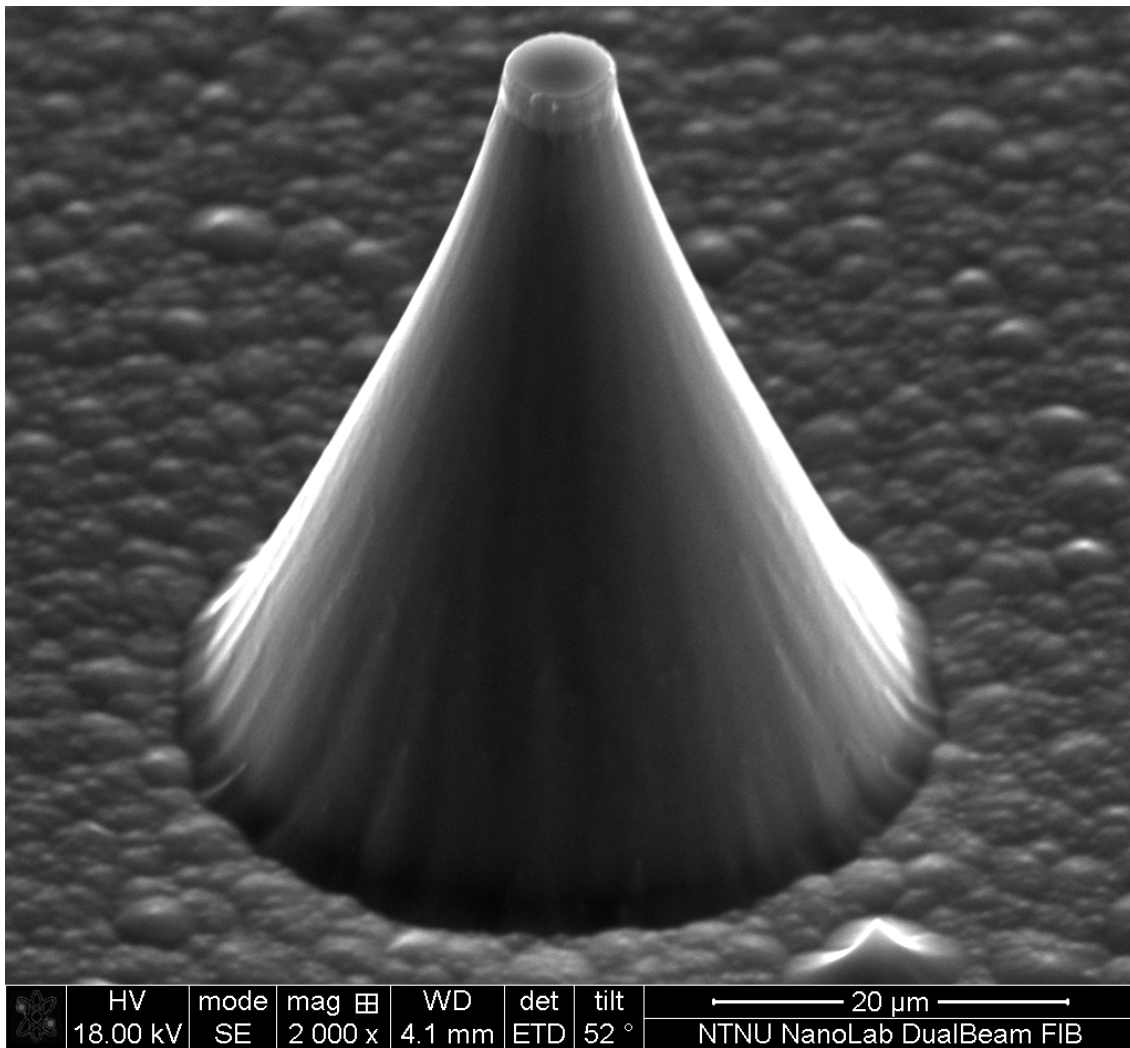
Figure 7.18: E38. Etched for 30 min.

7.4 Carbon Nanowires Fabrication Results

Several attempts to fabricate Carbon nanowires have been conducted according to the recipe described in Chapter 6. Samples E15 - E19 have been fabricated with no photomask and etched with an ICP-RIE Chiller (Plasmalab 100 - ICP180, Oxford Instruments), except sample E18; etched with an Oxygen plasma cleaner (Femto, Diener Electronic). The samples E33 - E35 have been fabricated with the same photomask used for fabricating cones and etched with an ICP-RIE Cryo (Plasmalab 100 - ICP180, Oxford Instruments). The author changed to a photomask with samples E22 and E33 - E35 due to the challenge of observing nanowires with a SEM (FEI Helios NanoLab DualBeam FIB) when no micro structures are present (Fig. 7.19).

It is a challenge to observe any characteristics from Figure 7.19d, Figure 7.19e, Figure 7.19f, Figure 7.19j and Figure 7.19k. With a photomask, SU-8 pillars instead of a SU-8 layer is left after the lithography step. The Oxygen plasma etch will therefore form nanowires on the top surface of the SU-8 pillars. All samples are fabricated as 4" silicon wafers, with ~17 μm photoresist and scribed to 2x2 cm substrates to fit the Calcination Gold Furnace (Fig. 6.3b).

ID	t [min]	T [$°C$]	P [$mTorr$]	ICP [W]	CCP [W]	He [$sccm$]
E15	10	20	50	300	25	6.5
E16	20	20	75	300	25	8
E17	10	20	50	400	20	10
E18	10	-	-	100	-	-
E19	30	20	55	500	20	7.5
E22	30	20	55	300	20	7
E33	30	20	85	300	40	27.4
E34	15	20	85	300	40	23
E35	45	20	85	300	40	23

Table 7.4: t = etching time, T = etching temperature, P = etching pressure, ICP = inductively coupled plasma RF source, CCP = coupled plasma RF source, He = Helium flow rate.

A Energy-Dispersive x-ray Spectroscopy, EDS, (Apollo 10, EDAX Inc) is used for a chemical characterization of the samples in order to state the change of SU-8 5 to Carbon.

Noteworthy, the distance from node to sample, spot size, SEM current and voltage are important for essential EDS parameters; CPS (counts per second, x-ray signal) and DT (dead time). Seen from Figure 7.21 - Figure 7.25, the surface is containing mostly Carbon. The y-axis represent the number of X- rays received and processed by the detector and the x-axis shows the energy level of those counts. The Genesis Edax software do not provide values for the y-axis in numbers. See Figure 7.24a for comparison with pure Silicon. Some Oxygen is still left on the samples. Some Aluminium can be observed, as expected, due to sputtering from the Aluminium Oxide dome, as described earlier in this work. Silicon ca also be observed in the EDS graph, as expected.

7.4.1   Discussion

Oxygen is removed in the $300 - 500^\circ C$ temperature range [109]. It can therefore be suggested to decrease the ramping speed of the pyrolysis process from $300^\circ C$ to $800^\circ C$ or/and increase the holding time at $300^\circ C$.

Even though the change to nanowire fabrication on pillars for samples E22 and E33 - E35, characterization of the nanowire height and thickness could not be completed due to the small scale. Structures in nano scale can be observed from the SEM pictures (Fig. 7.20d, Fig. 7.20e and Fig. 7.20f). Because of the problematic observation conditions of samples E15 - E19, not much can be concluded except that Carbon is formed. Any conclusion regarding optimal Oxygen plasma recipe for fabricating nanowires can therefore not be stated. A SEM with in-lens cold field emission electron microscope should be used to characterize the nanowires due to a higher resolution, 0.4 nm. The SEM (FIB) used in our work has a maximum, best case resolution of 1.2 nm.

The mechanical and electrical properties of pyrolyzed Carbon depend on the pyrolysis temperature [108]. Therefore several different pyrolysis recipes should be further explored.
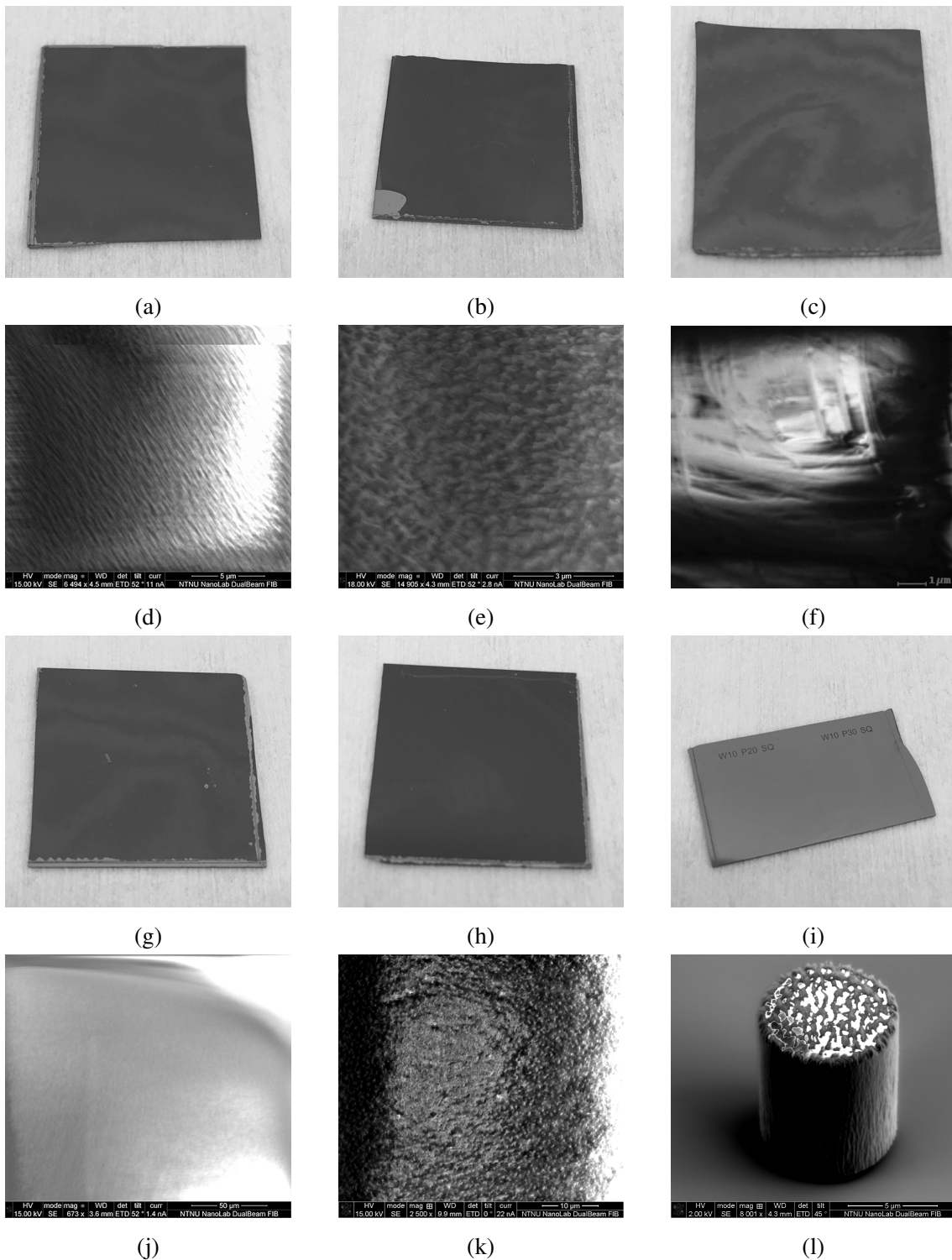
Figure 7.19: Samples after Oxygen plasma etching and pyrolysis process, SEM. (a) & (d) E15. (b) & (e) E16. (c) & (f) E17. (g) & (j) E18. (h) & (k) E19. (i) & (l) E22.
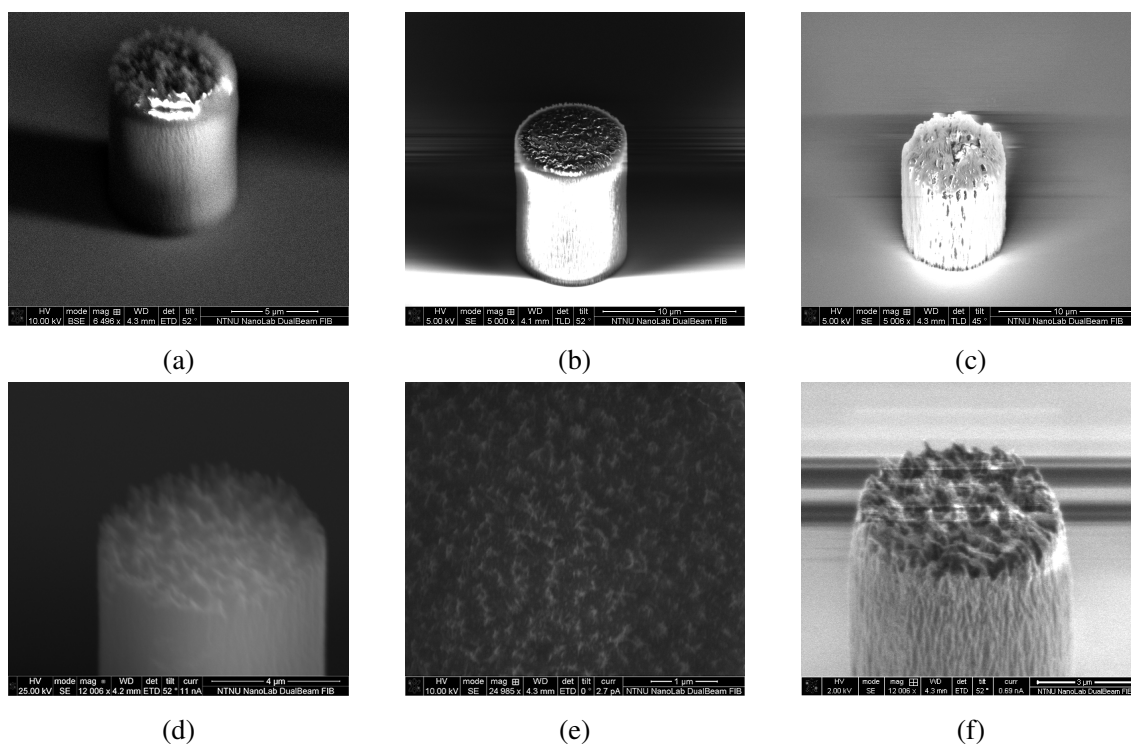
Figure 7.20: (a) E33. (b) E34. (c) E35. After Oxygen plasma treatment, before pyrolysis process. (d) E33. (e) E34. (f) E35. After pyrolysis process.
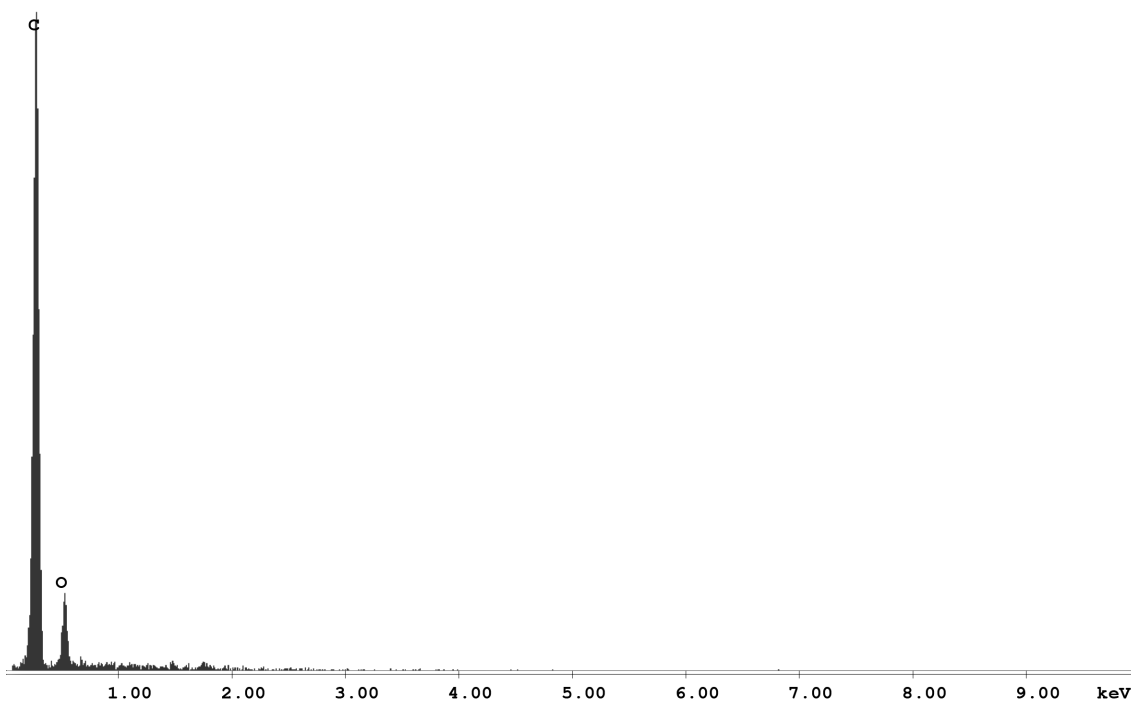
(a)
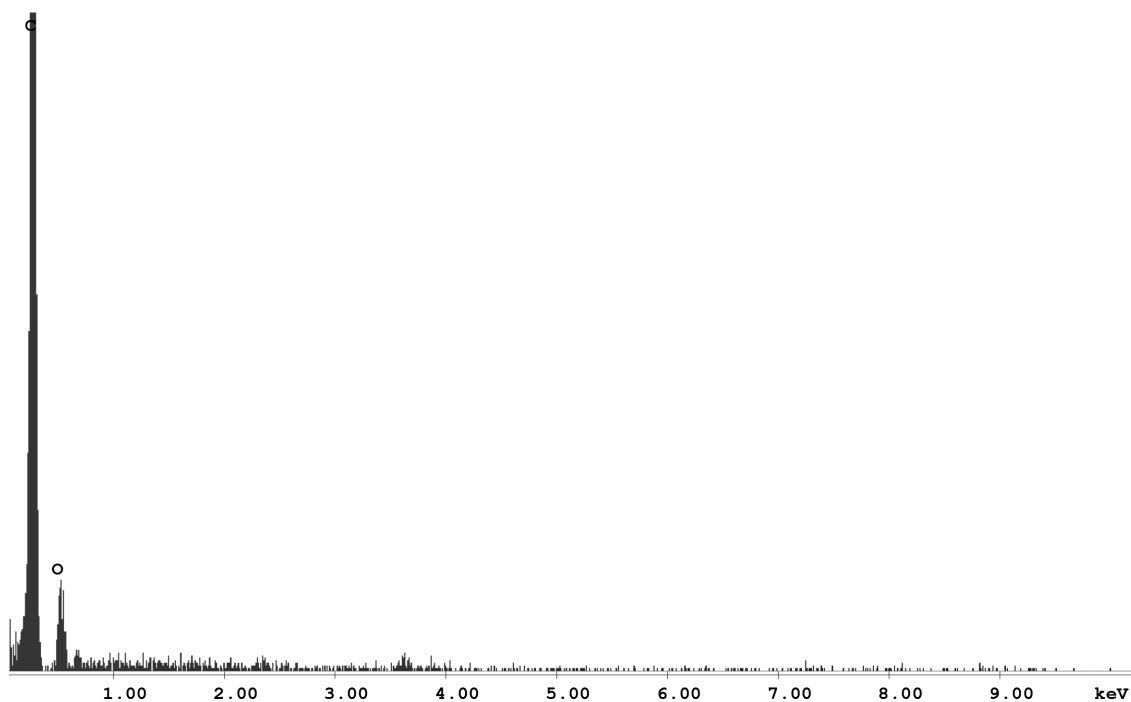
(b)

Figure 7.21: EDS characterization. (a) E15. (b) E16. The y-axis represent the number of X- rays received and processed by the detector and the x-axis shows the energy level of those counts. The Genesis Edax software do not provide values for the y-axis in numbers.
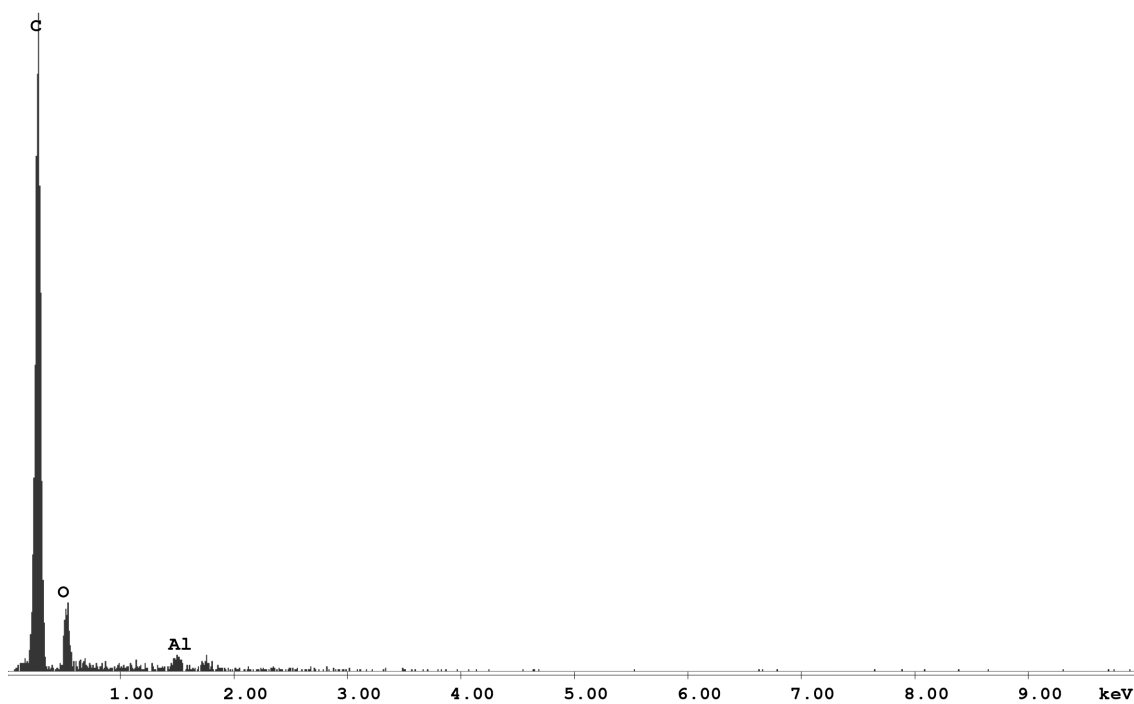
(a)
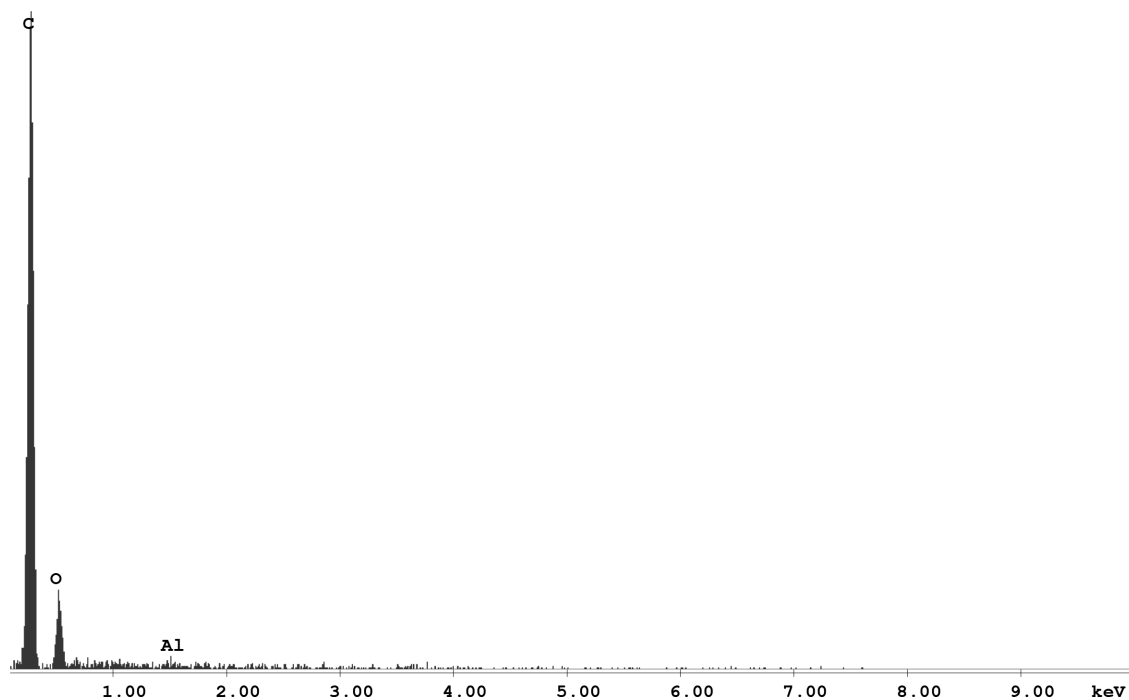
(b)

Figure 7.22: EDS characterization. (a) E17. (b) E18. The y-axis represent the number of X- rays received and processed by the detector and the x-axis shows the energy level of those counts. The Genesis Edax software do not provide values for the y-axis in numbers.
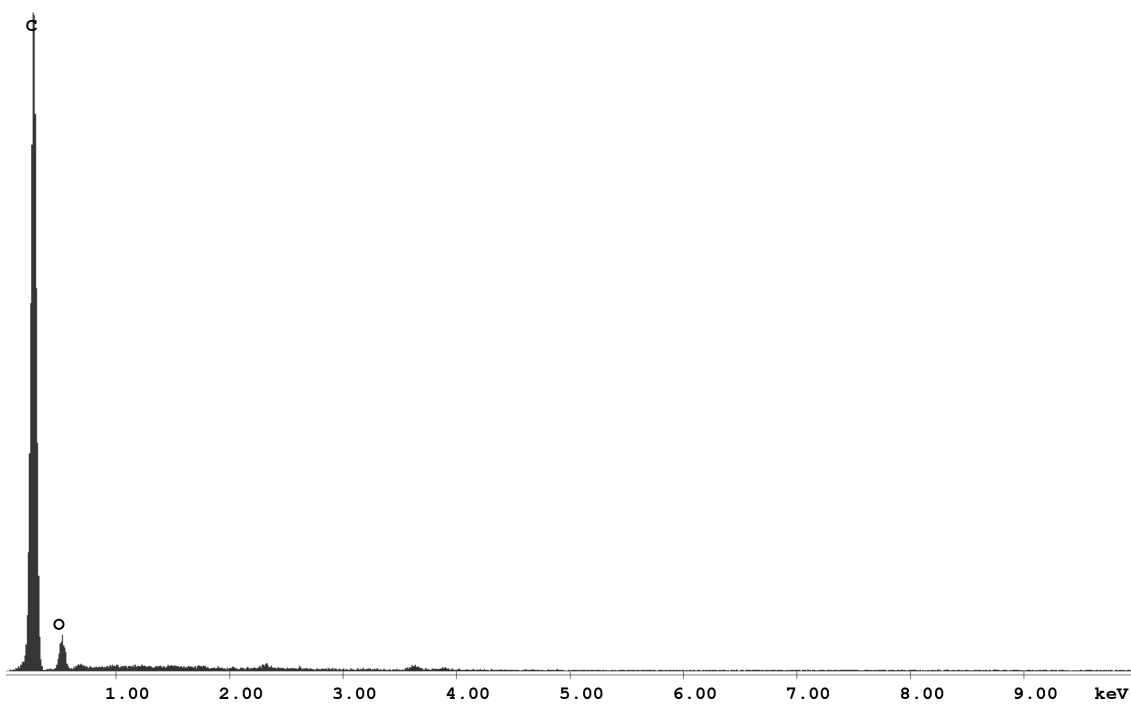
(a)
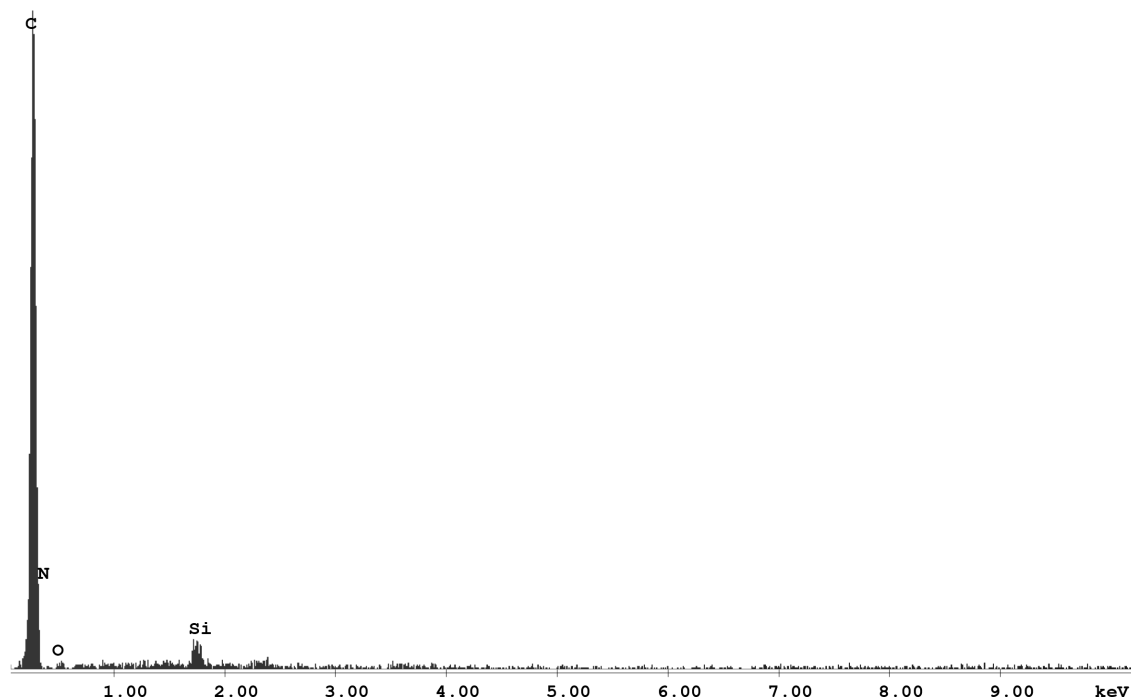
(b)

Figure 7.23: EDS characterization. (a) E19. (b) E22. The y-axis represent the number of X- rays received and processed by the detector and the x-axis shows the energy level of those counts. The Genesis Edax software do not provide values for the y-axis in numbers.
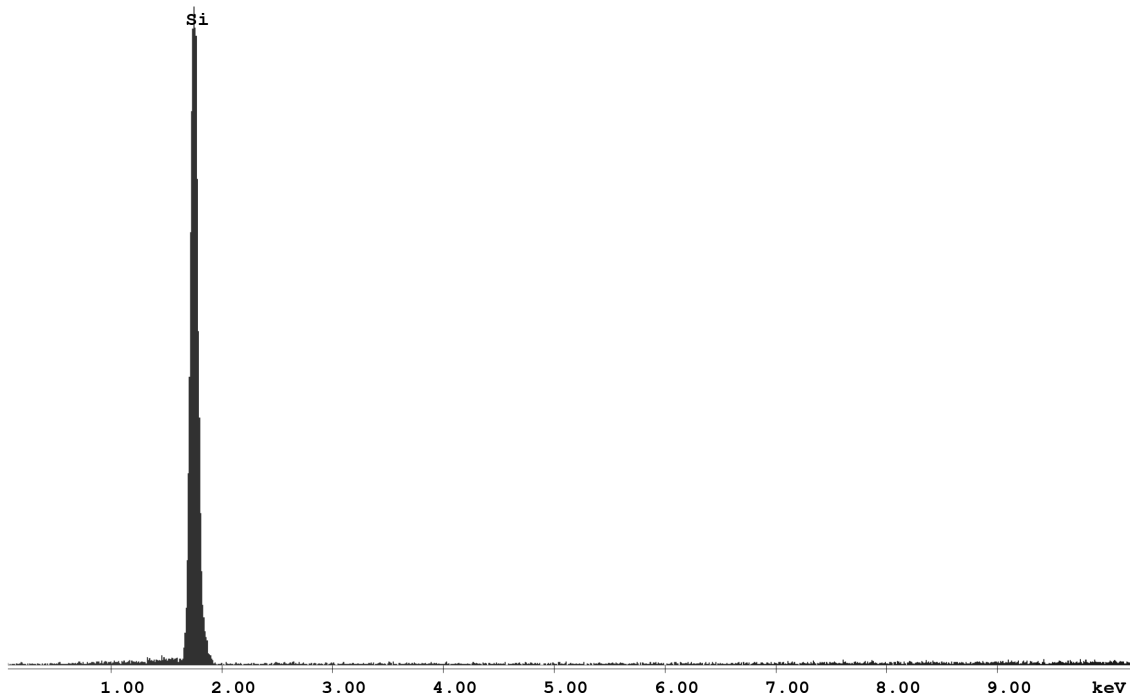
(a)
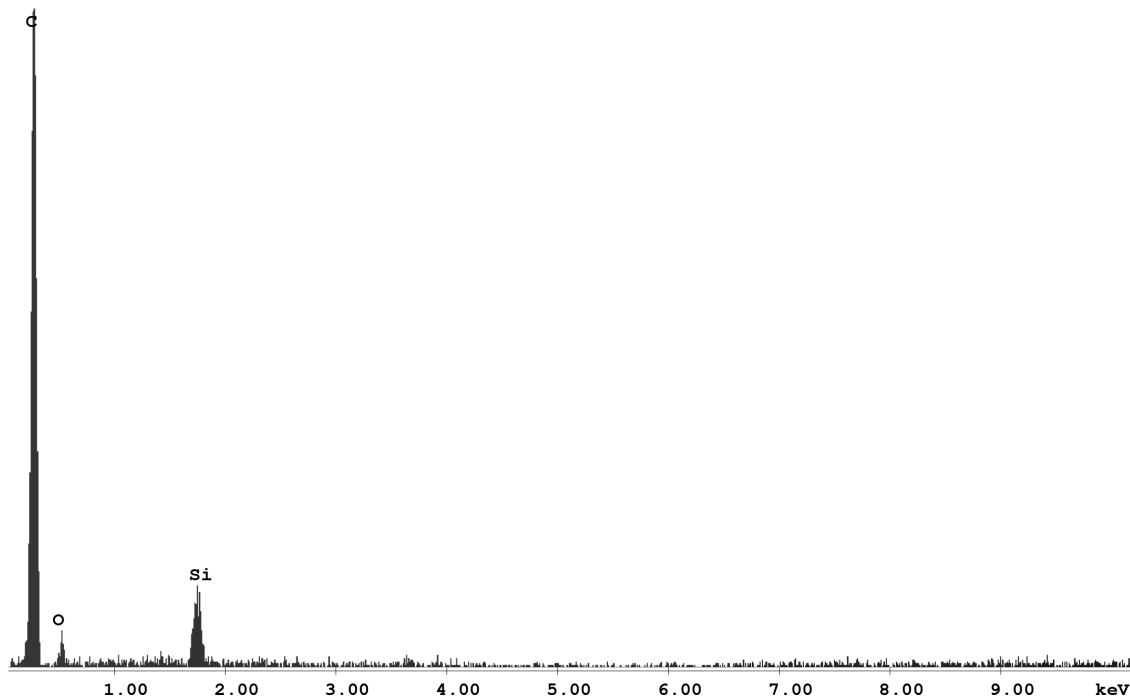
(b)

Figure 7.24: EDS characterization. (a) E41. (b) E33. The y-axis represent the number of X- rays received and processed by the detector and the x-axis shows the energy level of those counts. The Genesis Edax software do not provide values for the y-axis in numbers.
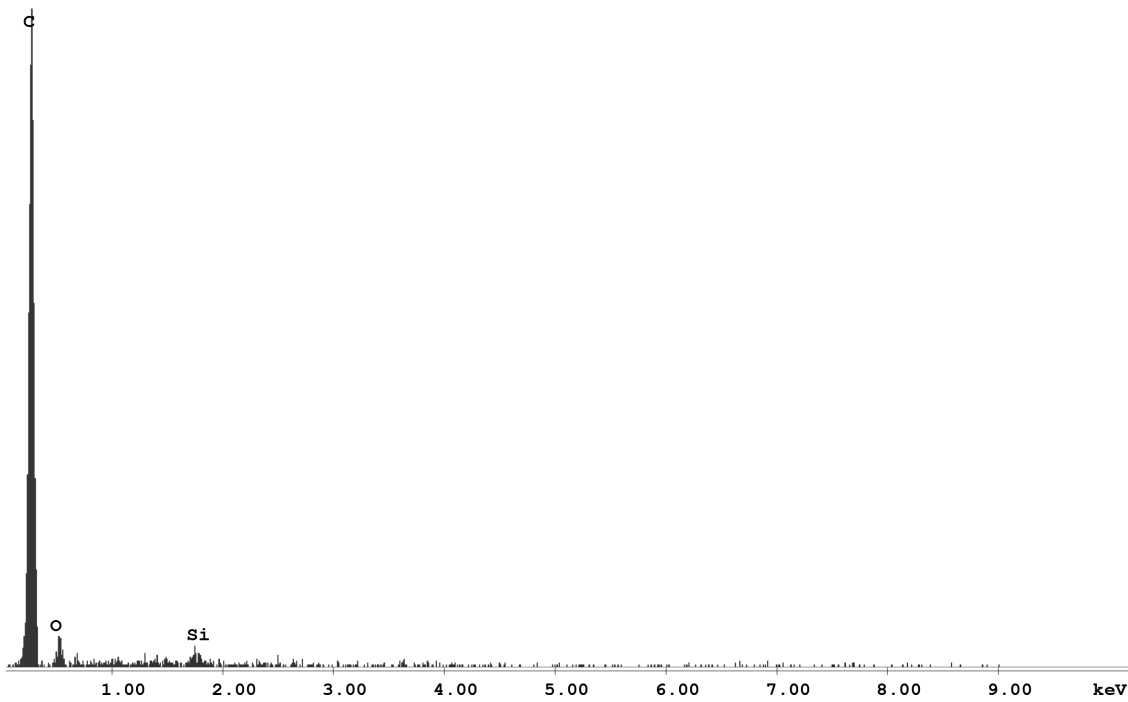
(a)
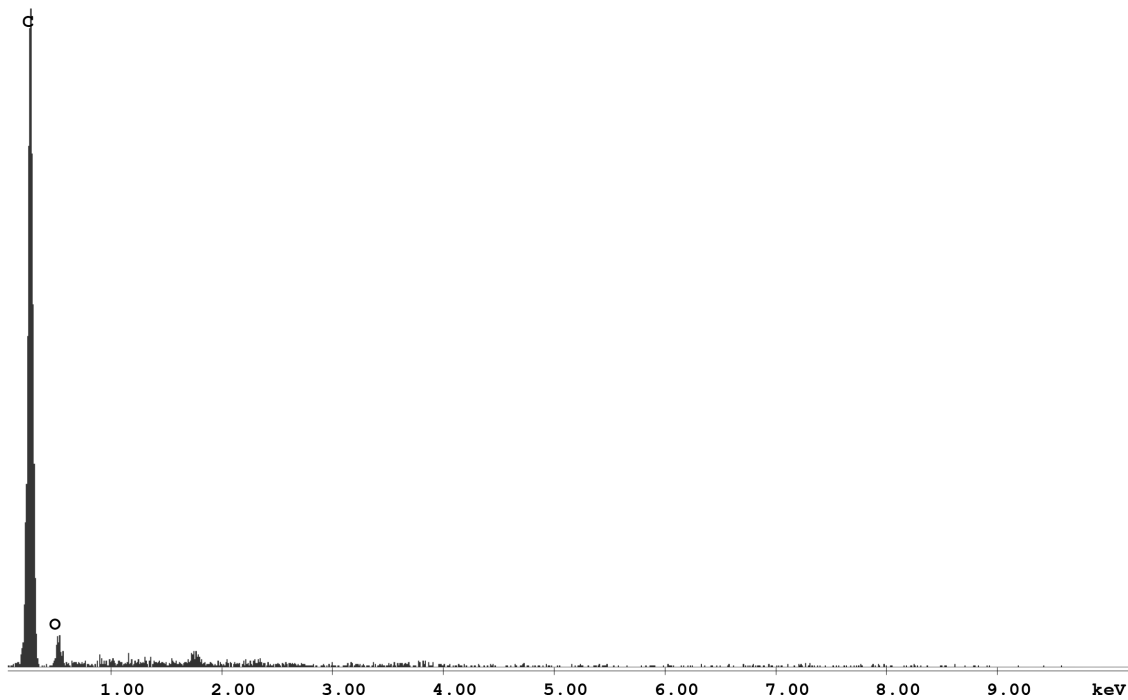
(b)

Figure 7.25: EDS characterization. (a) E34. (b) E35. The y-axis represent the number of X- rays received and processed by the detector and the x-axis shows the energy level of those counts. The Genesis Edax software do not provide values for the y-axis in numbers.

7.5 Hierarchical Structures Fabrication Results

The combination of cones and nano structures from black Silicon and pyrolysis will be presented here. A hierarchical structure can be constructed of cones with nanowires on the surface between the cones, cones with nanowires on top or on cone walls.

ID	t $[min]$	T $[°C]$	P $[mTorr]$	ICP $[W]$	CCP $[W]$	He $[sccm]$
E29	45	20	85	300	40	24.7
E36	30	20	85	300	40	20
E37	20	20	85	300	40	24.4

Table 7.5: t = etching time, T = etching temperature, P = etching pressure, ICP = inductively coupled plasma RF source, CCP = coupled plasma RF source, He = Helium flow rate.

The samples E29-2 and E36-2 (Fig. 7.27c and Fig. 7.27f) are first etched as described earlier for cone fabrication. Then the samples is etched with Oxygen plasma, see Chapter 6. The result can be seen in Figure 7.27. The harsh Oxygen plasma etch, only etching the mask, is forming a porous structure of SU-8 5 nanowires on the cone top, hence a hierarchical structure.

Silicon cones with 3 μm height can be fabricated on the surface between the cones by etching at a lower temperature (-120°C) for 10 minutes, i.e. black Silicon. The result can be seen in Figure 7.26a. Nanowires can be formed on the surface between the cones by adding second photoresist layer on the top of an already etched wafer, E37. Noteworthy, the photoresist did not attach to the cone top or wall surface. After exposure and post-exposure baking the wafer was etched with the Oxygen plasma recipe. The result can be seen in Figure 7.26b and Figure 7.26c. Nanowires of SU-8 5 can be observed. Nanowires could not be formed on the cone walls by this method.

7.5.1 Discussion

The nanowires between cones on sample E37-2 and the wires on the top surface of sample E36-2 have not been characterized due to the small length scale. A SEM with in-lens cold field emission electron microscope should be used to characterize the wires with a higher

resolution, 0.4 nm. The SEM (FIB) used in our work has a maximum, best case resolution of 1.2 nm. If long nanowires are wanted, a thicker photoresist layer should be used, that can be booth for the top cone surface and the surface between cones. The photoresist SU-8 50 can provide a thickness of 40 - 100 μm. The author recommend to investigate fabrication of nano structures on cones by using an EBL system to maintain control over pitch of the nano structures.
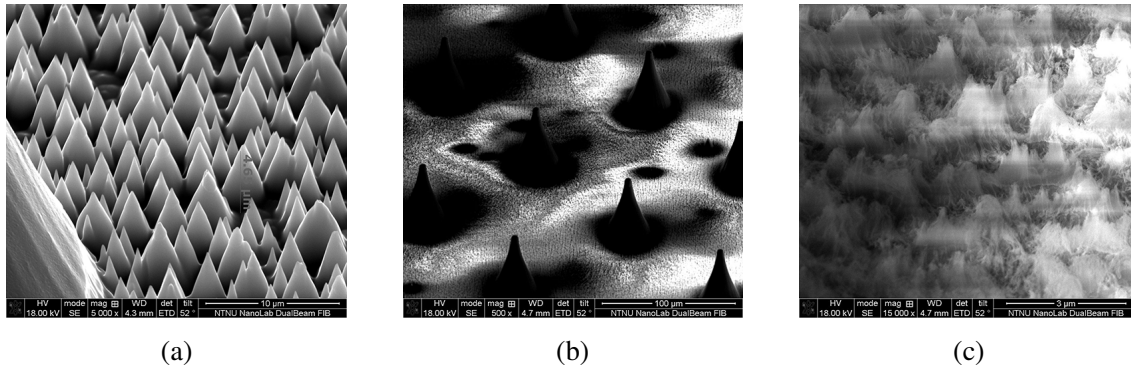
Figure 7.26: (a) E39-2. Small 3 μm cones between 46.9 μm cones. (b) - (c) E37-2. Nanowires between 85 μm cones.

(a)

(b)

(c)

(d)

(e)

(f)
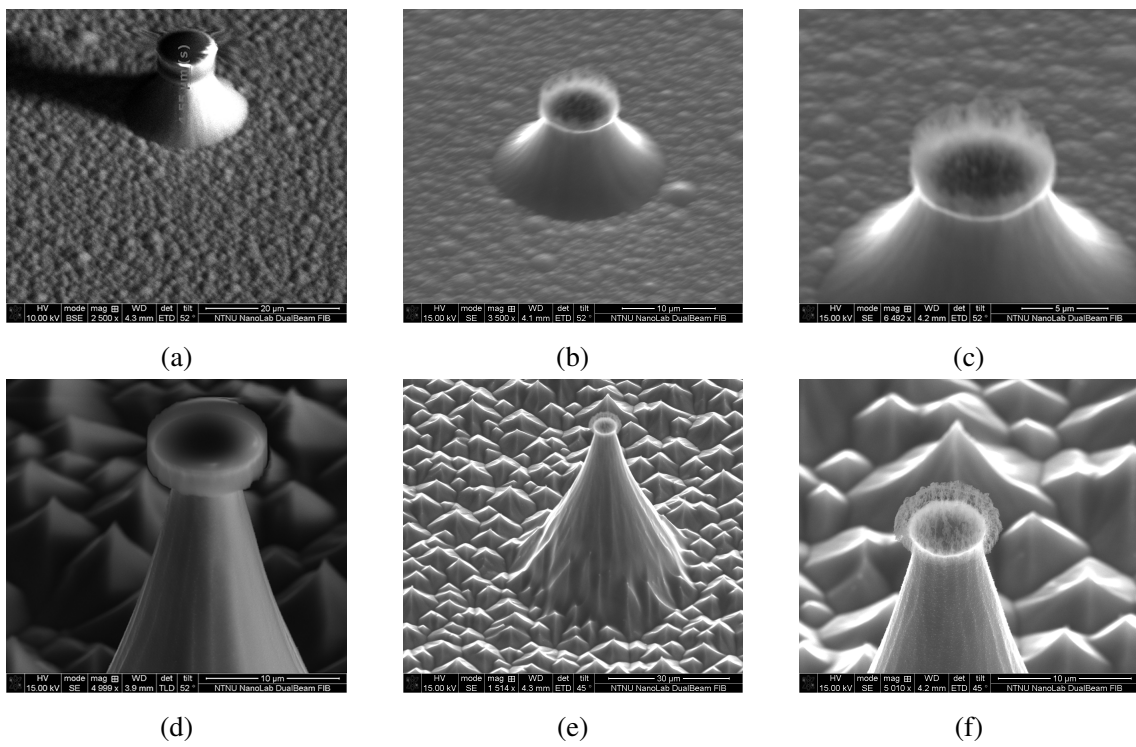
Figure 7.27: (a) - (c) E29-2. (d) - (f) E36-2.

7.6   Anomalous Wetting of Hierarchical Structure

It is out of the scope of this work to do in-depth analysis of the CA and LFP of the samples. Preliminary analysis are conducted due to partial or total wetting of some samples in order to draw some lines for further work.

In this part samples E38, E39 and E45 are compared in order to get an introductory understanding of why sample E39 is totally wetting. Samples E38 (Fig. 7.28a) and E39 (Fig. 7.28b) have been etched with the cone recipe for 30 min, cleaned and has the same cone structures. Furthermore, sample E39 has been etched with the cone recipe at $-120°C$ to get black Silicon and hence formation of small, ~3 μm, cones on the surface in between the big cones, see Figure 7.28b. Sample E45 (Fig. 7.28c) has been through the same cone recipe at $-120°C$, without any mask, and hence have the same surface as sample E39 without the 47 μm high cones.

An optical tensiometer, Figure 7.28g, (Attension Theta, Biolin Scientific, Sweden) is used to characterize the surface. The sample wafer is placed on a brass block, see Figure 7.28h, with 8 cartridge heaters (RAC100L10Ø850W, Lojer Components, U.K.), insulated by 10 mm thick SFC-2 walls (Bagges AS, Norway) and monitored by 5 K-type thermocouples (KMQSS-IM050U-150, Omega, U.K.). The droplet is generated by pushing DI water out of a fine needle (Gastight #1001, Hamilton Co, Reno Nevada, U.S.) at a small rate, see Figure 7.28i. The droplet detaches from the needle due to its own weight, gravity, and falls on the substrate surface with an impact velocity at ambient conditions, i.e. no heating. The tensiometer is used to qualitatively quantify if the substrate is total or partial wetting, i.e. $0°$ or $> 0°$ CA.

It is given attention to if the surface is partial or total wetting only and thought will therefore not be given droplet density, velocity and characteristic length. Figure 7.28d, Figure 7.28e and Figure 7.28f are taken at 32 frames per second (fps) after 10 seconds. The pattern with 90 μm pitch is used with no further argument. The same trend can be observed for all pitches, see Figure 7.29 for three different pitches. Samples E38 and E45 is obviously not total wetting since a droplet with a CA can be observed. Sample E39 is total wetting in 2.4 seconds on average over all 16 patterns with different pitches, see Table

7.6 for all times. The test is repeated five times for the same pitch, E39 - 90 μm pitch, see Figure 7.30. The samples are dried with compressed air between runs.

7.6.1 Discussion

The total wetting of E39 may be related to the combination of micro cone structures of both 47 μm and 3 μm height since either separate do not give a total wetting surface. The result is interesting and should be investigated further. We recommend to repeat the experiment with the exact same characteristics. Also other cone heights both for the big and small structures. The cone heights can be controlled with the recipes developed in this work. Furthermore, the same test, though with nano structures on the top surface of the big cones should be investigated. Sample E37-2 has nanowires between big cones. Will nanowires give the same wetting as the small cones found on sample E39? At last, will the same action be observed if the cone is changed with a cylindrical pillar?

Comprehensive CA and LFP analysis is a natural step for further work. While doing LFP analysis at high temperatures, $> 300°C$, with DI water, the heat flux from the substrate can heat the liquid in the syringe used for depositing droplets. It can be avoided by using a fluid with lower boiling point. Due to FC-72´s low boiling point, 56°C, see datasheet in Appendix **??**, the author of this work recommend to do LFP analysis with FC-72. LFP analysis with Liquid Nitrogen is also a interesting case worth to investigate further due to a boiling point at $-195.8°C$ [112].
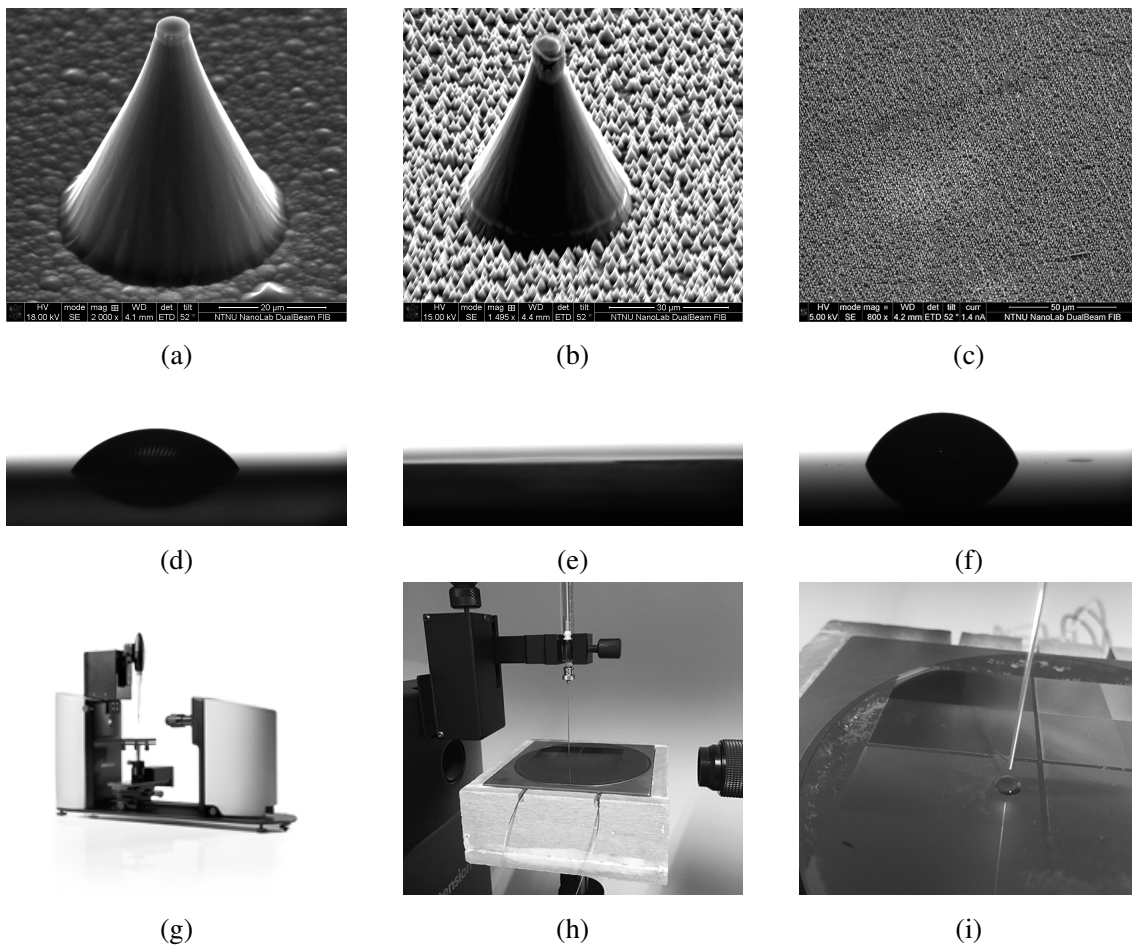
Figure 7.28: (a) and (d) E38. (b) and (e) E39. (c) and (f) E45. (g) Attension Theta, Biolin Scientific, Sweden. (h) Brass block insulated by SFC-2. (i) DI droplet on substrate.

P [μm]	Time [s]
40	1.9
50	2.2
60	1.7
70	2.0
80	6.0
90	2.0
100	3.5
150	2.9
200	0.9
250	0.8
300	3.6
350	1.5

Table 7.6: Time to evaporation of droplet. All done with E39. P = pitch.

(a) t = 0.0625 s   (b) t = 0.5625 s   (c) t = 2.09375 s

(d) t = 3.34375 s   (e) t = 4.28125 s   (f) t = 5.0625 s

(g) t = 0.03125 s   (h) t = 1.4375 s   (i) t = 2.90625 s

Figure 7.29: (a) E39 - 90 μm pitch. Δt = 2.03 s. (d) E39 - 60 μm pitch. Δt = 1.7 s. (g) E39 - 150 μm pitch. Δt = 2.9 s.

(a) t = 0.0625 s   (b) t = 0.5625 s   (c) t = 2.09375 s

(d) t = 0.90625 s   (e) t = 3.28125 s   (f) t = 5.625 s

(g) t = 0.03125 s   (h) t = 2.25 s   (i) t = 4.46875 s

(j) t = 0.03125 s   (k) t = 2.0625 s   (l) t = 4.125 s
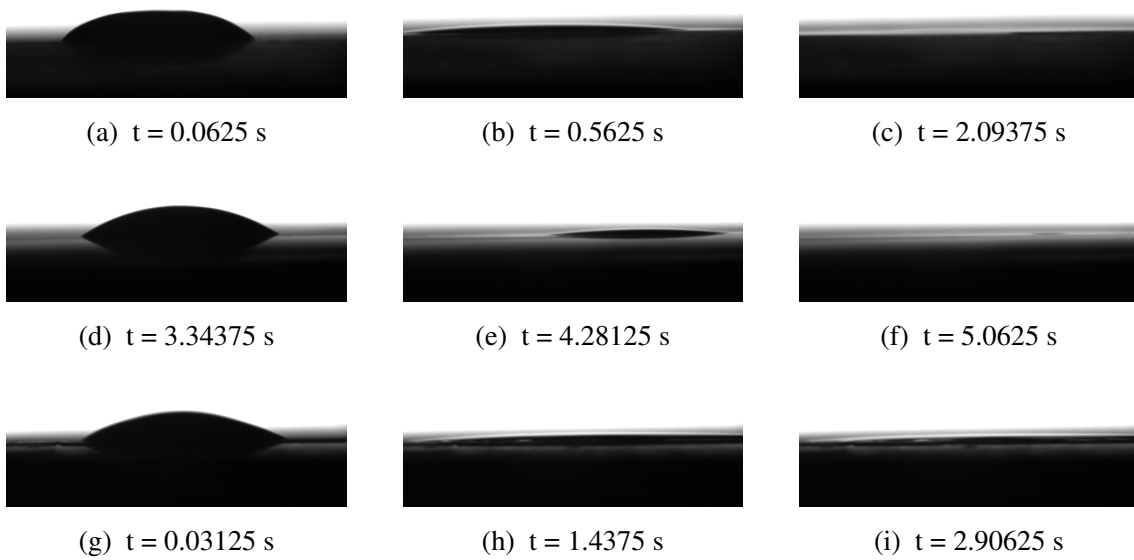
(m) t = 0.03125 s   (n) t = 2.0625 s   (o) t = 4.28125 s
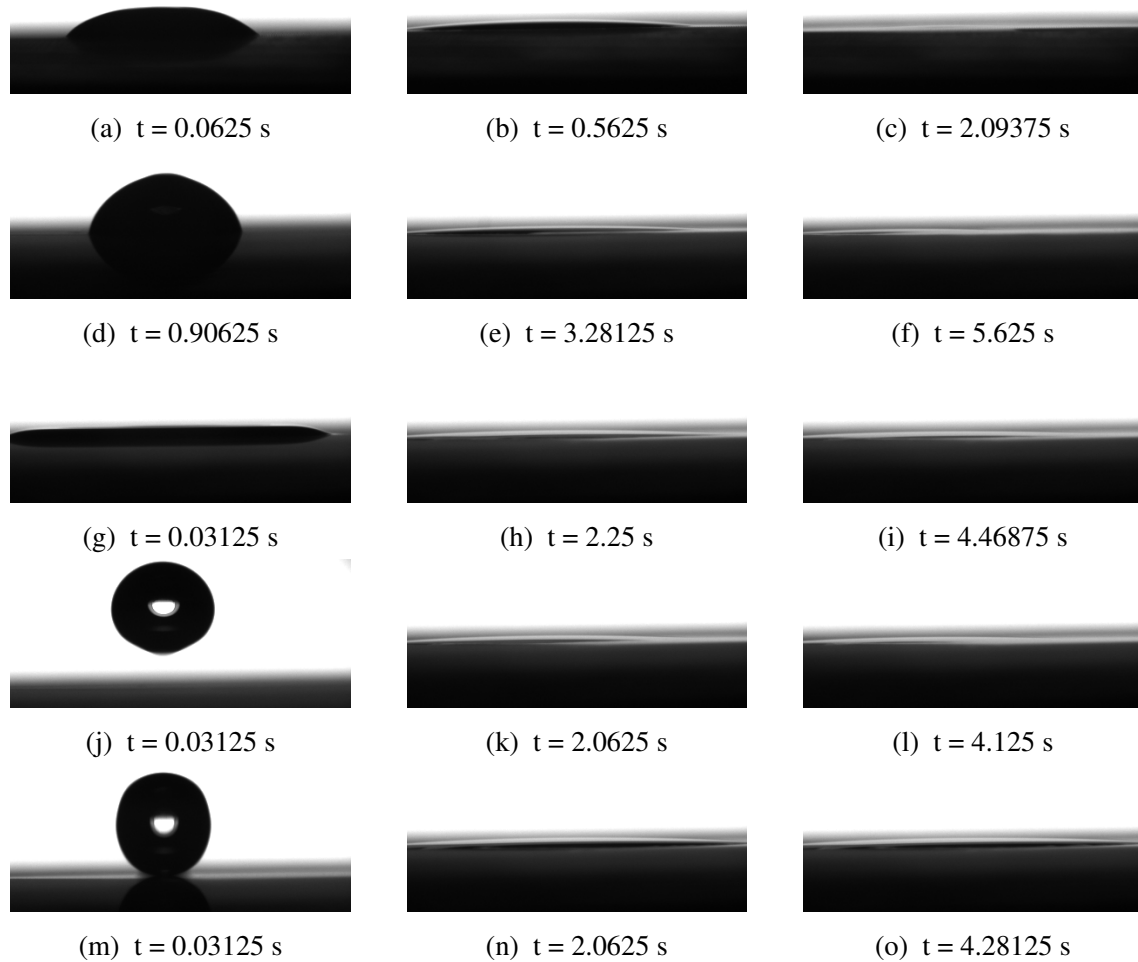
Figure 7.30: All samples are E39 - 90 μm pitch. Wafer dried with compressed air between each test. (a) - (c) Sample 1. (d) - (f) Sample 2. (g) - (i) Sample 3. (j) - (l) Sample 4. (m) - (o) Sample 5.

7.7 Test Facility for Impacting Droplet

An 105mm x 105mm x 40mm brass block for testing 4" wafer samples and an 56mm x 56mm x 35mm brass block for testing 2" wafer samples have been designed with the software Autodesk Inventor (Autodesk Inc., U.S.) and fabricated by the engineering department at NTNU EPT to fit together with an optical tensiometer (Attension Theta, Biolin Scientific, Sweden) for studying impacting droplets over a micro-nano structure surface (Fig. 7.31). See Appendix D for detailed drawings.

The brass block, for 4" wafer samples, is designed to hold 8 cartridge heaters, 5 thermocouples and is insulated by 10mm thick SFC-2 (Bagges AS, Norway) walls on all sides and underneath (Fig. 7.32). SFC-2 is selected as insulation material by cause of its high thermal resistance. The SFC-2 insulation structure is designed by the author and have been delivered by Bagges AS. Eight 100mm long 850W cartridge heaters (RAC100L10Ø850W, Lojer Components, U.K.) have been delivered by Lojer Components Inc.. The distance between the cartridge heaters and the thermocouples is designed to be > 10mm as recommended by Omega Engineering, that is for both brass blocks. The temperature 1.5mm below the top surface of the brass block is monitored by 5 K-type thermocouples (KMQSS-IM050U-150, Omega, U.K.) delivered by Omega Engineering Inc.

The brass block, for 2" wafer samples, is designed to hold 4 cartridge heaters, 3 thermocouples and is insulated by 10mm thick SFC-2 (Bagges AS, Norway) walls on all sides and underneath (Fig. 7.33). Four 50mm long 500W cartridge heaters (RAC2506-50L10Ø500W, Lojer Components, U.K.) have been delivered by Lojer Components Inc.. The temperature 1.5mm below the top surface of the brass block is monitored by 3 K-type thermocouples (KMQSS-IM050U-150, Omega, U.K.) delivered by Omega Engineering Inc.

7.7.1 Discussion

A lexan or plexi cover making it possible to take pictures and still be able to control the atmosphere, i.e. the temperature, humidity and pressure, above the sample wafer will be a natural further step for the test facility.
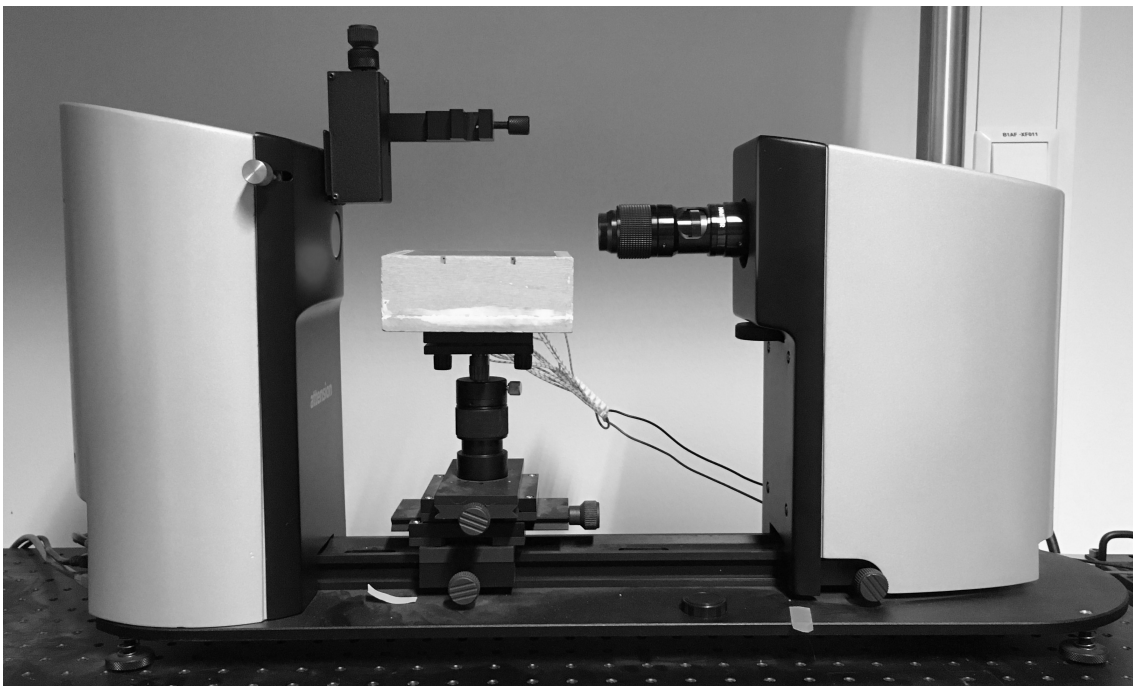
Figure 7.31: Brass block for conducting LFP measurements, 4" wafers. 8 cartridge heaters (RAC100L10Ø850W, Lojer Components, UK), insulated by 10 mm thick SFC-2 walls (Bagges AS, Norway) and monitored by 5 K-type thermocouples (KMQSS-IM050U-150, Omega, UK). Detailed drawings in Appendix D.
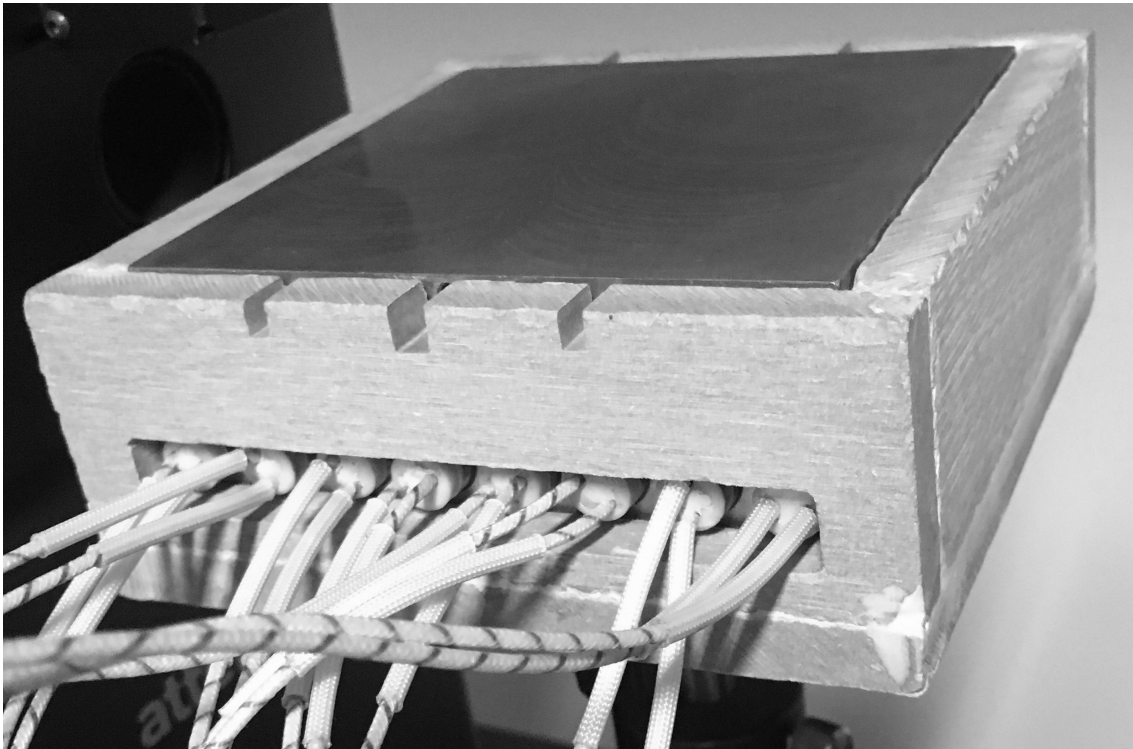
Figure 7.32: Brass block for studying impacting droplets over a micro-nano structure surface, 4" wafers. 8 cartridge heaters (RAC100L10Ø850W, Lojer Components, UK), insulated by 10 mm thick SFC-2 walls (Bagges AS, Norway) and monitored by 5 K-type thermocouples (KMQSS-IM050U-150, Omega, UK). Detailed drawings in Appendix D.

Figure 7.33: Brass block for studying impacting droplets over a micro-nano structure surface, 2" wafers. 4 cartridge heaters (RAC2506-50L10Ø500W , Lojer Components, UK), insulated by 10 mm thick SFC-2 walls (Bagges AS, Norway) and monitored by 3 K-type thermocouples (KMQSS-IM050U-150, Omega, UK). Detailed drawings in Appendix D.

8. Conclusions

The main objective in this work was to (A) identify and (B) fabricate structures for enhancing the Leidenfrost point. The secondary objective was to (C) design and fabricate a test facility for studying impacting droplet over a micro-nano structure surface.

Objective A is reached by (I) a literature review of the relevant literature for controlling the Leidenfrost point with micro-nano engineered surfaces and comprehensive analysis of calculated data, by the author, of surface geometries from the literature and the objective is concluded by using a cone structure with nanowires on its surface for enhancing the Leidenfrost Point.

Objective B is reached by (II) uncovering essential aspects to successfully fabricate the optimal structures, (III) development of a fabrication method for micro pillars with controllable dimensions. The etching step has been identified as the key to fabricate pillars with given characteristics and dimensions. More precise, the temperature of the sample wafer, contamination of the gas mixture from leakages, pressure, bias voltage, CCP power and O_2/SF_6 gas ratio.

Continued by (IV) identification of a fabrication method for cones and exploration of it with respect to etching time. The cone height limit of the method given the selected, designed and fabricated photomask has been identified to be $\approx 142 \mu m$.

A convenient fabrication method (V) for Carbon nanowires using the photoresist SU-8, a harsh Oxygen plasma etch and a pyrolysis process has been identified. Nanowires with unknown length have been fabricated with success, even with an 800°C upper limit oven. Three different possible methods (VI) for fabrication of a hierarchical structure have been explored. A combination of; (i) $\approx 50 \mu m$ and $\approx 3 \mu m$ high cones, (ii) $\approx 50 \mu m$ cones

and nanowires on the surface between the cones, (iii) $\approx 50 \mu m$ cones and nanowires on its top surface. Task (V) and (VI) contribute to the ability of making hierarchical structures, essential for reaching objective B.

Anomalous wetting characteristics (VII) have been identified for a sample with hierarchical structures consisting of 46.9 μm high cones and 3 μm high cones. The sample is compared with a sample with only 48.4 μm high cones and a sample with only 3 μm cones. The result will help to improve the understanding of how surface structures can enhance the Leidenfrost point (B).

A test facility (VIII) for studying impacting droplet over a micro-nano structure surface on a 2" or a 4" wafer has been designed and fabricated with insulation, cartridge heaters, and thermocouples, ready for further work. Objective C is reached by this task.

Lithography and deep reactive ion etching have demonstrated the ability to fabricate surfaces with controllable structures to enhance the characteristics of the surface and hence the Leidenfrost point. Spray cooling as a possible candidate for liquid cooling of microprocessors and other devices with high heat flux and restrictions on operational temperature is strengthened.

8.1   Contributions

- A new method for analyzing geometrical surface structures from different work with respect to the contact surface fraction and the surface roughness fraction is presented.

- This work suggest to define an optimal structure consisting of a micro cone and nanowires for enhancing the Leidenfrost point based on the literature review.

- Helium flow rate from the ICP-RIE is suggested as a post etching analysis tool.

- A method for attaching Carbon nanowires to Silicon pillars is developed.

- A method for fabricating Carbon nanowires between big scale micro cones is developed.

- A improved test facility for studying impacting droplet over a micro-nano structure surface on both 2" and 4" wafers.

Bibliography

[1] NA, "Intel processor clock speed (mhz) i.e. frequency evolution over time," 2014.

[2] G. Moore, "Cramming More Components Onto Integrated Circuits, Electronics,(38) 8," vol. 86, no. 1, pp. 114–117, 1965.

[3] NSA, "2014 edition of moore´s law of intel processors," 2014.

[4] E. S. Fulkerson, S. Telford, R. Deri, A. Bayramian, R. Lanning, E. Koh, K. Charron, and C. Haefner, "Pulsed power system for the hapls diode pumped laser system," in *Pulsed Power Conference (PPC), 2015 IEEE*, pp. 1–6, IEEE, 2015.

[5] "Qcw laser diode." `http://web.archive.org/web/20150508033518/` `http://www.lasertel.com/Products/S15QCWLaserDiode.aspx`, 2016. Accessed: 2016-05-11.

[6] S. G. Kandlikar and A. V. Bapat, "Evaluation of jet impingement, spray and microchannel chip cooling options for high heat flux removal," *Heat Transfer Engineering*, vol. 28, no. 11, pp. 911–923, 2007.

[7] J. D. Bernardin and I. Mudawar, "The Leidenfrost Point: Experimental Study and Assessment of Existing Models," *Journal of Heat Transfer*, vol. 121, no. 4, p. 894, 1999.

[8] D. Attinger, C. Frankiewicz, A. R. Betz, T. M. Schutzius, R. Ganguly, A. Das, C.-J. Kim, and C. M. Megaridis, "Surface engineering for phase change heat transfer: A review," *MRS Energy & Sustainability*, vol. 1, p. E4, 2014.

113

[9] NA, "Microchemicals: Baking steps in photoresists processing," 2015.

[10] L. Sainiemi and S. Franssila, "Mask material effects in cryogenic deep reactive ion etching," *Journal of Vacuum Science & Technology B: Microelectronics and Nanometer Structures*, vol. 25, no. 3, pp. 801–807, 2007.

[11] R. Dussart, T. Tillocher, P. Lefaucheux, and M. Boufnichel, "Plasma cryogenic etching of silicon: from the early days to today's advanced technologies," *Journal of Physics D: Applied Physics*, vol. 47, no. 12, p. 123001, 2014.

[12] K. Koch, I. C. B. A, C. K. B, and S. K. B, "The superhydrophilic and superoleophilic leaf surface of Ruellia devosiana (Acanthaceae): a biological model for spreading of water and oil on surfaces '," *Functional Plant Biology*, vol. 36, pp. 339–350, 2009.

[13] K. Koch and W. Barthlott, "Superhydrophobic and superhydrophilic plant surfaces: an inspiration for biomimetic materials.," *Philosophical transactions. Series A, Mathematical, physical, and engineering sciences*, vol. 367, no. 1893, pp. 1487–509, 2009.

[14] X. Li, "Metal assisted chemical etching for high aspect ratio nanostructures: a review of characteristics and applications in photovoltaics," *Current Opinion in Solid State and Materials Science*, vol. 16, no. 2, pp. 71–81, 2012.

[15] Y. Im, Y. Joshi, C. Dietz, and S. Lee, "Enhanced boiling of a dielectric liquid on copper nanowire surfaces," *International Journal of Micro-Nano Scale Transport*, vol. 1, no. 1, pp. 79–96, 2010.

[16] M. C. Tsai, G. Te Lin, H. T. Chiu, and C. Y. Lee, "Synthesis of zirconium dioxide nanotubes, nanowires, and nanocables by concentration dependent solution deposition," *Journal of Nanoparticle Research*, vol. 10, no. 5, pp. 863–869, 2008.

[17] A. S. Arce, *Switching activation barriers: new insights in E-field driven processes at the interface: perspectives in physical chemistry and catalysis*. PhD thesis, University of Twente, 2014.

[18] V. Kondrashov and J. Rühe, "Microcones and nanograss: toward mechanically robust superhydrophobic surfaces.," *Langmuir : the ACS journal of surfaces and colloids*, vol. 30, no. 15, pp. 4342–50, 2014.

[19] J. R. Thome, "The New Frontier in Heat Transfer: Microscale and Nanoscale Technologies," *Heat Transfer Engineering*, vol. 27, no. 9, pp. 1–3, 2006.

[20] M. I. Flik, B. I. Choi, and K. E. Goodson, "Heat Transfer Regimes in Microstructures," *Journal of Heat Transfer*, vol. 114, no. August 1992, p. 666, 1992.

[21] T. Cader and D. Tilton, "Implementing spray cooling thermal management in high heat flux applications," in *Thermal and Thermomechanical Phenomena in Electronic Systems, 2004. ITHERM'04. The Ninth Intersociety Conference on*, vol. 2, pp. 699–701, IEEE, 2004.

[22] T. Y. Fan and R. L. Byer, "Diode laser-pumped solid-state lasers," *Quantum Electronics, IEEE Journal of*, vol. 24, no. 6, pp. 895–912, 1988.

[23] E. A. Silk, E. L. Golliher, and R. P. Selvam, "Spray cooling heat transfer: technology overview and assessment of future challenges for micro-gravity application," *Energy Conversion and Management*, vol. 49, no. 3, pp. 453–468, 2008.

[24] N. Doerry, J. Amy, and C. Krolick, "History and the status of electric ship propulsion, integrated power systems, and future trends in the us navy," *Proceedings of the IEEE*, vol. 103, no. 12, pp. 2243–2251, 2015.

[25] "Blown away: Hel md destroys mortars midflight." `https://web.archive.org/web/20160422183818/http://www.boeing.com/features/2014/10/bds-helmd-10-13-14.page`, 2016. Accessed: 2016-05-11.

[26] "Lockheed martin demonstrates adam ground-based laser system against military-grade small boats." `https://web.archive.org/web/20160316012012/http://www.lockheedmartin.com/us/news/press-releases/2014/may/0507-ss-adam.html`, 2016. Accessed: 2016-05-11.

[27] "Turning up the heat: Latest evolution of lockheed martin laser weapon system stops truck in field test." `https://web.archive.org/web/20160313225425/http://www.lockheedmartin.com/us/news/press-releases/2015/march/ssc-space-athena-laser.html`, 2016. Accessed: 2016-05-11.

[28] "Turbulence-taming turret: Lockheed martin prototype expands laser performance at jet speeds." `https://web.archive.org/web/20160415010857/http://lockheedmartin.com/us/news/press-releases/2015/october/space-lase-darpa.html`, 2016. Accessed: 2016-05-11.

[29] J. Kim, "Spray cooling heat transfer: The state of the art," *International Journal of Heat and Fluid Flow*, vol. 28, no. 4, pp. 753–767, 2007.

[30] D. E. Tilton, M. R. Pais, and L. C. Chow, "High power density spray cooling," tech. rep., DTIC Document, 1989.

[31] I. Kopchikov, G. Voronin, T. Kolach, D. Labuntsov, and P. Lebedev, "Liquid boiling in a thin film," *International Journal of Heat and Mass Transfer*, vol. 12, no. 7, pp. 791–796, 1969.

[32] W.-L. Cheng, W.-W. Zhang, H. Chen, and L. Hu, "Spray cooling and flash evaporation cooling: The current development and application," *Renewable and Sustainable Energy Reviews*, vol. 55, pp. 614–628, 2016.

[33] T. Cader, L. J. Westra, and R. C. Eden, "Spray cooling thermal management for increased device reliability," *Device and Materials Reliability, IEEE Transactions on*, vol. 4, no. 4, pp. 605–613, 2004.

[34] T. A. Shedd, "Next generation spray cooling: high heat flux management in compact spaces," *Heat Transfer Engineering*, vol. 28, no. 2, pp. 87–92, 2007.

[35] J. G. Leidenfrost, "On the fixation of water in diverse fire," *International Journal of Heat and Mass Transfer*, vol. 9, no. 11, pp. 1153–1166, 1966.

[36] J. D. Bernardin and I. Mudawar, "The Leidenfrost Point: Experimental Study and Assessment of Existing Models," *Journal of Heat Transfer*, vol. 121, no. 4, p. 894, 1999.

[37] C. Lake, "Viscoelastic leidenfrost drops," no. November, pp. 8–10, 2008.

[38] T. Tran, H. J. J. Staat, A. Prosperetti, C. Sun, and D. Lohse, "Drop Impact on Superheated Surfaces," *Physical Review Letters*, vol. 108, p. 036101, jan 2012.

[39] B. Gottfried, C. Lee, and K. Bell, "The leidenfrost phenomenon: film boiling of liquid droplets on a flat plate," *International Journal of Heat and Mass Transfer*, vol. 9, no. 11, pp. 1167–1188, 1966.

[40] D. Quéré, "Leidenfrost Dynamics," *Annual Review of Fluid Mechanics*, vol. 45, no. 1, pp. 197–215, 2013.

[41] Y. Tian, B. Su, and L. Jiang, "Interfacial Material System Exhibiting Superwettability," *Advanced Materials*, vol. 26, no. 40, pp. 6872–6897, 2014.

[42] D. Quéré, "Wetting and Roughness," *Annual Review of Materials Research*, vol. 38, no. 1, pp. 71–99, 2008.

[43] D. Quéré, "Wetting and Roughness," *Annual Review of Materials Research*, vol. 38, no. 1, pp. 71–99, 2008.

[44] Y. He, C. Jiang, S. Wang, Z. Ma, and W. Yuan, "Switch isotropic/anisotropic wettability via dual-scale rods," *AIP Advances*, vol. 4, no. 10, p. 107103, 2014.

[45] E. a. Vogler, "Structure and reactivity of water at biomaterial surfaces.," *Advances in colloid and interface science*, vol. 74, pp. 69–117, 1998.

[46] R. N. Wenzel, "Resistance of solid surfaces to wetting by water.," *Journal of Industrial and Engineering Chemistry (Washington, D. C.)*, vol. 28, pp. 988–994, 1936.

[47] A. B. D. Cassie, "Of porous surfaces,," no. 5, pp. 546–551, 1944.

[48] K. Liu, X. Yao, and L. Jiang, "Recent developments in bio-inspired special wettability," *Chemical Society Reviews*, vol. 39, no. 8, p. 3240, 2010.

[49] J. Bico, C. Tordeux, and D. Quéré, "Rough wetting," *Europhysics Letters (EPL)*, vol. 55, no. July, pp. 214–220, 2001.

[50] S. Adera, R. Raj, R. Enright, and E. N. Wang, "Non-wetting droplets on hot super-hydrophilic surfaces," *Nature Communications*, vol. 4, pp. 1–7, 2013.

[51] T. Tran, H. J. J. Staat, A. Susarrey-Arce, T. C. Foertsch, A. van Houselt, H. J. G. E. Gardeniers, A. Prosperetti, D. Lohse, and C. Sun, "Droplet impact on superheated micro-structured surfaces," *Soft Matter*, vol. 9, no. 12, pp. 3272–3282, 2013.

[52] W. Zhang, T. Yu, J. Fan, W. Sun, and Z. Cao, "Droplet impact behavior on heated micro-patterned surfaces," *Journal of Applied Physics*, vol. 119, no. 11, p. 114901, 2016.

[53] K. Baumeister and F. Simon, "Leidenfrost temperature—its correlation for liquid metals, cryogens, hydrocarbons, and water," *Journal of Heat Transfer*, vol. 95, no. 2, pp. 166–173, 1973.

[54] R. T. Feng, X. D. Wu, and Q. J. Xue, "Profile characterization and temperature dependence of droplet control on textured surfaces," *Chinese Science Bulletin*, vol. 56, no. 18, pp. 1930–1934, 2011.

[55] H. KIM, B. TRUONG, J. BUONGIORNO, and L.-W. HU, "Effects of Micro/Nano-Scale Surface Characteristics on the Leidenfrost Point Temperature of Water," *Journal of Thermal Science and Technology*, vol. 7, no. 3, pp. 453–462, 2012.

[56] H. M. Kwon, J. C. Bird, and K. K. Varanasi, "Increasing Leidenfrost point using micro-nano hierarchical surface structures," *Applied Physics Letters*, vol. 103, no. 20, pp. 2011–2016, 2013.

[57] C. Kruse, T. Anderson, C. Wilson, C. Zuhlke, D. Alexander, G. Gogos, and S. Ndao, "Extraordinary shifts of the Leidenfrost temperature from multiscale micro/nanostructured surfaces.," *Langmuir : the ACS journal of surfaces and colloids*, vol. 29, pp. 9798–806, aug 2013.

[58] G. R. Duursma, R. A. P. Kennedy, and K. Sefiane, "The Leidenfrost Phenomenon on Structured Surfaces," vol. 44, no. September, pp. 7–10, 2014.

[59] D. A. del Cerro, A. G. Marín, G. R. B. E. Römer, B. Pathiraj, D. Lohse, and A. J. Huis in 't Veld, "Leidenfrost point reduction on micropatterned metallic surfaces.," *Langmuir : the ACS journal of surfaces and colloids*, vol. 28, no. 42, pp. 15106–10, 2012.

[60] J. Li, Y. Hou, Y. Liu, C. Hao, M. Li, M. K. Chaudhury, S. Yao, and Z. Wang, "Directional transport of high-temperature Janus droplets mediated by structural topography," *Nat Phys*, vol. advance online publication, feb 2016.

[61] Z. Yoshimitsu, A. Nakajima, T. Watanabe, and K. Hashimoto, "Effects of surface structure on the hydrophobicity and sliding behavior of water droplets," *Langmuir*, vol. 18, no. 15, pp. 5818–5822, 2002.

[62] S. Adera, R. Raj, R. Enright, and E. N. Wang, "Evaporation-Induced Cassie Droplets on Superhydrophilic Microstructured Surfaces," *ASME 2012 10th International Conference on Nanochannels, Microchannels, and Minichannels*, no. m, p. 835, 2012.

[63] S.-S. Liu, C.-H. Zhang, H.-B. Zhang, J. Zhou, J.-G. He, and H.-Y. Yin, "Fabrication of pillar-array superhydrophobic silicon surface and thermodynamic analysis on the wetting state transition," *Chinese Physics B*, vol. 22, p. 106801, 2013.

[64] F. Chen, D. Zhang, Q. Yang, X. Wang, B. Dai, X. Li, X. Hao, Y. Ding, J. Si, and X. Hou, "Anisotropic Wetting on Microstrips Surface Fabricated by Femtosecond Laser," *Langmuir*, vol. 27, no. 1, pp. 359–365, 2011.

[65] Y. He, C. Jiang, S. Wang, Z. Ma, W. Tian, and W. Yuan, "Tailoring Anisotropic Wettability Using Micro-pillar Geometry," *Colloids and Interface Science Communications*, vol. 2, pp. 19–23, 2014.

[66] C. Ma, S. Bai, X. Peng, and Y. Meng, "Anisotropic wettability of laser microgrooved SiC surfaces," *Applied Surface Science*, vol. 284, pp. 930–935, 2013.

[67] D. Quere, A. L. Lafuma, and J. Bico, "Slippy and sticky microtextured solids," *Nanotechnology*, vol. 14, no. 10, pp. 1109–1112, 2003.

[68] K.-H. Chu, Y. S. Joung, R. Enright, C. R. Buie, and E. N. Wang, "Hierarchically structured surfaces for boiling critical heat flux enhancement," *Applied Physics Letters*, vol. 102, no. 15, p. 151602, 2013.

[69] H. Kim, B. Truong, J. Buongiorno, and L.-W. Hu, "On the effect of surface roughness height, wettability, and nanoporosity on leidenfrost phenomena," *Applied Physics Letters*, vol. 98, no. 8, p. 083121, 2011.

[70] M. Shearn, X. Sun, M. D. Henry, A. Yariv, and A. Scherer, "Advanced Plasma Processing: Etching, Deposition, and Wafer Bonding Techniques for Semiconductor Applications," *Semiconductor Technologies*, pp. 79–104, 2010.

[71] G. Fisher, M. R. Seacrist, and R. W. Standley, "Silicon crystal growth and wafer technologies," *Proceedings of the IEEE*, vol. 100, no. SPL CONTENT, pp. 1454–1474, 2012.

[72] T. Zijlstra, E. Van der Drift, M. J. A. de Dood, E. Snoeks, and A. Polman, "Fabrication of two-dimensional photonic crystal waveguides for 1.5 μm in silicon by deep anisotropic dry etching," *Journal of Vacuum Science & Technology B: Microelectronics and Nanometer Structures*, vol. 17, no. 6, pp. 2734–2739, 1999.

[73] L. Sainiemi, *Cryogenic Deep Reactive Ion Etching of Silicon Micro and Nanostructures*. 2009.

[74] M. J. Walker, "Comparison of Bosch and cryogenic processes for patterning high aspect ratio features in silicon," *Proceedings of SPIE*, vol. 4407, no. 0, pp. 89–99, 2001.

[75] F. Laermer and A. Schilp, "Method for anisotropic plasma etching of substrates," Mar. 12 1996. US Patent 5,498,312.

[76] S. Tachi, K. Tsujimoto, and S. Okudaira, "Low-temperature reactive ion etching

and microwave plasma etching of silicon," *Applied Physics Letters*, vol. 52, no. 8, pp. 616–618, 1988.

[77] R. D'Agostino, "Plasma etching of Si and SiO2 in SF6–O2 mixtures," *Journal of Applied Physics*, vol. 52, no. 1, p. 162, 1981.

[78] S. Tachi, "Low-temperature dry etching," *Journal of Vacuum Science & Technology A: Vacuum, Surfaces, and Films*, vol. 9, no. 3, p. 796, 1991.

[79] M. A. Blauw, T. Zijlstra, R. A. Bakker, and E. van der Drift, "Kinetics and crystal orientation dependence in high aspect ratio silicon dry etching," *Journal of Vacuum Science & Technology B: Microelectronics and Nanometer Structures*, vol. 18, no. 6, p. 3453, 2000.

[80] NA, "Fabrication, photolithography - azonano.com," 2014.

[81] T. Tillocher, R. Dussart, X. Mellhaoui, P. Lefaucheux, N. M. Maaza, P. Ranson, M. Boufnichel, and L. J. Overzet, "Oxidation threshold in silicon etching at cryogenic temperatures," *Journal of Vacuum Science & Technology A: Vacuum, Surfaces, and Films*, vol. 24, no. 4, pp. 1073–1082, 2006.

[82] a. F. Isakovic, K. Evans-Lutterodt, D. Elliott, A. Stein, and J. B. Warren, "Cyclic, cryogenic, highly anisotropic plasma etching of silicon using SF[sub 6]O[sub 2]," *Journal of Vacuum Science & Technology A: Vacuum, Surfaces, and Films*, vol. 26, no. 5, p. 1182, 2008.

[83] M. Boufnichel, S. Aachboun, F. Grangeon, P. Lefaucheux, and P. Ranson, "Profile control of high aspect ratio trenches of silicon. I. Effect of process parameters on local bowing," *Journal of Vacuum Science & Technology B*, vol. 20, no. 4, pp. 1508–1513, 2002.

[84] M. Boufnichel, P. Lefaucheux, S. Aachboun, R. Dussart, and P. Ranson, "Origin, control and elimination of undercut in silicon deep plasma etching in the cryogenic process," *Microelectronic Engineering*, vol. 77, no. 3-4, pp. 327–336, 2005.

[85] G. S. Oehrlein and Y. Kurogi, "Sidewall surface chemistry in directional etching processes," *Materials Science and Engineering: R: Reports*, vol. 24, no. 4, pp. 153–183, 1998.

[86] C. Mogab, "The loading effect in plasma etching," *Journal of the Electrochemical Society*, vol. 124, no. 8, pp. 1262–1268, 1977.

[87] Y. Takata, S. Hidaka, J. Cao, T. Nakamura, H. Yamamoto, M. Masuda, and T. Ito, "Effect of surface wettability on boiling and evaporation," *Energy*, vol. 30, no. 2, pp. 209–220, 2005.

[88] S. G. Kandlikar and M. E. Steinke, "Contact angles and interface behavior during rapid evaporation of liquid on a heated surface," *International Journal of Heat and Mass Transfer*, vol. 45, no. 18, pp. 3771–3780, 2002.

[89] H. Jansen, M. de Boer, H. Wensink, B. Kloeck, and M. Elwenspoek, "The black silicon method. VIII. A study of the performance of etching silicon using SF6/O2-based chemistry with cryogenical wafer cooling and a high density ICP source," *Microelectronics Journal*, vol. 32, no. 9, pp. 769–777, 2001.

[90] R. L. Lane and Z. Li, "Surface roughness studies of deep plasma etching in crystalline silicon," in *University/Government/Industry Microelectronics Symposium, 1995., Proceedings of the Eleventh Biennial*, pp. 134–139, IEEE, 1995.

[91] O. Instruments, "Plasmalab System 100 System Manual," vol. 1, no. 1, 2009.

[92] M. Shao, D. D. D. Ma, and S.-T. Lee, "Silicon nanowires–synthesis, properties, and applications," *European Journal of Inorganic Chemistry*, vol. 2010, no. 27, pp. 4264–4278, 2010.

[93] B. Shi, Y.-B. Wang, and K. Chen, "Pool boiling heat transfer enhancement with copper nanowire arrays," *Applied Thermal Engineering*, vol. 75, pp. 115 – 121, 2015.

[94] M.-C. Lu, R. Chen, V. Srinivasan, V. P. Carey, and A. Majumdar, "Critical heat flux

of pool boiling on si nanowire array-coated surfaces," *International Journal of Heat and Mass Transfer*, vol. 54, no. 25, pp. 5359–5367, 2011.

[95] Z. Yao, Y.-W. Lu, and S. Kandlikar, "Effects of nanowire height on pool boiling performance of water on silicon chips," *International Journal of Thermal Sciences*, vol. 50, no. 11, pp. 2084–2090, 2011.

[96] R. Chen, M.-C. Lu, V. Srinivasan, Z. Wang, H. H. Cho, and A. Majumdar, "Nanowires for enhanced boiling heat transfer," *Nano letters*, vol. 9, no. 2, pp. 548–553, 2009.

[97] H. S. Ahn, N. Sinha, M. Zhang, D. Banerjee, S. Fang, and R. H. Baughman, "Pool boiling experiments on multiwalled carbon nanotube (mwcnt) forests," *Journal of Heat Transfer*, vol. 128, no. 12, pp. 1335–1342, 2006.

[98] S. Ujereh, T. Fisher, and I. Mudawar, "Effects of carbon nanotube arrays on nucleate pool boiling," *International Journal of Heat and Mass Transfer*, vol. 50, no. 19, pp. 4023–4038, 2007.

[99] C.-H. Chen, Q. Cai, C. Tsai, C.-L. Chen, G. Xiong, Y. Yu, and Z. Ren, "Drop-wise condensation on superhydrophobic surfaces with two-tier roughness," *Applied Physics Letters*, vol. 90, no. 17, p. 173108, 2007.

[100] S. H. Kim, H. S. Ahn, J. Kim, M. H. Kim, and H. S. Park, "Experimental study of water droplets on over-heated nano/microstructured zirconium surfaces," *Nuclear Engineering and Design*, vol. 278, pp. 367–376, 2014.

[101] T. Gambaryan-Roisman, "Liquids on porous layers: wetting, imbibition and transport processes," *Current Opinion in Colloid & Interface Science*, vol. 19, no. 4, pp. 320–335, 2014.

[102] C. Liu, J. Ju, J. Ma, Y. Zheng, and L. Jiang, "Directional drop transport achieved on high-temperature anisotropic wetting surfaces," *Advanced Materials*, vol. 26, no. 35, pp. 6086–6091, 2014.

[103] S. H. Kim, H. S. Ahn, J. Kim, M. Kaviany, and M. H. Kim, "Dynamics of water droplet on a heated nanotubes surface," *Applied Physics Letters*, vol. 102, no. 23, p. 233901, 2013.

[104] O. J. Schueller, S. T. Brittain, and G. M. Whitesides, "Fabrication of glassy carbon microstructures by soft lithography," *Sensors and Actuators A: Physical*, vol. 72, no. 2, pp. 125–139, 1999.

[105] C. Wang, G. Jia, L. H. Taherabadi, and M. J. Madou, "A novel method for the fabrication of high-aspect ratio c-mems structures," *Microelectromechanical Systems, Journal of*, vol. 14, no. 2, pp. 348–358, 2005.

[106] M. d. C. Jaramillo, E. Torrents, R. Martínez-Duarte, M. J. Madou, and A. Juárez, "On-line separation of bacterial cells by carbon-electrode dielectrophoresis," *Electrophoresis*, vol. 31, no. 17, pp. 2921–2928, 2010.

[107] R. Kostecki, B. Schnyder, D. Alliata, X. Song, K. Kinoshita, and R. Kötz, "Surface studies of carbon films from pyrolyzed photoresist," *Thin Solid Films*, vol. 396, no. 1, pp. 36–43, 2001.

[108] M. F. De Volder, R. Vansweevelt, P. Wagner, D. Reynaerts, C. Van Hoof, and A. J. Hart, "Hierarchical carbon nanowire microarchitectures made by plasma-assisted pyrolysis of photoresist," *Acs Nano*, vol. 5, no. 8, pp. 6593–6600, 2011.

[109] G. M. Jenkins and K. Kawamura, *Polymeric carbons–carbon fibre, glass and char*. Cambridge University Press, 1976.

[110] J. Kim, X. Song, K. Kinoshita, M. Madou, and R. White, "Electrochemical studies of carbon films from pyrolyzed photoresist," *Journal of the Electrochemical Society*, vol. 145, no. 7, pp. 2314–2319, 1998.

[111] E. Groestad, "Micro engineered surfaces for enhanced heat transfer," 2015.

[112] S. Chandra and S. Aziz, "Leidenfrost evaporation of liquid nitrogen droplets," *Journal of heat transfer*, vol. 116, no. 4, pp. 999–1006, 1994.

A.   Additional Figures
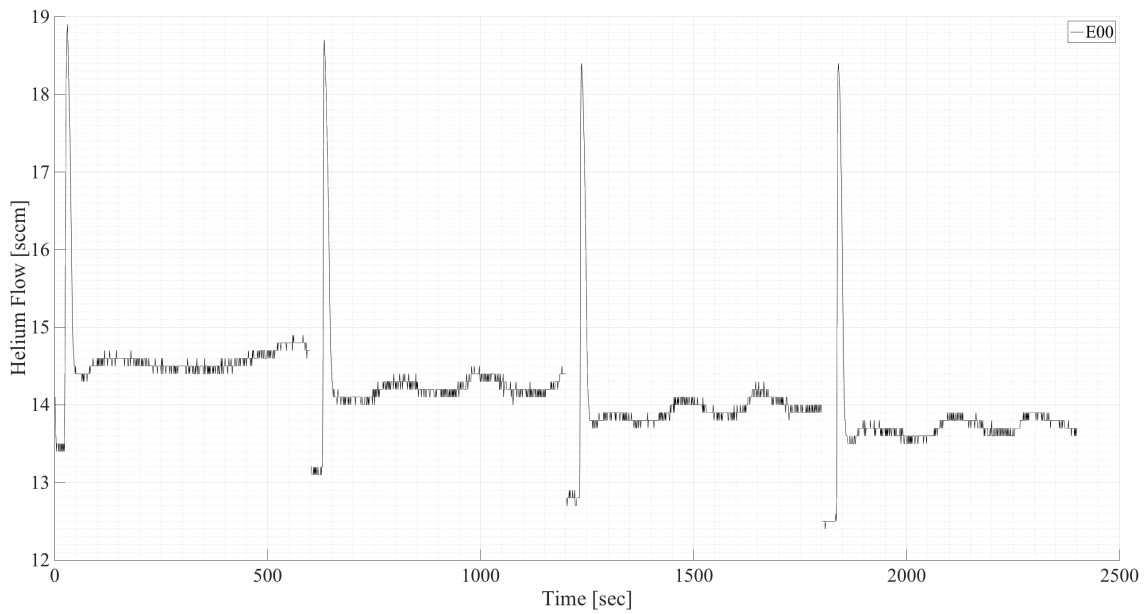
Figure A.1: Flow rate of Helium to backside of wafer E00 as seen in Fig. 4.8. E00 is etched in four 10 min cycles.
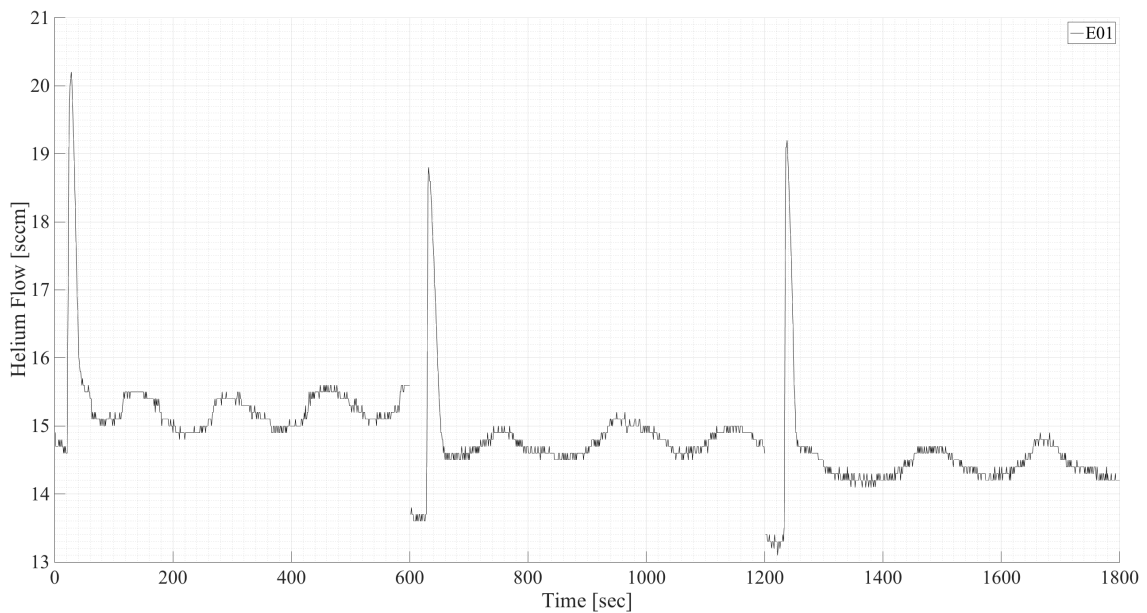
Figure A.2: Flow rate of Helium to backside of wafer E01 as seen in Fig. 4.8. E01 is etched in three 10 min cycles.
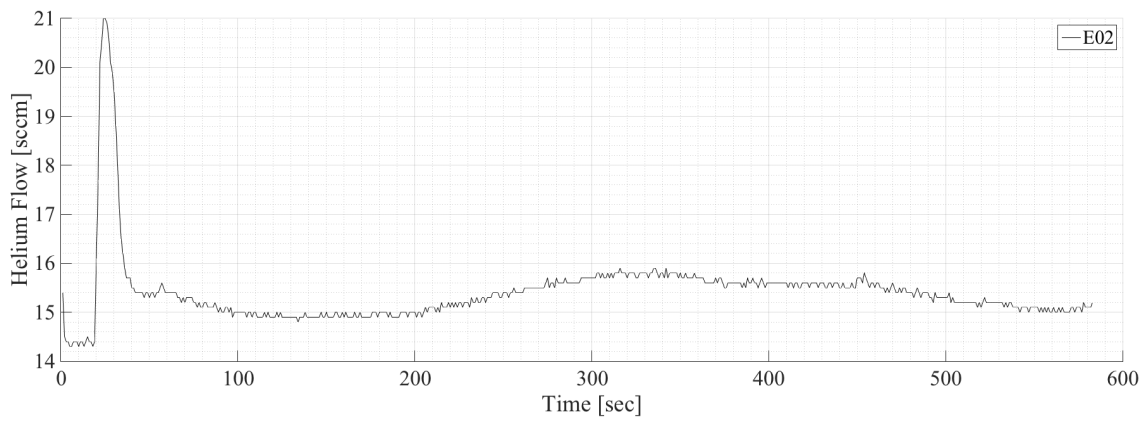
Figure A.3: Flow rate of Helium to backside of wafer E02 as seen in Fig. 4.8.
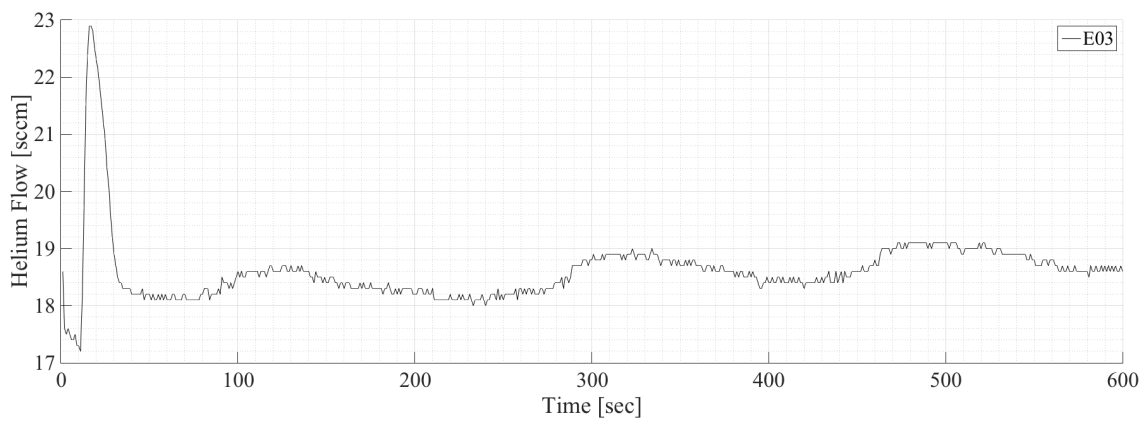
Figure A.4: Flow rate of Helium to backside of wafer E03 as seen in Fig. 4.8. E03 is etched in one 10 min cycle.
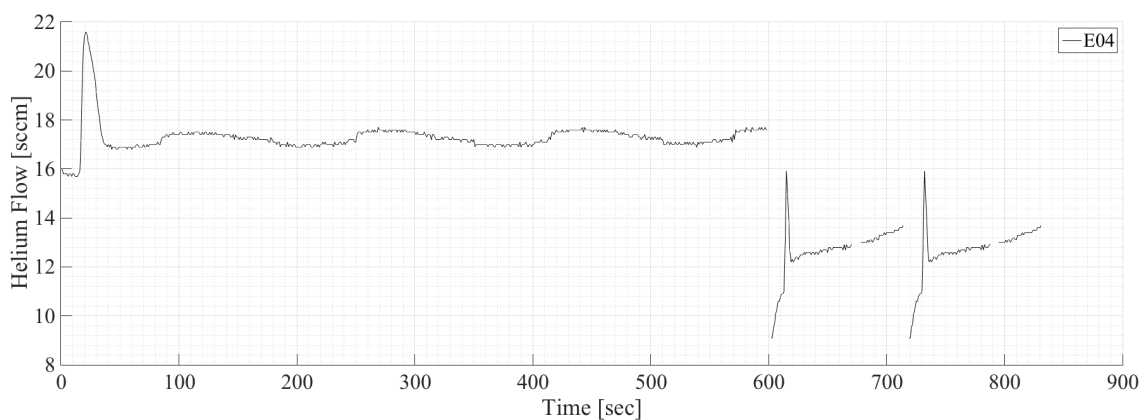
Figure A.5: Flow rate of Helium to backside of wafer E04 as seen in Fig. 4.8. E04 is etched in two 10 min cycles.
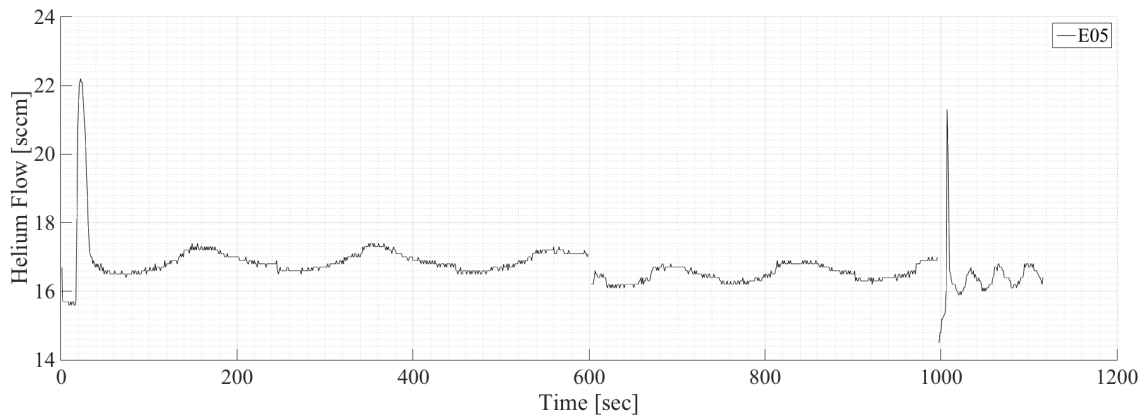
Figure A.6: Flow rate of Helium to backside of wafer E05 as seen in Fig. 4.8. E05 is etched in three 10 min cycles.
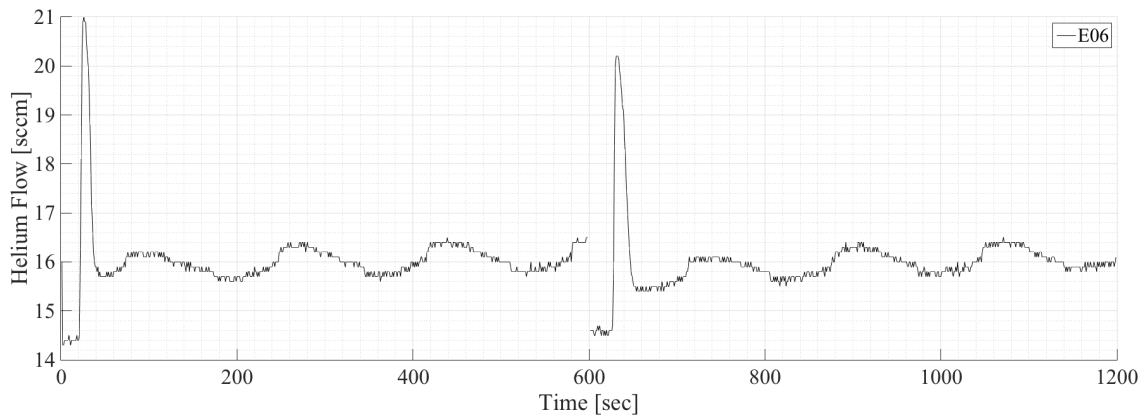
Figure A.7: Flow rate of Helium to backside of wafer E06 as seen in Fig. 4.8. E06 is etched in two 10 min cycles.
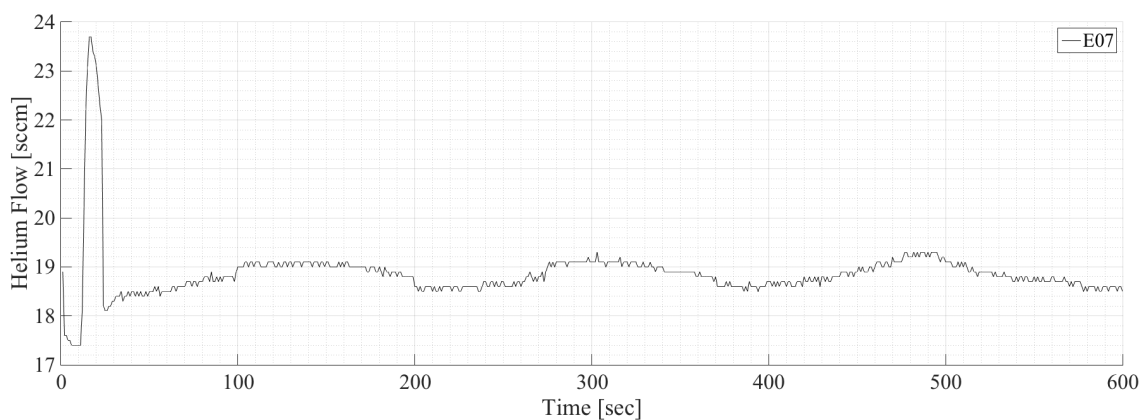
Figure A.8: Flow rate of Helium to backside of wafer E07 as seen in Fig. 4.8. E07 is etched in one 10 min cycle.
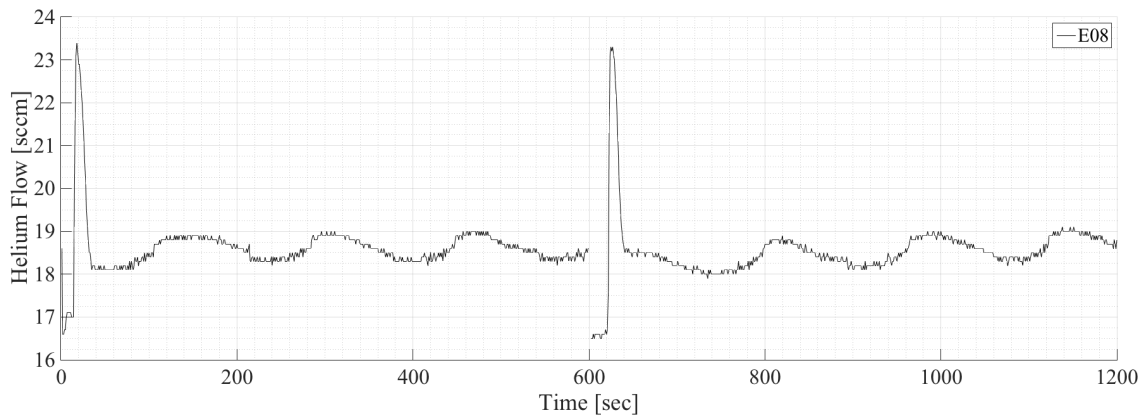
Figure A.9: Flow rate of Helium to backside of wafer E08 as seen in Fig. 4.8. E08 is etched in two 10 min cycles.
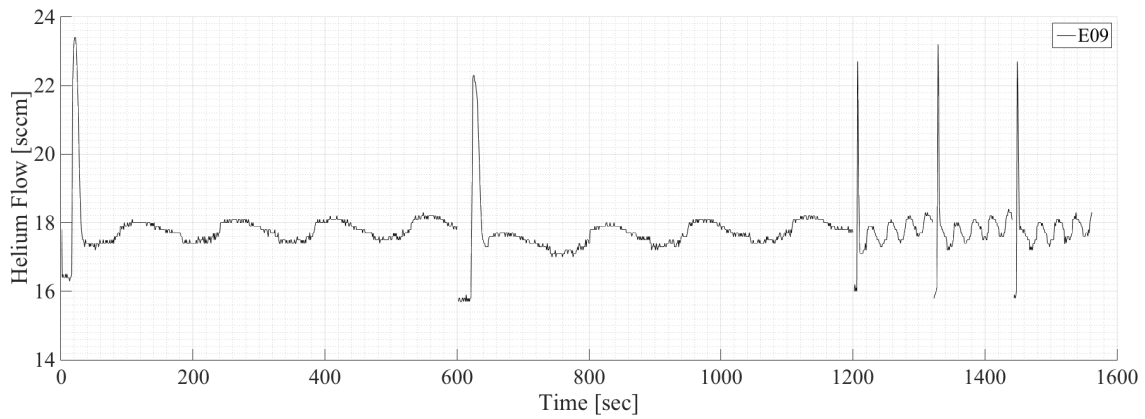
Figure A.10: Flow rate of Helium to backside of wafer E09 as seen in Fig. 4.8. E09 is etched in five 10 min cycles.
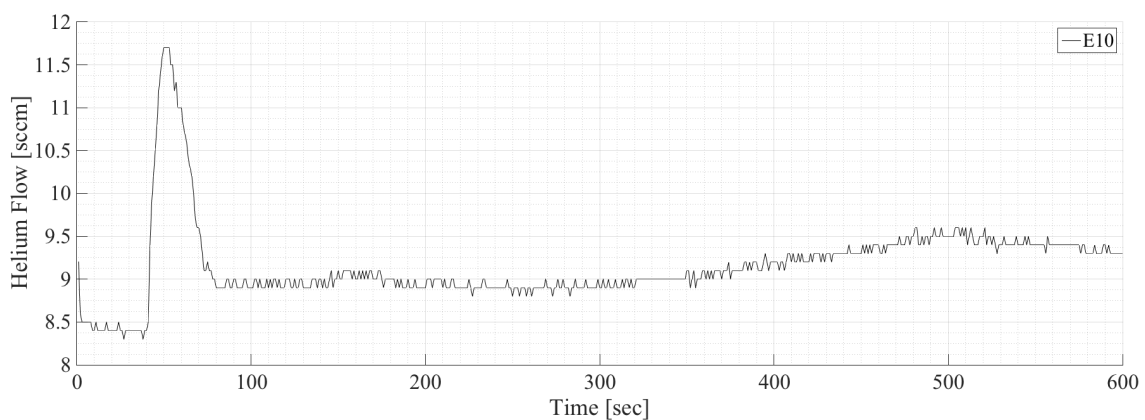
Figure A.11: Flow rate of Helium to backside of wafer E10 as seen in Fig. 4.8. E10 is etched in one 10 min cycle.
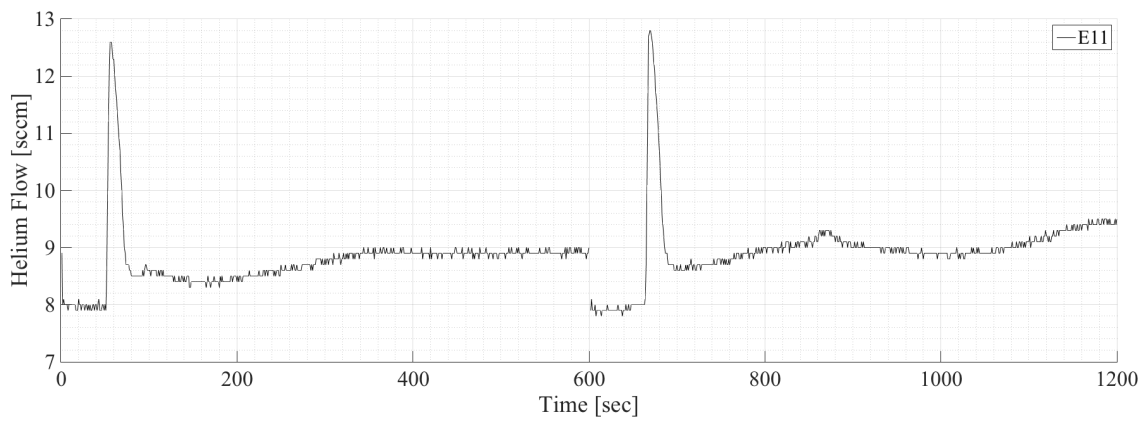
Figure A.12: Flow rate of Helium to backside of wafer E11 as seen in Fig. 4.8. E11 is etched in two 10 min cycles.
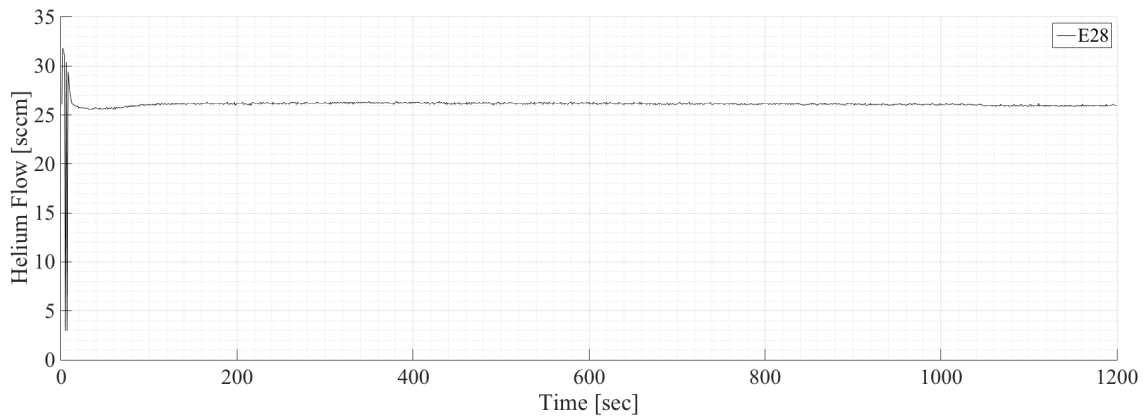
Figure A.13: Flow rate of Helium to backside of wafer E28 as seen in Fig. 4.8.
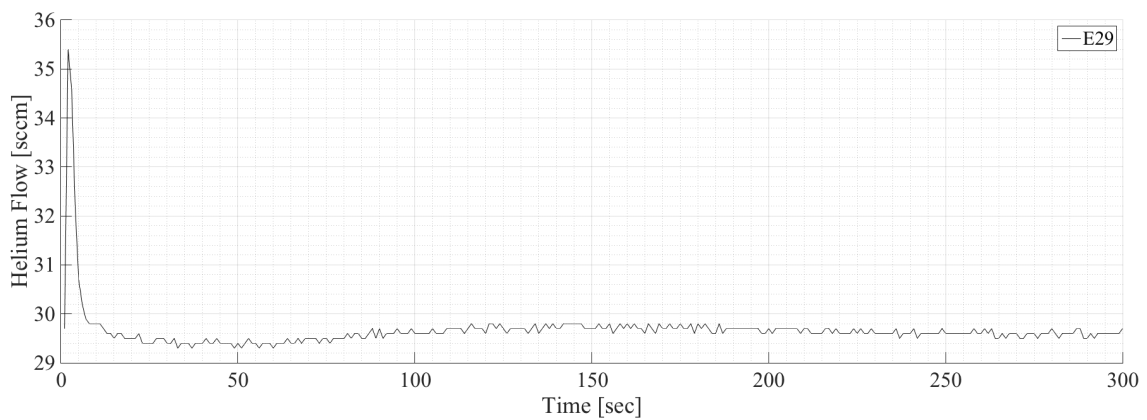
Figure A.14: Flow rate of Helium to backside of wafer E29 as seen in Fig. 4.8.
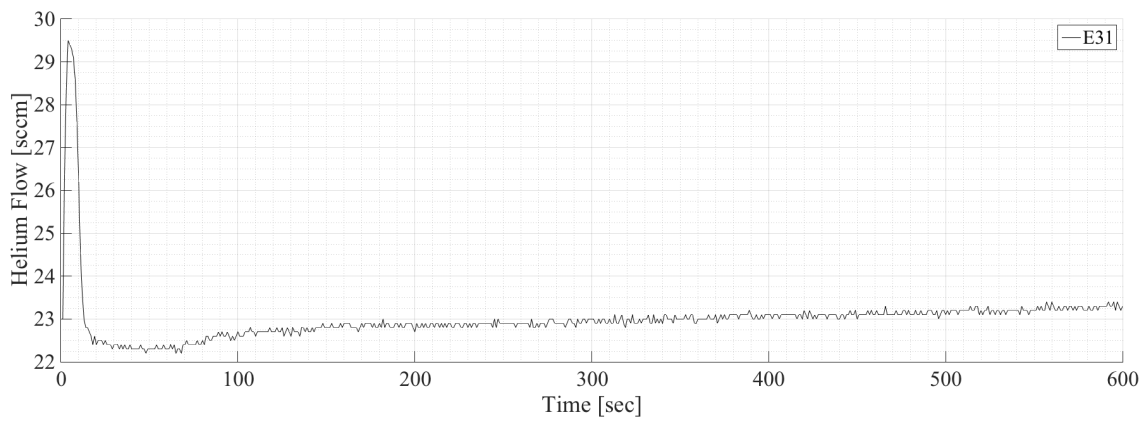
Figure A.15: Flow rate of Helium to backside of wafer E31 as seen in Fig. 4.8.
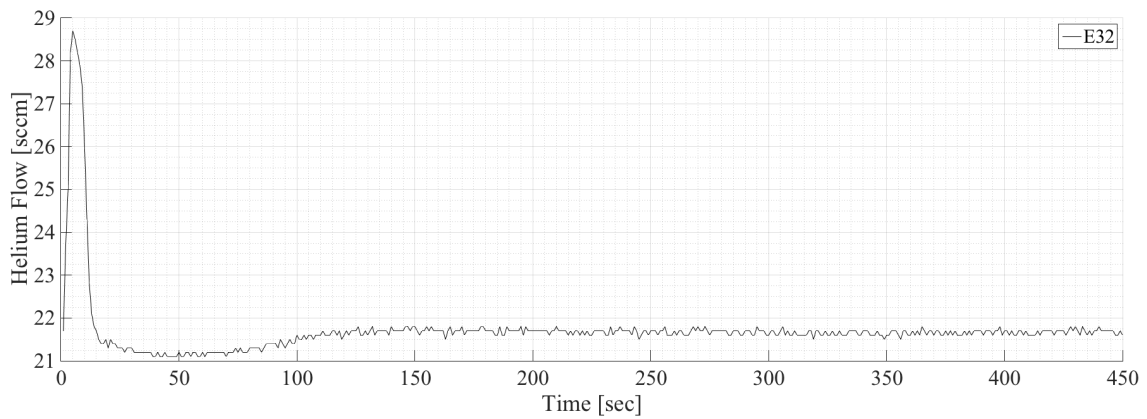
Figure A.16: Flow rate of Helium to backside of wafer E32 as seen in Fig. 4.8.
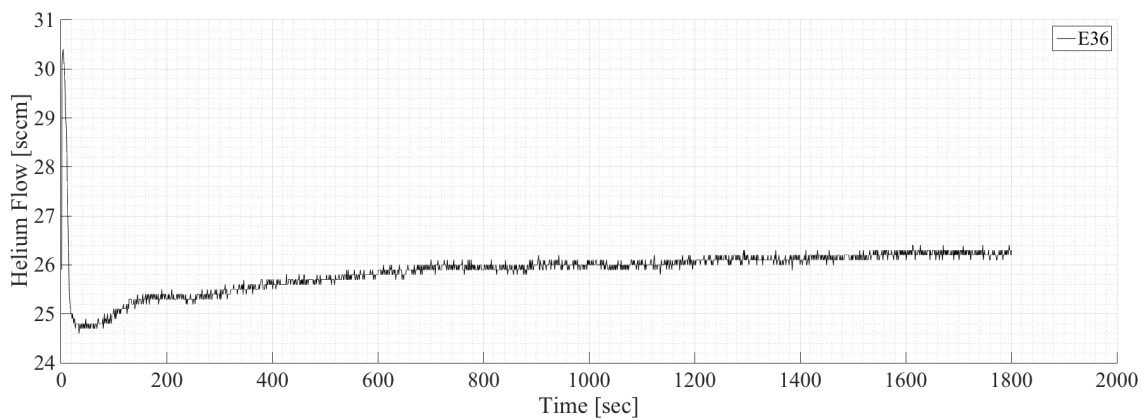
Figure A.17: Flow rate of Helium to backside of wafer E36 as seen in Fig. 4.8.
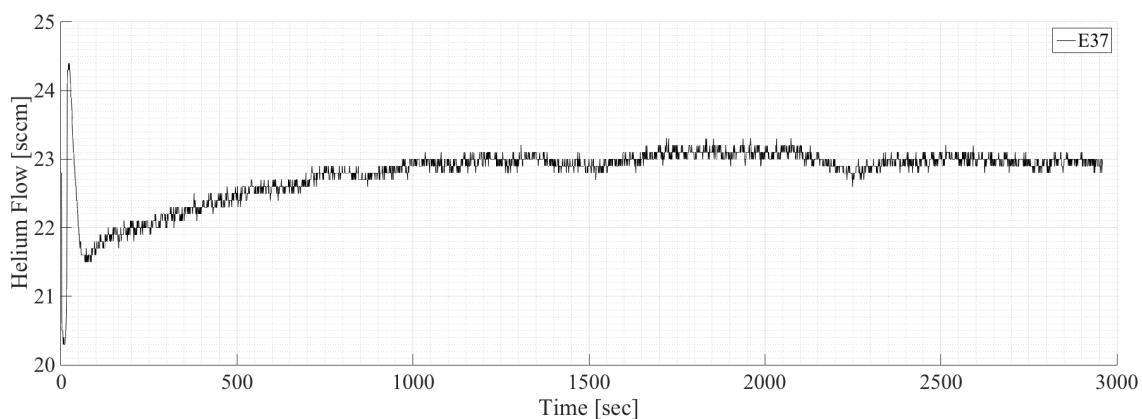
Figure A.18: Flow rate of Helium to backside of wafer E37 as seen in Fig. 4.8.
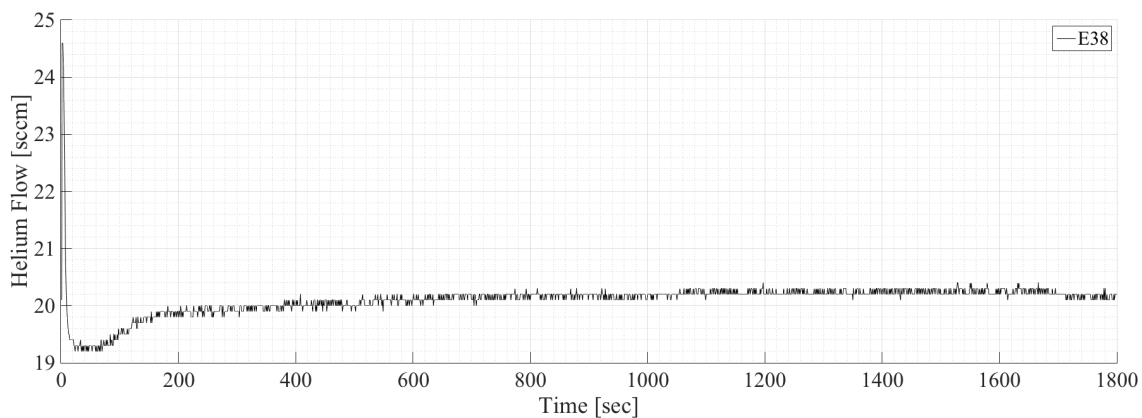
Figure A.19: Flow rate of Helium to backside of wafer E38 as seen in Fig. 4.8.
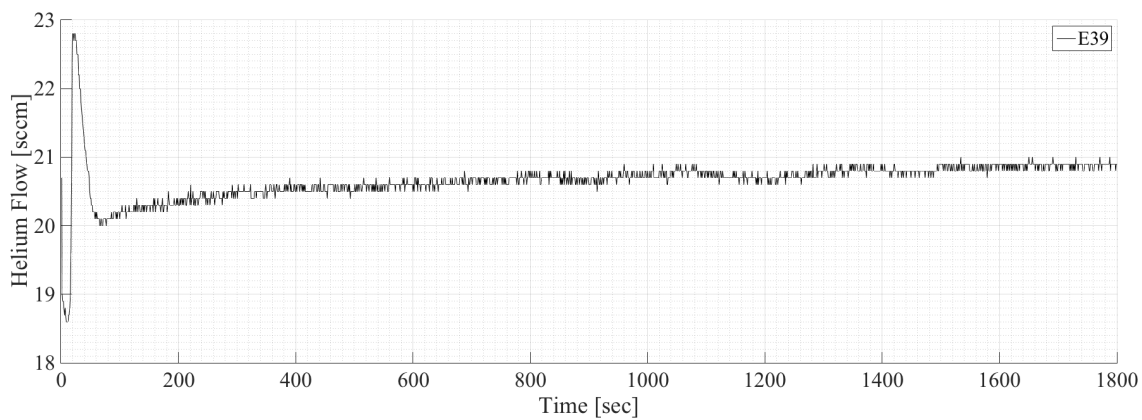
Figure A.20: Flow rate of Helium to backside of wafer E39 as seen in Fig. 4.8.
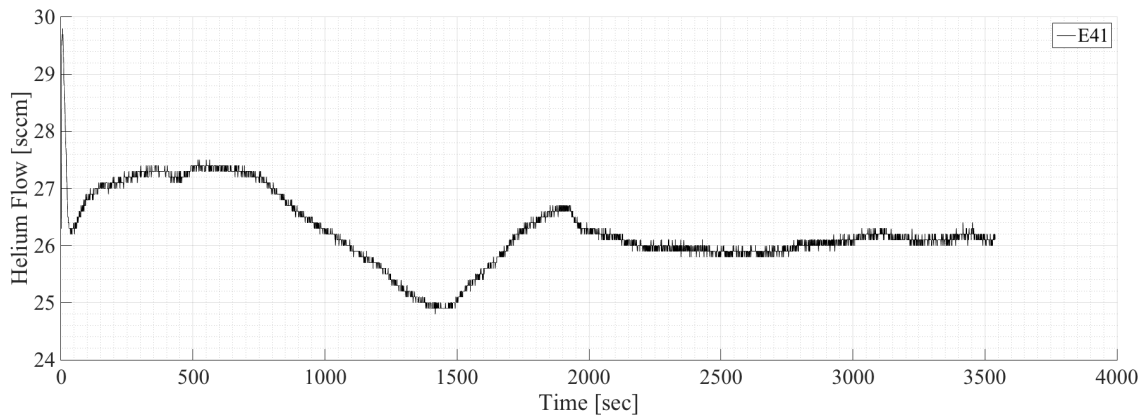
Figure A.21: Flow rate of Helium to backside of wafer E41 as seen in Fig. 4.8.
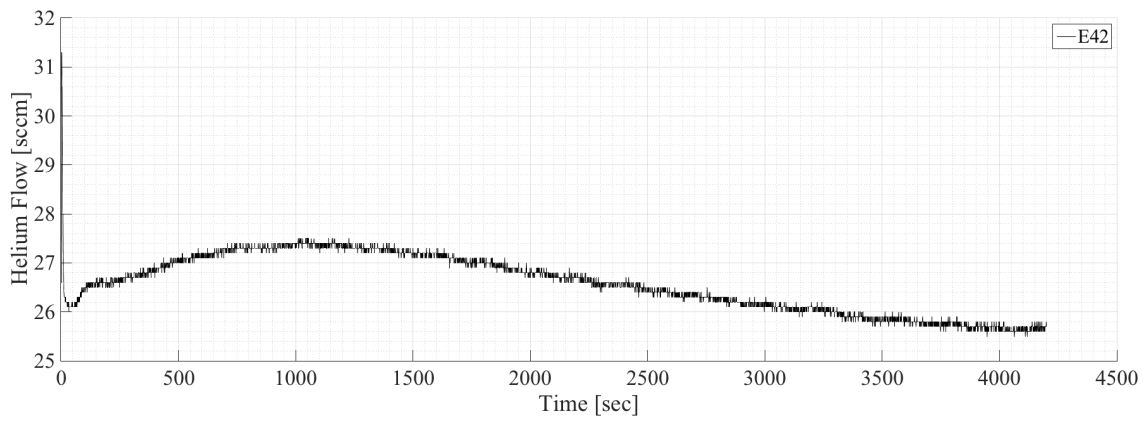
Figure A.22: Flow rate of Helium to backside of wafer E42 as seen in Fig. 4.8.
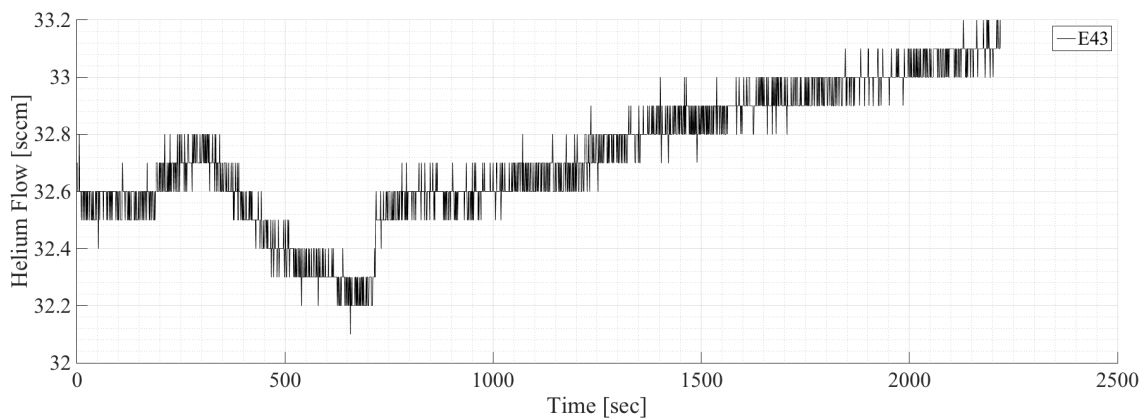
Figure A.23: Flow rate of Helium to backside of wafer E43 as seen in Fig. 4.8.
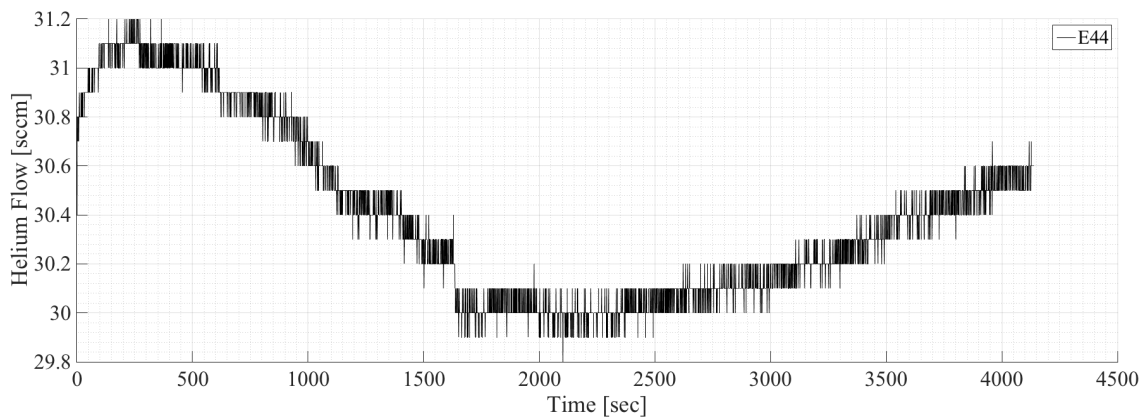
Figure A.24: Flow rate of Helium to backside of wafer E44 as seen in Fig. 4.8.
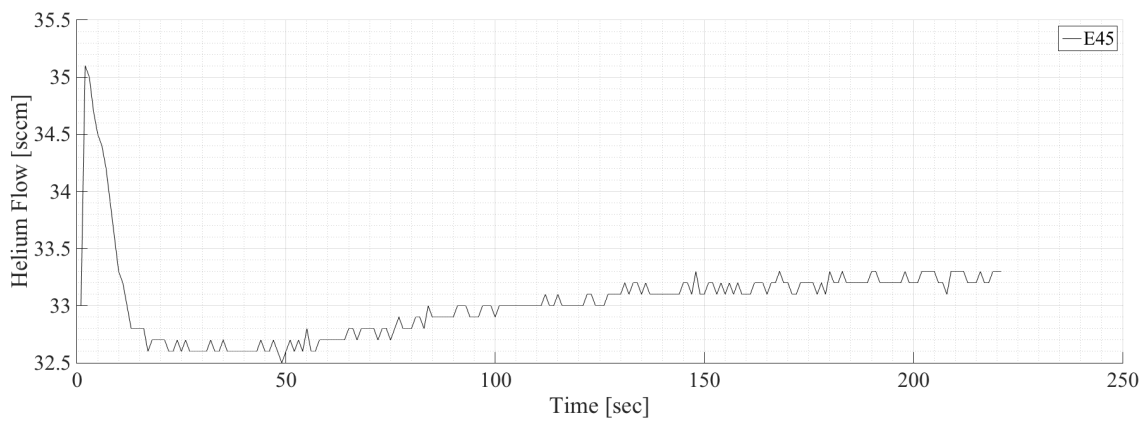
Figure A.25: Flow rate of Helium to backside of wafer E45 as seen in Fig. 4.8.
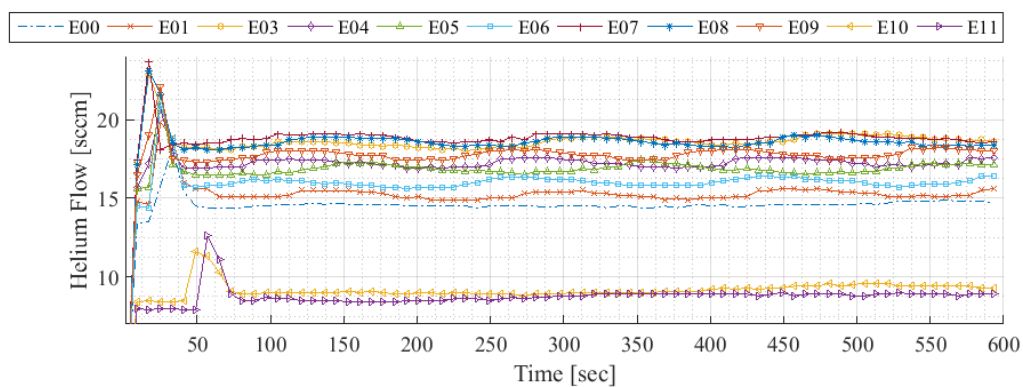
Figure A.26: Flow rate of Helium to backside of wafer as seen in Fig. 4.8. The flow rate is used as a tool to detect leakages from the backside of the wafer to the chamber. A leakage will affect both wafer temperature and chamber gas mixture.
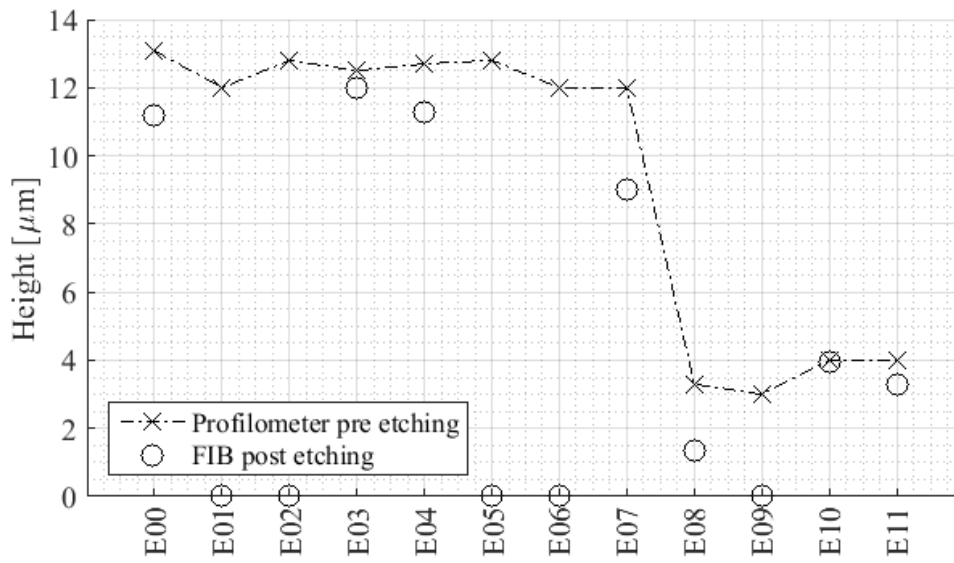
Figure A.27: Mask Thickness measured pre etching. Consistent mask thickness by developed spin-coating recipe can be observed. E01, E02, E05 and E06 have no FIB mask thickness value.
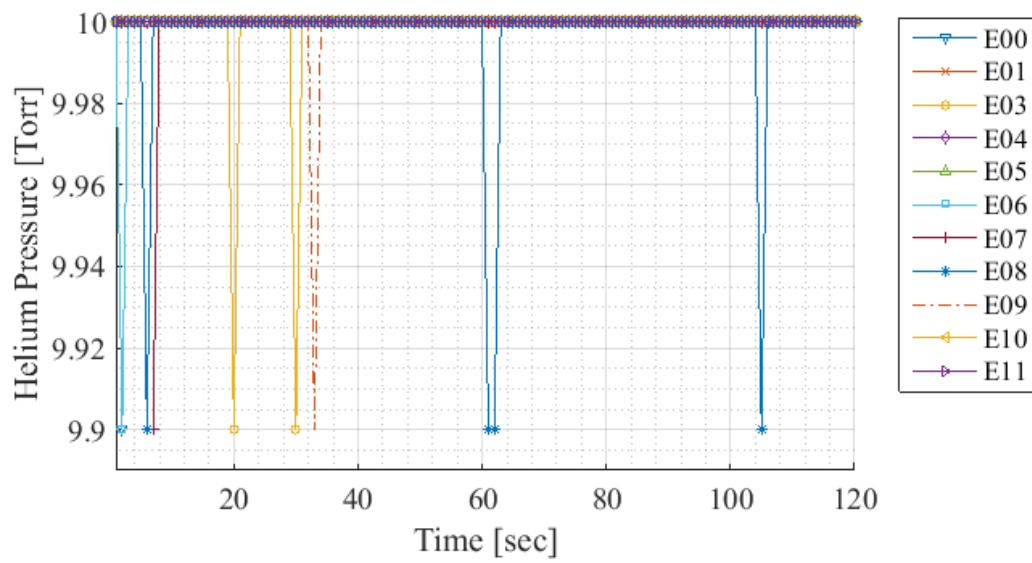
Figure A.28: Helium Pressure. Just the first 120 seconds are plotted due to constant values for all samples after. A constant pressure throughout the etching process can be observed, except some small deviation the first two minutes. Unstable Helium pressure can then not be a reason for variable wafer temperature.
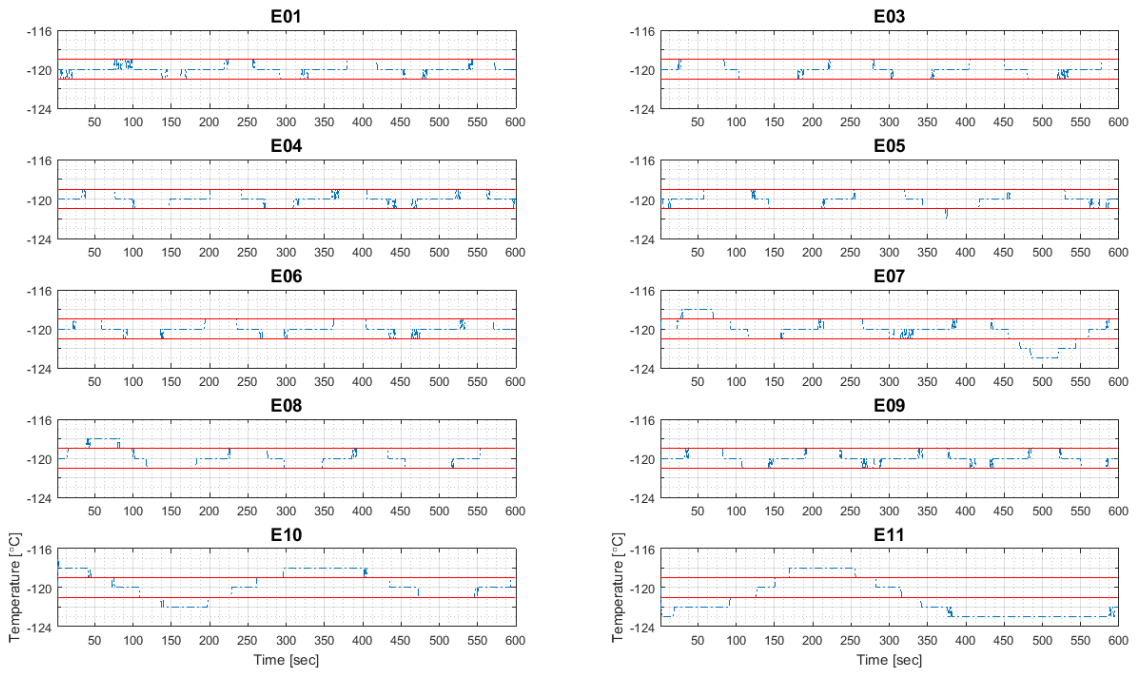
Figure A.29: Table top Temperature. This is not necessary the wafer temperature who is dependent on the Helium leakage, carrier wafer, TIM and contamination of the backside of the wafer. E01 to E09 are varying +/-1°C except E07 who has a dip to -123°C at 500 sec. E10 is in the range -120+/-2°C and E11 is in the range -120+/-3°C. A shift in the wavelength of the cooling cycle can be seen from E09 to E10.
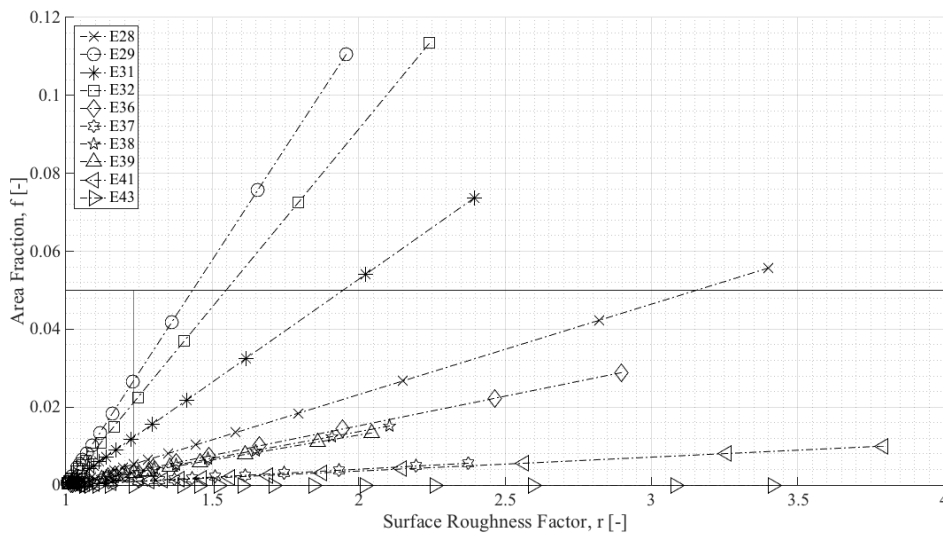
Figure A.30: Results - Cones.
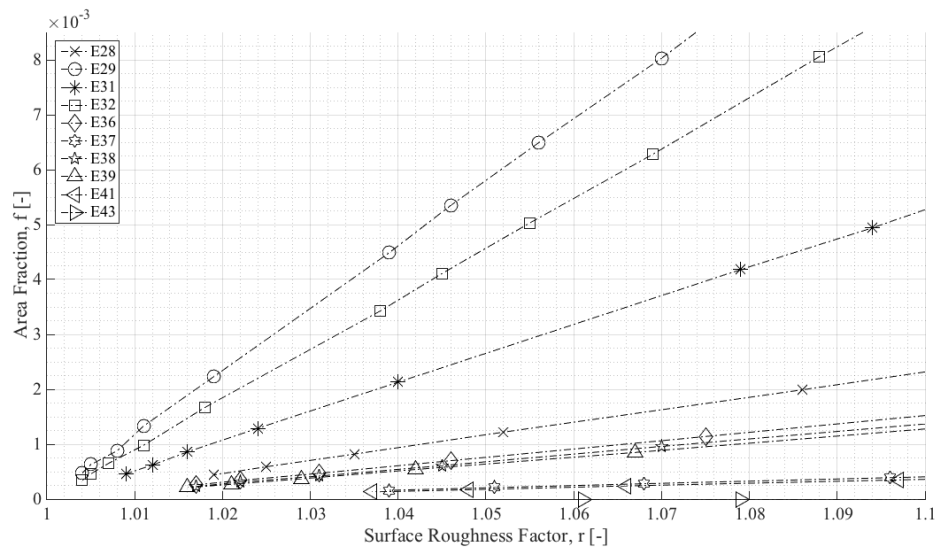
Figure A.31: Results - Cones.

B. Plot Data

B.1 Adera et al (2013)

D: [um] [1]	Px: [um]	Py: [um]	H: [um]	S:	Ap:	At:	Aa:	f:	r:	H/D:	P/D:	Intrinsic CA:	Wenzel:	Cassie:
6.6	13.4	13.4	18.3	1.00	400.00	34.21	779.44	0.08553	1.949	2.77	2.03	59.9	12.24603719	150.6423002
4.6	15.4	15.4	15.2	1.00	400.00	16.62	619.66	0.04155	1.549	3.30	3.35	59.9	39.02097218	159.6549548
9.1	10.9	10.9	15.8	1.00	400.00	65.04	851.70	0.16260	2.129	1.74	1.20	59.9	#NUM!	139.1004644
3.8	8.2	8.2	27.4	1.00	144.00	11.34	471.10	0.07876	3.272	7.21	2.16	59.9	#NUM!	151.8534673
3.1	6.9	6.9	15	1.00	100.00	7.55	246.08	0.07548	2.461	4.84	2.23	59.9	#NUM!	152.4578406
6.6	23.4	23.4	17	1.00	900.00	34.21	1252.49	0.03801	1.392	2.58	3.55	59.9	45.73896838	160.5483193

Figure B.1: Adera et al (2013) data values. D = Diameter. $P_x = P_y$ = Pitch. H = Height. A_p calculated with Equation 2.1. A_t calculated with Equation 2.2. A_a calculated with Equation 2.3. f calculated with Equation 2.13. r calculated with Equation 2.14.

B.2 Duursma et al (2014)

D: [um]	Px: [um]	Py: [um]	H: [um]	S:	Ap:	At:	Aa:	f:	r:	H/D:	P/D:	Intrinsic CA:	Wenzel:	Cassie:
5	5	5	10	1.00	100.00	25.00	300.00	0.250000	3.0000	2.00	1.00	59.9	#NUM!	128.6544718
5	10	10	10	1.00	225.00	25.00	425.00	0.111111	1.8889	2.00	2.00	59.9	18.68430651	146.4252952
5	20	20	10	1.00	625.00	25.00	825.00	0.040000	1.3200	2.00	4.00	59.9	48.54786233	160.0414105
10	40	40	10	1.00	2500.00	100.00	2900.00	0.040000	1.1600	1.00	4.00	59.9	54.42610438	160.0414105
10	10	10	10	1.00	400.00	100.00	800.00	0.250000	2.0000	1.00	1.00	59.9	#NUM!	128.6544718
10	20	20	10	1.00	900.00	100.00	1300.00	0.111111	1.4444	1.00	2.00	59.9	43.58067669	146.4252952
10	30	30	10	1.00	1600.00	100.00	2000.00	0.062500	1.2500	1.00	3.00	59.9	51.17907281	154.9793726
10	40	40	10	1.00	2500.00	100.00	2900.00	0.040000	1.1600	1.00	4.00	59.9	54.42610438	160.0414105
10	50	50	10	1.00	3600.00	100.00	4000.00	0.027778	1.1111	1.00	5.00	59.9	56.13526406	163.3937427
10	60	60	10	1.00	4900.00	100.00	5300.00	0.020408	1.0816	1.00	6.00	59.9	57.14939624	165.7793612
10	70	70	10	1.00	6400.00	100.00	6800.00	0.015625	1.0625	1.00	7.00	59.9	57.80142988	167.5644607
10	80	80	10	1.00	8100.00	100.00	8500.00	0.012346	1.0494	1.00	8.00	59.9	58.24577014	168.9507572
10	90	90	10	1.00	10000.00	100.00	10400.00	0.010000	1.0400	1.00	9.00	59.9	58.56229862	170.0586179
10	100	100	10	1.00	12100.00	100.00	12500.00	0.008264	1.0331	1.00	10.00	59.9	58.79580703	170.9643522

Figure B.2: Duursma et al (2014) data values. D = Diameter. $P_x = P_y$ = Pitch. H = Height. A_p calculated with Equation 2.4. A_t calculated with Equation 2.5. A_a calculated with Equation 2.6. f calculated with Equation 2.13. r calculated with Equation 2.14.

B.3 Feng et al (2011)

D: [um]	Px: [um]	Py: [um]	H: [um]	S:	Ap:	At:	Aa:	f:	r:	H/D:	P/D:	Intrinsic CA:	Wenzel:	Cassie:
2.5	2.5	2.5	5	1.00	25.00	6.25	75.00	0.25000	3.000	2.00	1.00	59.9	#NUM!	128.6544718
2.5	3.09	3.09	5	1.00	31.25	6.25	81.25	0.20001	2.600	2.00	1.24	59.9	#NUM!	134.4013034
2.5	4	4	5	1.00	42.25	6.25	92.25	0.14793	2.183	2.00	1.60	59.9	#NUM!	141.0671539
2.5	5.4	5.4	5	1.00	62.41	6.25	112.41	0.10014	1.801	2.00	2.16	59.9	25.40499431	148.1717093
2.5	8.7	8.7	5	1.00	125.44	6.25	175.44	0.04982	1.399	2.00	3.48	59.9	45.45965068	157.696691
5	5	5	5	1.00	100.00	25.00	200.00	0.25000	2.000	1.00	1.00	59.9	#NUM!	128.6544718
5	6.2	6.2	5	1.00	125.44	25.00	225.44	0.19930	1.797	1.00	1.24	59.9	25.66893323	134.4873047
5	7.9	7.9	5	1.00	166.41	25.00	266.41	0.15023	1.601	1.00	1.58	59.9	36.5938671	140.7530212
5	10.8	10.8	5	1.00	249.64	25.00	349.64	0.10014	1.401	1.00	2.16	59.9	45.37977746	148.1717093
5	17.4	17.4	5	1.00	501.76	25.00	601.76	0.04982	1.199	1.00	3.48	59.9	53.02538986	157.696691
10	10	10	5	1.00	400.00	100.00	600.00	0.25000	1.500	0.50	1.00	59.9	41.2129419	128.6544718
10	12.4	12.4	5	1.00	501.76	100.00	701.76	0.19930	1.399	0.50	1.24	59.9	45.45965068	134.4873047
10	15.84	15.84	5	1.00	667.71	100.00	867.71	0.14977	1.300	0.50	1.58	59.9	49.32784701	140.8162614
10	21.6	21.6	5	1.00	998.56	100.00	1198.56	0.10014	1.200	0.50	2.16	59.9	52.98977572	148.1717093
10	34.7	34.7	5	1.00	1998.09	100.00	2198.09	0.05005	1.100	0.50	3.47	59.9	56.51561173	157.6661535
50	50	50	5	1.00	10000.00	2500.00	11000.00	0.25000	1.100	0.10	1.00	59.9	56.518905	128.6544718

Figure B.3: Feng et al (2011) data values. D = Diameter. $P_x = P_y$ = Pitch. H = Height. A_p calculated with Equation 2.4. A_t calculated with Equation 2.5. A_a calculated with Equation 2.6. f calculated with Equation 2.13. r calculated with Equation 2.14.

B.4   He et al (2014)

D: [um]	Px: [um]	Py: [um]	H: [um]	S:	Ap:	At:	Aa:	f:	r:	H/D:	P/D:	Theta_C:	Intrinsic CA:	Wenzel:	Cassie:
10	20	40	20	2.00	1500.00	100.00	2300.00	0.06667	1.533	2.00	2.00	129.52	59.9	39.73733754	154.1448317
10	20	60	20	3.00	2100.00	100.00	2900.00	0.04762	1.381	2.00	2.00	135.58	59.9	46.16670743	158.2021079
10	20	80	20	4.00	2700.00	100.00	3500.00	0.03704	1.296	2.00	2.00	139.88	59.9	49.45036716	160.8021119
10	20	100	20	5.00	3300.00	100.00	4100.00	0.03030	1.242	2.00	2.00	143.13	59.9	51.45793066	162.6497593
20	40	80	20	2.00	6000.00	400.00	7600.00	0.06667	1.267	1.00	2.00	141.06	59.9	50.56169851	154.1448317
20	40	120	20	3.00	8400.00	400.00	10000.00	0.04762	1.190	1.00	2.00	146.44	59.9	53.34204731	158.2021079
20	40	160	20	4.00	10800.00	400.00	12400.00	0.03704	1.148	1.00	2.00	150.07	59.9	54.84371967	160.8021119
10	20	40	40	2.00	1500.00	100.00	3100.00	0.06667	2.067	4.00	2.00	117.82	59.9	#NUM!	154.1448317
10	20	60	40	3.00	2100.00	100.00	3700.00	0.04762	1.762	4.00	2.00	123.75	59.9	27.91854162	158.2021079
10	20	80	40	4.00	2700.00	100.00	4300.00	0.03704	1.593	4.00	2.00	128.25	59.9	36.99364221	160.8021119
10	20	100	40	5.00	3300.00	100.00	4900.00	0.03030	1.485	4.00	2.00	131.81	59.9	41.86945594	162.6497593
20	40	80	40	2.00	6000.00	400.00	9200.00	0.06667	1.533	2.00	2.00	129.52	59.9	39.73733754	154.1448317
20	40	120	40	3.00	8400.00	400.00	11600.00	0.04762	1.381	2.00	2.00	135.58	59.9	46.16670743	158.2021079
20	40	160	40	4.00	10800.00	400.00	14000.00	0.03704	1.296	2.00	2.00	139.88	59.9	49.45036716	160.8021119

Figure B.4: He et al (2014) data values. D = Diameter. P_x = P_y = Pitch. H = Height. A_p calculated with Equation 2.4. A_t calculated with Equation 2.5. A_a calculated with Equation 2.6. f calculated with Equation 2.13. r calculated with Equation 2.14.

B.5   Kim et al (2012)

D: [um]	Px: [um]	Py: [um]	H: [um]	S:	Ap:	At:	Aa:	f:	r:	h/D:	P/D:	Intrinsic CA:	Wenzel:	Cassie:
5	500	500	0	1.00	255025.00	19.63	255025.00	0.00008	1.0000000	0.00	100.00	59.9	59.9	179.1287765
5	500	500	5	1.00	255025.00	19.63	255103.54	0.00008	1.0003080	1.00	100.00	59.9	59.88977083	179.1287765
5	500	500	10	1.00	255025.00	19.63	255182.08	0.00008	1.0006159	2.00	100.00	59.9	59.8795406	179.1287765
5	500	500	15	1.00	255025.00	19.63	255260.62	0.00008	1.0009239	3.00	100.00	59.9	59.86930932	179.1287765

Figure B.5: Kim et al (2012) data values. D = Diameter. P_x = P_y = Pitch. H = Height. A_p calculated with Equation 2.1. A_t calculated with Equation 2.2. A_a calculated with Equation 2.3. f calculated with Equation 2.13. r calculated with Equation 2.14.

B.6   Kwon et al (2013)

D: [um]	Px: [um]	Py: [um]	H: [um]	S:	Ap:	At:	Aa:	f:	r:	H/D:	P/D:	Intrinsic CA:	Wenzel:	Cassie:
10	75	75	10	1.00	7225.00	100.00	7625.00	0.013841	1.05536	1.00	7.50	59.9	58.04344736	168.2985969
10	100	100	10	1.00	12100.00	100.00	12500.00	0.008264	1.03306	1.00	10.00	59.9	58.79580703	170.9643522
10	80	80	10	1.00	8100.00	100.00	8500.00	0.012346	1.04938	1.00	8.00	59.9	58.24577014	168.9507572
10	50	50	10	1.00	3600.00	100.00	4000.00	0.027778	1.11111	1.00	5.00	59.9	56.13526406	163.3937427
10	40	40	10	1.00	2500.00	100.00	2900.00	0.040000	1.16000	1.00	4.00	59.9	54.42610438	160.0414105
10	30	30	10	1.00	1600.00	100.00	2000.00	0.062500	1.25000	1.00	3.00	59.9	51.17907281	154.9793726
10	25	25	10	1.00	1225.00	100.00	1625.00	0.081633	1.32653	1.00	2.50	59.9	48.29700786	151.3336077
10	10	10	10	1.00	400.00	100.00	800.00	0.250000	2.00000	1.00	1.00	59.9	#NUM!	128.6544718
10	5	5	10	1.00	225.00	100.00	625.00	0.444444	2.77778	1.00	0.50	59.9	#NUM!	109.4304215
10	3.3	3.3	10	1.00	176.89	100.00	576.89	0.565323	3.26129	1.00	0.33	59.9	#NUM!	98.69423287

Figure B.6: Kwon et al (2013) data values. D = Diameter. P_x = P_y = Pitch. H = Height. A_p calculated with Equation 2.4. A_t calculated with Equation 2.5. A_a calculated with Equation 2.6. f calculated with Equation 2.13. r calculated with Equation 2.14.

B.7 Tran et al (2013)

D: [um]	Px: [um]	Py: [um]	H: [um]	S:	Ap:	At:	Aa:	f:	r:	h/D:	P/D:	Intrinsic CA:	Wenzel:	Cassie:
9	4	4	2	1.00	169.00	63.62	225.55	0.37643	1.335	0.22	0.44	59.9	47.98539687	115.7713689
9	4	4	4	1.00	169.00	63.62	282.10	0.37643	1.669	0.44	0.44	59.9	33.16179474	115.7713689
9	4	4	8	1.00	169.00	63.62	395.19	0.37643	2.338	0.89	0.44	59.9	#NUM!	115.7713689
9	20	20	2	1.00	841.00	63.62	897.55	0.07564	1.067	0.22	2.22	59.9	57.64033887	152.4265992
9	20	20	4	1.00	841.00	63.62	954.10	0.07564	1.134	0.44	2.22	59.9	55.32270404	152.4265992
9	20	20	8	1.00	841.00	63.62	1067.19	0.07564	1.269	0.89	2.22	59.9	50.47635116	152.4265992

Figure B.7: Tran et al (2013) data values. D = Diameter. $P_x = P_y$ = Pitch. H = Height. A_p calculated with Equation 2.1. A_t calculated with Equation 2.2. A_a calculated with Equation 2.3. f calculated with Equation 2.13. r calculated with Equation 2.14.

B.8 Yoshimitsu et al (2002)

D: [um]	Px: [um]	Py: [um]	H: [um]	S:	Ap:	At:	Aa:	f:	r:	H/D:	P/D:	Intrinsic CA:	Wenzel:	Cassie:
50	100	100	0	1.00	22500.00	2500.00	22500.00	0.11111	1.000	0.00	2.00	114	114	159.080314
50	100	100	10	1.00	22500.00	2500.00	24500.00	0.11111	1.089	0.20	2.00	114	116.288485	159.080314
50	100	100	36	1.00	22500.00	2500.00	29700.00	0.11111	1.320	0.72	2.00	114	122.4723384	159.080314
50	100	100	148	1.00	22500.00	2500.00	52100.00	0.11111	2.316	2.96	2.00	114	160.3597033	159.080314
50	100	100	282	1.00	22500.00	2500.00	78900.00	0.11111	3.507	5.64	2.00	114	#NUM!	159.080314
50	100	100	35	1.00	22500.00	2500.00	29500.00	0.11111	1.311	0.70	2.00	114	122.2271325	159.080314

Figure B.8: Yoshimitsu et al (2002) data values. D = Diameter. $P_x = P_y$ = Pitch. H = Height. A_p calculated with Equation 2.4. A_t calculated with Equation 2.5. A_a calculated with Equation 2.6. f calculated with Equation 2.13. r calculated with Equation 2.14.

B.9   Cones fabricated by author

DL: [um]	DU: [um]	Px: [um]	Py: [um]	H: [um]	Ap:	At:	Aa:	f:	r:
28,8	9	5	5	55,2	1142,44	63,62	3884,47	0,05569	3,400
28,8	9	10	10	55,2	1505,44	63,62	4247,47	0,04226	2,821
28,8	9	20	20	55,2	2381,44	63,62	5123,47	0,02671	2,151
28,8	9	30	30	55,2	3457,44	63,62	6199,47	0,01840	1,793
28,8	9	40	40	55,2	4733,44	63,62	7475,47	0,01344	1,579
28,8	9	50	50	55,2	6209,44	63,62	8951,47	0,01025	1,442
28,8	9	60	60	55,2	7885,44	63,62	10627,47	0,00807	1,348
28,8	9	70	70	55,2	9761,44	63,62	12503,47	0,00652	1,281
28,8	9	80	80	55,2	11837,44	63,62	14579,47	0,00537	1,232
28,8	9	90	90	55,2	14113,44	63,62	16855,47	0,00451	1,194
28,8	9	100	100	55,2	16589,44	63,62	19331,47	0,00383	1,165
28,8	9	150	150	55,2	31969,44	63,62	34711,47	0,00199	1,086
28,8	9	200	200	55,2	52349,44	63,62	55091,47	0,00122	1,052
28,8	9	250	250	55,2	77729,44	63,62	80471,47	0,00082	1,035
28,8	9	300	300	55,2	108109,44	63,62	110851,47	0,00059	1,025
28,8	9	350	350	55,2	143489,44	63,62	146231,47	0,00044	1,019

Figure B.9: Surface Calculations - E28. D_L = Lower Diameter. D_U = Upper Diameter. $P_x = P_y$ = Pitch. H = Height. A_p calculated with Equation 2.10. A_t calculated with Equation 2.11. A_a calculated with Equation 2.12. f calculated with Equation 2.13. r calculated with Equation 2.14.

DL: [um]	DU: [um]	Px: [um]	Py: [um]	H: [um]	Ap:	At:	Aa:	f:	r:
19	9	5	5	16,8	576,00	63,62	1127,02	0,11045	1,957
19	9	10	10	16,8	841,00	63,62	1392,02	0,07564	1,655
19	9	20	20	16,8	1521,00	63,62	2072,02	0,04183	1,362
19	9	30	30	16,8	2401,00	63,62	2952,02	0,02650	1,229
19	9	40	40	16,8	3481,00	63,62	4032,02	0,01828	1,158
19	9	50	50	16,8	4761,00	63,62	5312,02	0,01336	1,116
19	9	60	60	16,8	6241,00	63,62	6792,02	0,01019	1,088
19	9	70	70	16,8	7921,00	63,62	8472,02	0,00803	1,070
19	9	80	80	16,8	9801,00	63,62	10352,02	0,00649	1,056
19	9	90	90	16,8	11881,00	63,62	12432,02	0,00535	1,046
19	9	100	100	16,8	14161,00	63,62	14712,02	0,00449	1,039
19	9	150	150	16,8	28561,00	63,62	29112,02	0,00223	1,019
19	9	200	200	16,8	47961,00	63,62	48512,02	0,00133	1,011
19	9	250	250	16,8	72361,00	63,62	72912,02	0,00088	1,008
19	9	300	300	16,8	101761,00	63,62	102312,02	0,00063	1,005
19	9	350	350	16,8	136161,00	63,62	136712,02	0,00047	1,004

Figure B.10: Surface Calculations - E29. D_L = Lower Diameter. D_U = Upper Diameter. $P_x = P_y$ = Pitch. H = Height. A_p calculated with Equation 2.10. A_t calculated with Equation 2.11. A_a calculated with Equation 2.12. f calculated with Equation 2.13. r calculated with Equation 2.14.

DL: [um]	DU: [um]	Px: [um]	Py: [um]	H: [um]	Ap:	At:	Aa:	f:	r:
24,7	9,1	5	5	30	882,09	65,04	2113,71	0,07373	2,396
24,7	9,1	10	10	30	1204,09	65,04	2435,71	0,05401	2,023
24,7	9,1	20	20	30	1998,09	65,04	3229,71	0,03255	1,616
24,7	9,1	30	30	30	2992,09	65,04	4223,71	0,02174	1,412
24,7	9,1	40	40	30	4186,09	65,04	5417,71	0,01554	1,294
24,7	9,1	50	50	30	5580,09	65,04	6811,71	0,01166	1,221
24,7	9,1	60	60	30	7174,09	65,04	8405,71	0,00907	1,172
24,7	9,1	70	70	30	8968,09	65,04	10199,71	0,00725	1,137
24,7	9,1	80	80	30	10962,09	65,04	12193,71	0,00593	1,112
24,7	9,1	90	90	30	13156,09	65,04	14387,71	0,00494	1,094
24,7	9,1	100	100	30	15550,09	65,04	16781,71	0,00418	1,079
24,7	9,1	150	150	30	30520,09	65,04	31751,71	0,00213	1,040
24,7	9,1	200	200	30	50490,09	65,04	51721,71	0,00129	1,024
24,7	9,1	250	250	30	75460,09	65,04	76691,71	0,00086	1,016
24,7	9,1	300	300	30	105430,09	65,04	106661,71	0,00062	1,012
24,7	9,1	350	350	30	140400,09	65,04	141631,71	0,00046	1,009

Figure B.11: Surface Calculations - E31. D_L = Lower Diameter. D_U = Upper Diameter. $P_x = P_y$ = Pitch. H = Height. A_p calculated with Equation 2.10. A_t calculated with Equation 2.11. A_a calculated with Equation 2.12. f calculated with Equation 2.13. r calculated with Equation 2.14.

DL: [um]	DU: [um]	Px: [um]	Py: [um]	H: [um]	Ap:	At:	Aa:	f:	r:
15	7,6	5	5	17,3	400,00	45,36	896,69	0,11341	2,242
15	7,6	10	10	17,3	625,00	45,36	1121,69	0,07258	1,795
15	7,6	20	20	17,3	1225,00	45,36	1721,69	0,03703	1,405
15	7,6	30	30	17,3	2025,00	45,36	2521,69	0,02240	1,245
15	7,6	40	40	17,3	3025,00	45,36	3521,69	0,01500	1,164
15	7,6	50	50	17,3	4225,00	45,36	4721,69	0,01074	1,118
15	7,6	60	60	17,3	5625,00	45,36	6121,69	0,00806	1,088
15	7,6	70	70	17,3	7225,00	45,36	7721,69	0,00628	1,069
15	7,6	80	80	17,3	9025,00	45,36	9521,69	0,00503	1,055
15	7,6	90	90	17,3	11025,00	45,36	11521,69	0,00411	1,045
15	7,6	100	100	17,3	13225,00	45,36	13721,69	0,00343	1,038
15	7,6	150	150	17,3	27225,00	45,36	27721,69	0,00167	1,018
15	7,6	200	200	17,3	46225,00	45,36	46721,69	0,00098	1,011
15	7,6	250	250	17,3	70225,00	45,36	70721,69	0,00065	1,007
15	7,6	300	300	17,3	99225,00	45,36	99721,69	0,00046	1,005
15	7,6	350	350	17,3	133225,00	45,36	133721,69	0,00034	1,004

Figure B.12: Surface Calculations - E32. D_L = Lower Diameter. D_U = Upper Diameter. $P_x = P_y$ = Pitch. H = Height. A_p calculated with Equation 2.10. A_t calculated with Equation 2.11. A_a calculated with Equation 2.12. f calculated with Equation 2.13. r calculated with Equation 2.14.

DL: [um]	DU: [um]	Px: [um]	Py: [um]	H: [um]	Ap:	At:	Aa:	f:	r:
31	6,9	5	5	52	1296,00	37,39	3756,38	0,02885	2,898
31	6,9	10	10	52	1681,00	37,39	4141,38	0,02224	2,464
31	6,9	20	20	52	2601,00	37,39	5061,38	0,01438	1,946
31	6,9	30	30	52	3721,00	37,39	6181,38	0,01005	1,661
31	6,9	40	40	52	5041,00	37,39	7501,38	0,00742	1,488
31	6,9	50	50	52	6561,00	37,39	9021,38	0,00570	1,375
31	6,9	60	60	52	8281,00	37,39	10741,38	0,00452	1,297
31	6,9	70	70	52	10201,00	37,39	12661,38	0,00367	1,241
31	6,9	80	80	52	12321,00	37,39	14781,38	0,00303	1,200
31	6,9	90	90	52	14641,00	37,39	17101,38	0,00255	1,168
31	6,9	100	100	52	17161,00	37,39	19621,38	0,00218	1,143
31	6,9	150	150	52	32761,00	37,39	35221,38	0,00114	1,075
31	6,9	200	200	52	53361,00	37,39	55821,38	0,00070	1,046
31	6,9	250	250	52	78961,00	37,39	81421,38	0,00047	1,031
31	6,9	300	300	52	109561,00	37,39	112021,38	0,00034	1,022
31	6,9	350	350	52	145161,00	37,39	147621,38	0,00026	1,017

Figure B.13: Surface Calculations - E36. D_L = Lower Diameter. D_U = Upper Diameter. $P_x = P_y$ = Pitch. H = Height. A_p calculated with Equation 2.10. A_t calculated with Equation 2.11. A_a calculated with Equation 2.12. f calculated with Equation 2.13. r calculated with Equation 2.14.

DL: [um]	DU: [um]	Px: [um]	Py: [um]	H: [um]	Ap:	At:	Aa:	f:	r:
65	5,9	5	5	85	4900,00	27,34	11631,17	0,00558	2,374
65	5,9	10	10	85	5625,00	27,34	12356,17	0,00486	2,197
65	5,9	20	20	85	7225,00	27,34	13956,17	0,00378	1,932
65	5,9	30	30	85	9025,00	27,34	15756,17	0,00303	1,746
65	5,9	40	40	85	11025,00	27,34	17756,17	0,00248	1,611
65	5,9	50	50	85	13225,00	27,34	19956,17	0,00207	1,509
65	5,9	60	60	85	15625,00	27,34	22356,17	0,00175	1,431
65	5,9	70	70	85	18225,00	27,34	24956,17	0,00150	1,369
65	5,9	80	80	85	21025,00	27,34	27756,17	0,00130	1,320
65	5,9	90	90	85	24025,00	27,34	30756,17	0,00114	1,280
65	5,9	100	100	85	27225,00	27,34	33956,17	0,00100	1,247
65	5,9	150	150	85	46225,00	27,34	52956,17	0,00059	1,146
65	5,9	200	200	85	70225,00	27,34	76956,17	0,00039	1,096
65	5,9	250	250	85	99225,00	27,34	105956,17	0,00028	1,068
65	5,9	300	300	85	133225,00	27,34	139956,17	0,00021	1,051
65	5,9	350	350	85	172225,00	27,34	178956,17	0,00016	1,039

Figure B.14: Surface Calculations - E37. D_L = Lower Diameter. D_U = Upper Diameter. $P_x = P_y$ = Pitch. H = Height. A_p calculated with Equation 2.10. A_t calculated with Equation 2.11. A_a calculated with Equation 2.12. f calculated with Equation 2.13. r calculated with Equation 2.14.

DL: [um]	DU: [um]	Px: [um]	Py: [um]	H: [um]	Ap:	At:	Aa:	f:	r:
44	6,8	5	5	48,4	2401,00	36,32	5054,31	0,01513	2,105
44	6,8	10	10	48,4	2916,00	36,32	5569,31	0,01245	1,910
44	6,8	20	20	48,4	4096,00	36,32	6749,31	0,00887	1,648
44	6,8	30	30	48,4	5476,00	36,32	8129,31	0,00663	1,485
44	6,8	40	40	48,4	7056,00	36,32	9709,31	0,00515	1,376
44	6,8	50	50	48,4	8836,00	36,32	11489,31	0,00411	1,300
44	6,8	60	60	48,4	10816,00	36,32	13469,31	0,00336	1,245
44	6,8	70	70	48,4	12996,00	36,32	15649,31	0,00279	1,204
44	6,8	80	80	48,4	15376,00	36,32	18029,31	0,00236	1,173
44	6,8	90	90	48,4	17956,00	36,32	20609,31	0,00202	1,148
44	6,8	100	100	48,4	20736,00	36,32	23389,31	0,00175	1,128
44	6,8	150	150	48,4	37636,00	36,32	40289,31	0,00096	1,070
44	6,8	200	200	48,4	59536,00	36,32	62189,31	0,00061	1,045
44	6,8	250	250	48,4	86436,00	36,32	89089,31	0,00042	1,031
44	6,8	300	300	48,4	118336,00	36,32	120989,31	0,00031	1,022
44	6,8	350	350	48,4	155236,00	36,32	157889,31	0,00023	1,017

Figure B.15: Surface Calculations - E38. D_L = Lower Diameter. D_U = Upper Diameter. $P_x = P_y$ = Pitch. H = Height. A_p calculated with Equation 2.10. A_t calculated with Equation 2.11. A_a calculated with Equation 2.12. f calculated with Equation 2.13. r calculated with Equation 2.14.

DL: [um]	DU: [um]	Px: [um]	Py: [um]	H: [um]	Ap:	At:	Aa:	f:	r:
44	6,4	5	5	46,9	2401,00	32,17	4912,82	0,01340	2,046
44	6,4	10	10	46,9	2916,00	32,17	5427,82	0,01103	1,861
44	6,4	20	20	46,9	4096,00	32,17	6607,82	0,00785	1,613
44	6,4	30	30	46,9	5476,00	32,17	7987,82	0,00587	1,459
44	6,4	40	40	46,9	7056,00	32,17	9567,82	0,00456	1,356
44	6,4	50	50	46,9	8836,00	32,17	11347,82	0,00364	1,284
44	6,4	60	60	46,9	10816,00	32,17	13327,82	0,00297	1,232
44	6,4	70	70	46,9	12996,00	32,17	15507,82	0,00248	1,193
44	6,4	80	80	46,9	15376,00	32,17	17887,82	0,00209	1,163
44	6,4	90	90	46,9	17956,00	32,17	20467,82	0,00179	1,140
44	6,4	100	100	46,9	20736,00	32,17	23247,82	0,00155	1,121
44	6,4	150	150	46,9	37636,00	32,17	40147,82	0,00085	1,067
44	6,4	200	200	46,9	59536,00	32,17	62047,82	0,00054	1,042
44	6,4	250	250	46,9	86436,00	32,17	88947,82	0,00037	1,029
44	6,4	300	300	46,9	118336,00	32,17	120847,82	0,00027	1,021
44	6,4	350	350	46,9	155236,00	32,17	157747,82	0,00021	1,016

Figure B.16: Surface Calculations - E39. D_L = Lower Diameter. D_U = Upper Diameter. $P_x = P_y$ = Pitch. H = Height. A_p calculated with Equation 2.10. A_t calculated with Equation 2.11. A_a calculated with Equation 2.12. f calculated with Equation 2.13. r calculated with Equation 2.14.

DL: [um]	DU: [um]	Px: [um]	Py: [um]	H: [um]	Ap:	At:	Aa:	f:	r:
39,6	5,03	5	5	95	1989,16	19,87	7546,68	0,00999	3,794
39,6	5,03	10	10	95	2460,16	19,87	8017,68	0,00808	3,259
39,6	5,03	20	20	95	3552,16	19,87	9109,68	0,00559	2,565
39,6	5,03	30	30	95	4844,16	19,87	10401,68	0,00410	2,147
39,6	5,03	40	40	95	6336,16	19,87	11893,68	0,00314	1,877
39,6	5,03	50	50	95	8028,16	19,87	13585,68	0,00248	1,692
39,6	5,03	60	60	95	9920,16	19,87	15477,68	0,00200	1,560
39,6	5,03	70	70	95	12012,16	19,87	17569,68	0,00165	1,463
39,6	5,03	80	80	95	14304,16	19,87	19861,68	0,00139	1,389
39,6	5,03	90	90	95	16796,16	19,87	22353,68	0,00118	1,331
39,6	5,03	100	100	95	19488,16	19,87	25045,68	0,00102	1,285
39,6	5,03	150	150	95	35948,16	19,87	41505,68	0,00055	1,155
39,6	5,03	200	200	95	57408,16	19,87	62965,68	0,00035	1,097
39,6	5,03	250	250	95	83868,16	19,87	89425,68	0,00024	1,066
39,6	5,03	300	300	95	115328,16	19,87	120885,68	0,00017	1,048
39,6	5,03	350	350	95	151788,16	19,87	157345,68	0,00013	1,037

Figure B.17: Surface Calculations - E41. D_L = Lower Diameter. D_U = Upper Diameter. $P_x = P_y$ = Pitch. H = Height. A_p calculated with Equation 2.10. A_t calculated with Equation 2.11. A_a calculated with Equation 2.12. f calculated with Equation 2.13. r calculated with Equation 2.14.

DL: [um]	DU: [um]	Px: [um]	Py: [um]	H: [um]	Ap:	At:	Aa:	f:	r:
60	0	5	5	135	4225,00	0,00	14431,39	0,00000	3,416
60	0	10	10	135	4900,00	0,00	15106,39	0,00000	3,083
60	0	20	20	135	6400,00	0,00	16606,39	0,00000	2,595
60	0	30	30	135	8100,00	0,00	18306,39	0,00000	2,260
60	0	40	40	135	10000,00	0,00	20206,39	0,00000	2,021
60	0	50	50	135	12100,00	0,00	22306,39	0,00000	1,844
60	0	60	60	135	14400,00	0,00	24606,39	0,00000	1,709
60	0	70	70	135	16900,00	0,00	27106,39	0,00000	1,604
60	0	80	80	135	19600,00	0,00	29806,39	0,00000	1,521
60	0	90	90	135	22500,00	0,00	32706,39	0,00000	1,454
60	0	100	100	135	25600,00	0,00	35806,39	0,00000	1,399
60	0	150	150	135	44100,00	0,00	54306,39	0,00000	1,231
60	0	200	200	135	67600,00	0,00	77806,39	0,00000	1,151
60	0	250	250	135	96100,00	0,00	106306,39	0,00000	1,106
60	0	300	300	135	129600,00	0,00	139806,39	0,00000	1,079
60	0	350	350	135	168100,00	0,00	178306,39	0,00000	1,061

Figure B.18: Surface Calculations - E43. D_L = Lower Diameter. D_U = Upper Diameter. $P_x = P_y$ = Pitch. H = Height. A_p calculated with Equation 2.10. A_t calculated with Equation 2.11. A_a calculated with Equation 2.12. f calculated with Equation 2.13. r calculated with Equation 2.14.

C. Recipes

C.1 PILLAR RECIPE A

1. Cleaning of Si wafer

   - Acetone, Isopropanol, Ethanol, Water, N_2

   - Plasma cleaner 3 min

2. Photoresist, spin coat

   - ma-N440

   - 1000 rpm - 3sec - 1000 rpm/sec

   - 3000 rpm - 30sec - 1000 rpm/sec

3. Baking

   - Type: Soft baking

   - Temp: 95°C

   - Time: 5 min

4. UV exposure

   - Type: MA6

   - Energy: 1300 mJ/cm^2

5. Development

   - Type: ma-D332 S

   - Time: 90 - 120 sec

6. Cleaning

   - Type: Plasma cleaner

   - Time: 30 sec

7. Sputtering

- Type: AJA

- Metall: Al

- Time: 10 - 30 min

- Power: 300 W

8. Lift off

   - Acetone in sonic bath

   - Time: 20 min

9. Etching

   - Type: ICP-RIE Cryo

   - Time: 5 - 20 min

   - Gas: $SF_6 and O_2$

C.2 PILLAR RECIPE B

1. Cleaning of Si wafer

   - Acetone, Isopropanol, Ethanol, Water, N_2

   - Plasma cleaner 3 min ($50\%O_2, 50\%power$)

2. Photoresist, spin coat

   - SU-8 5

   - 1000 rpm - 33sec - 300 rpm/sec

3. Pre Exposure Baking

   - Type: Soft baking

   - Temp: 65°C

   - Time: 1 min

   - Increase temp to 95°C with wafer on plate

   - Temp: 95°C

   - Time: 4 min

   - Cool down: 3 min

4. UV exposure

   - Type: MA6

   - Energy: 200 mJ

   - Method: Hard

   - Distance: 100

5. Post Exposure Baking

   - Type: Soft baking

   - Temp: 65°C

- Time: 1 min

- Increase temp to 95 degrees with wafer on plate

- Temp: 95°C

- Time: 2 min

- Cool down: 3 min

6. Development

    - Type: Dev-630

    - Time: 1 min development, water bath, N2, repeat 3 times

7. Etching

    - Type: ICP-RIE Cryo

    - Time: 5 - 20 min

    - Gas: SF_6 and O_2

C.3   PILLAR RECIPE C

1. Cleaning of Si wafer

   - Acetone, Isopropanol, Ethanol, Water, N_2

   - Plasma cleaner 3 min ($50\%O_2, 50\%power$)

2. Dehydration

   - 200°C for 5 min

3. Photoresist, spin coat

   - SU8-5

   - 1000 rpm - 33sec - 300 rpm/sec

4. Pre Exposure Baking

   - Type: Soft baking

   - Temp: 65°C

   - Time: 1 min

   - Increase temp to 95°C with wafer on plate

   - Temp: 95°C

   - Time: 4 min

   - Cool down: 3 min

5. UV exposure

   - Type: MA6

   - Energy: 200 mJ

   - Method: Hard

   - Distance: 100

6. Post Exposure Baking

- Type: Soft baking

- Temp: 65°C

- Time: 1 min

- Increase temp to 95°C with wafer on plate

- Temp: 95°C

- Time: 2 min

- Cool down: 3 min

7. Development

- Type: Dev-630

- Time: 1 min development, water bath, N2, repeat 3 times

8. Etching

- Type: ICP-RIE Cryo

- Time: 5 - 20 min

- Gas: SF_6 and O_2

C.4 PILLAR RECIPE D

1. Cleaning of Si wafer

   - Acetone bath in beaker, gently stirring in circles

   - Lift up the wafer while showering with Ethanol

   - Continue showering with Isopropanol

   - Continue showering with DI water

   - Dry with N_2

2. Dehydration

   - 200°C for 5 min

3. Plasma cleaner 3 min ($50\%O_2, 50\%power$)

4. Photoresist, spin coat

   - SU8-5

   - 1000 rpm - 33sec - 300 rpm/sec

   - This gives a photoresist thickness of ~12-15 μ m

5. Pre Exposure Baking

   - Use your own clean 4" carrier wafer on the plate

   - Type: Soft baking

   - Temp: 65°C

   - Time: 1 min

   - Increase temp to 95°C with wafer on plate

   - Temp: 95°C

   - Time: 4 min

   - Cool down: 3 min on plate

6. UV exposure

  - Type: MA6

  - Energy: 200 mJ

  - Method: Hard

  - Distance: 100 (This is only for alignment)

7. Post Exposure Baking

  - Use your own clean 4" carrier wafer on the plate

  - Type: Soft baking

  - Temp: 65°C

  - Time: 1 min

  - Increase temp to 95°C with wafer on plate

  - Temp: 95°C

  - Time: 2 min

  - Cool down: 3 min on plate

8. Development

  - Type: Dev-630

  - Time: 1 min development, Isopropanol bath, water bath, N2, repeat 3 times

9. Etching

  - Type: ICP-RIE Cryo

  - Time: 5 - 20 min

  - Gas: SF_6 and O_2

  - If the wafer gets black you produce nanowires. Reduce O_2 if you don't want that

C.5 PILLAR RECIPE E

1. Cleaning of Si wafer

    - Acetone bath in beaker, gently stirring in circles

    - Lift up the wafer while showering with Ethanol

    - Continue showering with Isopropanol

    - Continue showering with DI water

    - Dry with N_2

2. Dehydration

    - 200°C for 5 min

3. Plasma cleaner 3 min ($50\%O_2, 50\%power$)

4. Photoresist, spin coat

    - SU8-5

    - 1000 rpm - 33sec - 300 rpm/sec

    - This gives a photoresist thickness of ~$12 - 15\mu m$

5. Pre Exposure Baking

    - Use your own clean 4" carrier wafer on the plate

    - Type: Soft baking

    - Temp: 65°C

    - Time: 1 min

    - Increase temp to 95°C with wafer on plate

    - Temp: 95°C

    - Time: 4 min

    - Cool down: 3 min on plate

6. UV exposure

   - Type: MA6

   - Energy: 200 mJ

   - Method: Hard

   - Distance: 100 (This is only for alignment)

7. Post Exposure Baking

   - Use your own clean 4" carrier wafer on the plate

   - Type: Soft baking

   - Temp: 65°C

   - Time: 1 min

   - Increase temp to 95°C with wafer on plate

   - Temp: 95°C

   - Time: 2 min

   - Cool down: 3 min on plate

8. Development

   - Type: Dev-600

   - Time: 1 min development, water bath, N2, repeat 3 times

   - Isopropanol bath

   - N2

9. Profilometer: check height of photoresist pillar

10. Dehydration

    - 200°C for 5 min

11. Etching

    - Type: ICP-RIE Cryo

- Time: 5 - 20 min

- Gas: SF_6 and O_2

- If the wafer gets black you produce nanowires. Reduce O_2 if you dont want that

C.6   PILLAR RECIPE F

1. Cleaning of Si wafer

    - Acetone bath in beaker, gently stirring in circles

    - Lift up the wafer while showering with Ethanol

    - Continue showering with Isopropanol

    - Continue showering with DI water

    - Dry with N_2

2. Dehydration

    - 200°C for 5 min

3. Plasma cleaner 3 min (50%O_2, 50%$power$)

4. Photoresist, spin coat

    - SU-8 5

    - 1000 rpm - 33sec - 300 rpm/sec

    - This gives a photoresist thickness of ~12μm

5. Pre Exposure Baking

    - Use your own clean 4" carrier wafer on the plate

    - Type: Soft baking (baking on flat plate)

    - Temp: 65°C

    - Time: 1 min

    - Increase temp to 95°C with wafer on plate

    - Temp: 95°C

    - Time: 4 min

    - Cool down: 3 min on plate

6. Control backside, clean with acetone if necessary

7. UV exposure

   - Type: MA6

   - Energy: 200 mJ

   - Method: Hard

   - Distance: 100 (This is only for alignment)

8. Post Exposure Baking

   - Use your own clean 4" carrier wafer on the plate

   - Type: Soft baking

   - Temp: 65°C

   - Time: 1 min

   - Increase temp to 95°C with wafer on plate

   - Temp: 95°C

   - Time: 2 min

   - Cool down: 3 min on plate

9. Development

   - Type: Dev-600

   - Time: 1 min development, water bath, N2, repeat 3 times

   - Isopropanol bath

   - N2

10. Dehydration

    - 200°C for 5 min

11. Profilometer: check height of photoresist pillars

12. Etching

- Type: ICP-RIE Cryo

- Time: 10 - 50 min

- Gas: SF_6 and O_2

- If the wafer gets black you produce nanowires. Reduce O_2 if you dont want that

- Make sure the whole wafers backside has a thin layer of heat enhancing oil before placing on carrier wafer

ICP-RIE CRYO RECIPE

Loop 4,5,6 and 7 for deeper etch.

1. HE Leak Check (STD) - 10s

2. Pump (STD) - 3m

3. N2 Purge (STD) - 2m

   - P = 40 mTorr

   - T = -120°C

   - N2 = 100 sccm

4. Pump to 1e-6 (STD)

5. Strike - 8s

   - P = 10 mTorr

   - T = -120°C

   - RF = 40W

   - ICP = 600W

   - O2 = 10 sccm

   - SF6 = 60 sccm

6. Etch - 10m

   - P = 10 mTorr

   - T = -120°C

   - RF = 6W

   - ICP = 600W

   - O2 = 10 sccm

   - SF6 = 60 sccm

7. N2 Purge - 3m

- N2 = 60 sccm

8. Loop (STD) 3x

  - N2 Purge

  - Pump

9. Pump to 1e-6 (STD)

C.7 PILLAR RECIPE G

1. Cleaning of Si wafer

   - Acetone bath in beaker, gently stirring in circles

   - Lift up the wafer while showering with Ethanol

   - Continue showering with Isopropanol

   - Continue showering with DI water

   - Dry with N_2

2. Dehydration

   - 200°C for 5 min

3. Plasma cleaner 3 min ($50\%O_2, 50\% power$)

4. Photoresist, spin coat

   - SU8-5

   - 3000 rpm - 40sec - 300 rpm/sec

   - This gives a photoresist thickness of $\sim 1 - 2\mu m$

5. Pre Exposure Baking

   - Use your own clean 4" carrier wafer on the plate

   - Type: Soft baking (baking on flat plate)

   - Temp: 65 degrees

   - Time: 1 min

   - Increase temp to 95 degrees with wafer on plate

   - Temp: 95 degrees

   - Time: 3 min

   - Cool down: 3 min on plate

6. Control backside, clean with acetone if necessary

7. UV exposure

   - Type: MA6

   - Energy: 200 mJ

   - Method: Hard

   - Distance: 100 (This is only for alignment)

8. Post Exposure Baking

   - Use your own clean 4" carrier wafer on the plate

   - Type: Soft baking

   - Temp: 65 degrees

   - Time: 1 min

   - Increase temp to 95 degrees with wafer on plate

   - Temp: 95 degrees

   - Time: 1 min

   - Cool down: 3 min on plate

9. Development

   - Type: mr-Dev 600

   - Time: 1 min development, water bath

   - Isopropanol bath

   - N2

10. Dehydration

    - 200°C for 5 min

11. Profilometer: check height of photoresist pillars

12. Etching

- Type: ICP-RIE Cryo

- Time: 10 - 50 min

- Gas: SF_6 and O_2

- If the wafer gets black you produce nanowires. Reduce O_2 if you dont want that

- Make sure the whole wafers backside has a thin layer of heat enhancing oil before placing on carrier wafer

ICP-RIE CRYO RECIPE

Loop 4,5,6 and 7 for deeper etch.

1. HE Leak Check (STD) - 10s

2. Pump (STD) - 3m

3. N2 Purge (STD) - 2m

   - P = 40 mTorr

   - T = -120 C

   - N2 = 100 sccm

4. Pump to 1e-6 (STD)

5. Strike - 8s

   - P = 10 mTorr

   - T = -120°C

   - RF = 40W

   - ICP = 600W

   - O2 = 10 sccm

   - SF6 = 60 sccm

6. Etch - 10m

   - P = 10 mTorr

   - T = -120°C

   - RF = 6W

   - ICP = 600W

   - O2 = 10 sccm

   - SF6 = 60 sccm

7. N2 Purge - 3m

- N2 = 60 sccm

8. Loop (STD) 3x

    - N2 Purge

    - Pump

9. Pump to 1e-6 (STD)

C.8 PILLAR RECIPE H

1. Cleaning of Si wafer

    - Acetone bath in beaker, gently stirring in circles

    - Lift up the wafer while showering with Ethanol

    - Continue showering with Isopropanol

    - Continue showering with DI water

    - Dry with N_2

2. Dehydration

    - 200°C for 5 min

3. Plasma cleaner 3 min ($50\%O_2, 50\%power$)

4. Photoresist, spin coat

    - SU-8 5

    - 3000 rpm - 40sec - 300 rpm/sec

    - This gives a photoresist thickness of $\sim 1 - 2\mu m$

5. Pre Exposure Baking

    - Use your own clean 4" carrier wafer on the plate

    - Type: Soft baking (baking on flat plate)

    - Temp: 65°C

    - Time: 1 min

    - Increase temp to 95°C with wafer on plate

    - Temp: 95°C

    - Time: 3 min

    - Cool down: 3 min on plate

6. Control backside, clean with acetone if necessary

7. UV exposure

    - Type: MA6

    - Energy: 200 mJ

    - Method: Hard

    - Distance: 100 (This is only for alignment)

8. Post Exposure Baking

    - Use your own clean 4" carrier wafer on the plate

    - Type: Soft baking

    - Temp: 65°C

    - Time: 1 min

    - Increase temp to 95°C with wafer on plate

    - Temp: 95°C

    - Time: 1 min

    - Cool down: 3 min on plate

9. Development

    - Type: mr-Dev 600

    - Time: 1 min development, water bath

    - Isopropanol bath

    - N_2

10. Profilometer: check height of photoresist pillars

11. Cleaning of Si wafer backside

    - Acetone bath in beaker, gently stirring in circles

    - Lift up the wafer while showering with Ethanol

- Continue showering with Isopropanol

- Continue showering with DI water

- Dry with N_2

12. Dehydration

- 200°C for 5 min

13. Etching

- Type: ICP-RIE Cryo

- Time: 10 - 50 min

- Gas: SF_6 and O_2

- If the wafer gets black, you produce nanowires. Reduce O_2 if you do not want that

- Make sure the whole wafers backside has a thin layer of heat enhancing oil before placing on carrier wafer

ICP-RIE CRYO RECIPE

Loop 4,5,6 and 7 for deeper etch.

1. He Leak Check (STD) - 10s

2. Pump (STD) - 3m

3. N2 Purge (STD) - 2m

   - P = 40 mTorr

   - T = -120 C

   - N2 = 100 sccm

4. Pump to 1e-6 (STD)

5. Strike - 8s

   - P = 10 mTorr

   - T = -120°C

   - RF = 40W

   - ICP = 600W

   - O2 = 10 sccm

   - SF6 = 60 sccm

6. Etch - 10m

   - P = 10 mTorr

   - T = -120°C

   - RF = 6W

   - ICP = 600W

   - O2 = 10 sccm

   - SF6 = 60 sccm

7. N2 Purge - 3m

- N2 = 60 sccm

8. Loop (STD) 3x

    - N2 Purge

    - Pump

9. Pump to 1e-6 (STD)

C.9 ICP-RIE CRYO REMOVE SU-8 RECIPE

1. He Leak Check (STD) - 10s

2. Pump (STD) - 3m

3. N_2 Purge (STD)

   - t = 2 min

   - P = 40 mTorr

   - T = 20°C

   - N_2 = 100 sccm

4. Pump to 1e-6 (STD)

5. Etch

   - t = 30 min

   - P = 10 mTorr

   - T = 20°C

   - CCP = 200W

   - ICP = 1500W

   - He = 0 sccm

   - O_2 = 40 sccm

6. Loop (STD) 3x

   - N_2 Purge

   - Pump

7. Pump to 1e-6 (STD)

C.10   ICP-RIE CRYO CONE RECIPE 1.0

1. He Leak Check (STD) - 10s

2. Pump (STD) - 3m

3. N_2 Purge (STD)

   - $t = 2$ min

   - $P = 40$ mTorr

   - $T = -50°C$

   - $N_2 = 100$ sccm

4. Pump to 1e-6 (STD)

5. Strike

   - $t = 8$ sec

   - $P = 75$ mTorr

   - $T = -50°C$

   - $CCP = 40$W

   - $ICP = 500$W

   - $O_2 = 17.5$ sccm

   - $SF_6 = 100$ sccm

6. Etch

   - $t = 30$ min

   - $P = 75$ mTorr

   - $T = -50°C$

   - $CCP = 20$W

   - $ICP = 500$W

- O_2 = 17.5 sccm

- SF_6 = 100 sccm

7. Loop (STD) 3x

    - N_2 Purge

    - Pump

8. Pump to 1e-6 (STD)

C.11 ICP-RIE CRYO CONE RECIPE 2.0

1. HE Leak Check (STD) - 10s

2. Pump (STD) - 3m

3. N2 Purge (STD) - 2m

   - P = 40 mTorr

   - T = -50°C

   - N2 = 100 sccm

4. Pump to 1e-6 (STD)

5. Strike - 8s

   - P = 51 mTorr

   - T = -50°C

   - RF = 20W

   - ICP = 500W

   - O2 = 17.5 sccm

   - SF6 = 100 sccm

6. Etch Pressure - Loop 12x

   - P = +2 mTorr

   - T = -50°C

   - t = 5 sec

   - RF = 20W

   - ICP = 500W

   - O2 = 17.5 sccm

   - SF6 = 100 sccm

7. Etch - 30m

- P = 75 mTorr

- T = -50°C

- RF = 20W

- ICP = 500W

- O2 = 17.5 sccm

- SF6 = 100 sccm

8. Loop (STD) 3x

- N2 Purge

- Pump

9. Pump to 1e-6 (STD)

C.12 ICP-RIE CRYO CNW RECIPE

1. He Leak Check (STD) - 10s

2. Pump (STD) - 3m

3. N_2 Purge (STD)

   - $t = 2$ min

   - $P = 40$ mTorr

   - $T = 20°C$

   - $N_2 = 100$ sccm

4. Pump to 1e-6 (STD)

5. Strike

   - $t = 8$ sec

   - $P = 50$ mTorr

   - $T = 20°C$

   - $CCP = 40W$

   - $ICP = 300W$

   - $O_2 = 100$ sccm

6. Etch

   - $t = 30$ min

   - $P = 85$ mTorr

   - $T = 20°C$

   - $CCP = 40W$

   - $ICP = 300W$

   - $O_2 = 100$ sccm

7. Loop (STD) 3x

   - N_2 Purge

   - Pump

8. Pump to 1e-6 (STD)

C.13 ICP-RIE CRYO CONE BLACK SILICON RECIPE

1. He Leak Check (STD) - 10s

2. Pump (STD) - 3m

3. N_2 Purge (STD)

   - t = 2 min

   - P = 40 mTorr

   - T = -120°C

   - N_2 = 100 sccm

4. Pump to 1e-6 (STD)

5. Strike

   - t = 8 sec

   - P = 75 mTorr

   - T = -120°C

   - CCP = 40W

   - ICP = 500W

   - O_2 = 17.5 sccm

   - SF_6 = 100 sccm

6. Etch

   - t = 10 min

   - P = 75 mTorr

   - T = -120°C

   - CCP = 20W

   - ICP = 500W

- O_2 = 17.5 sccm

- SF_6 = 100 sccm

7. Loop (STD) 3x

    - N_2 Purge

    - Pump

8. Pump to 1e-6 (STD)
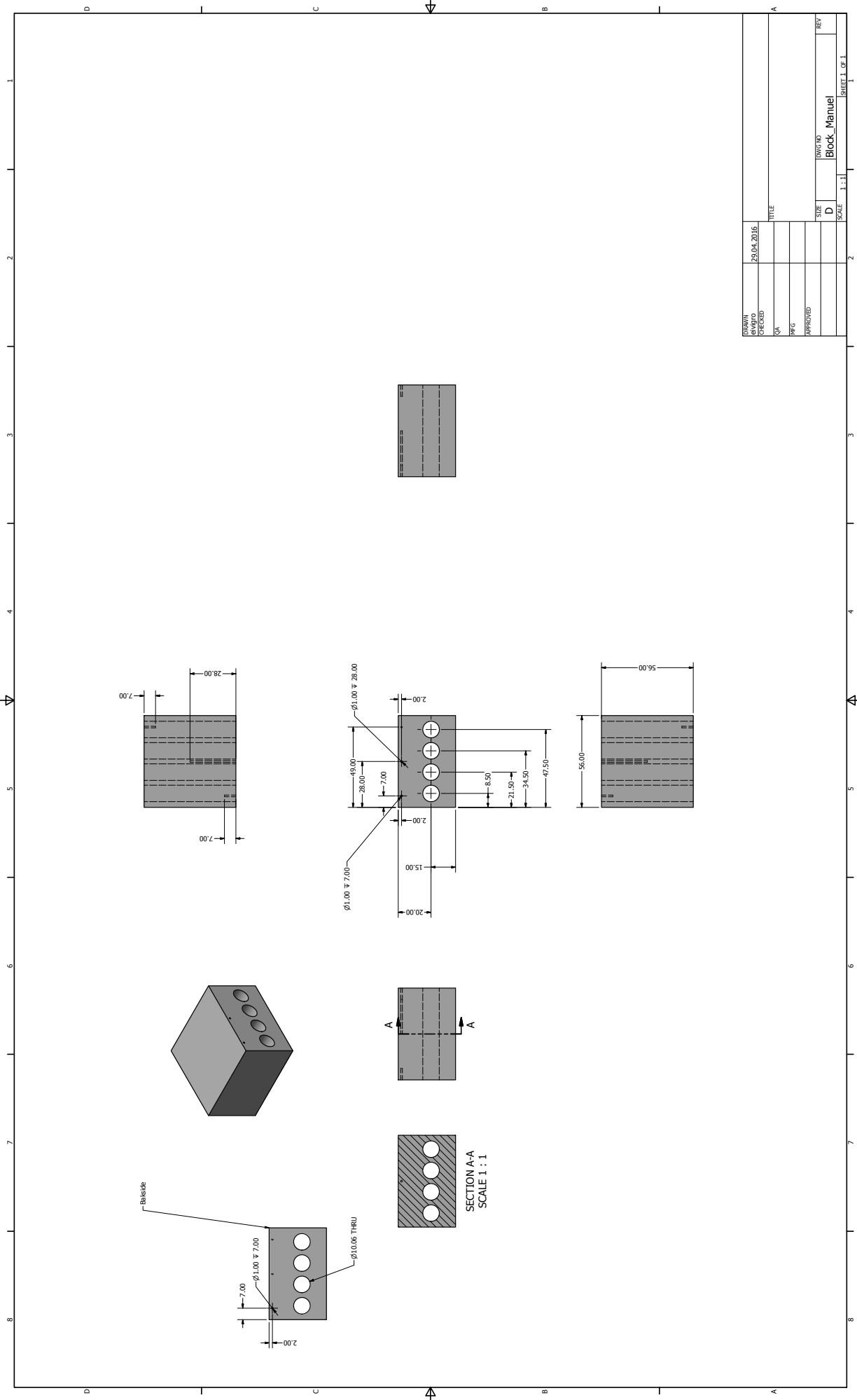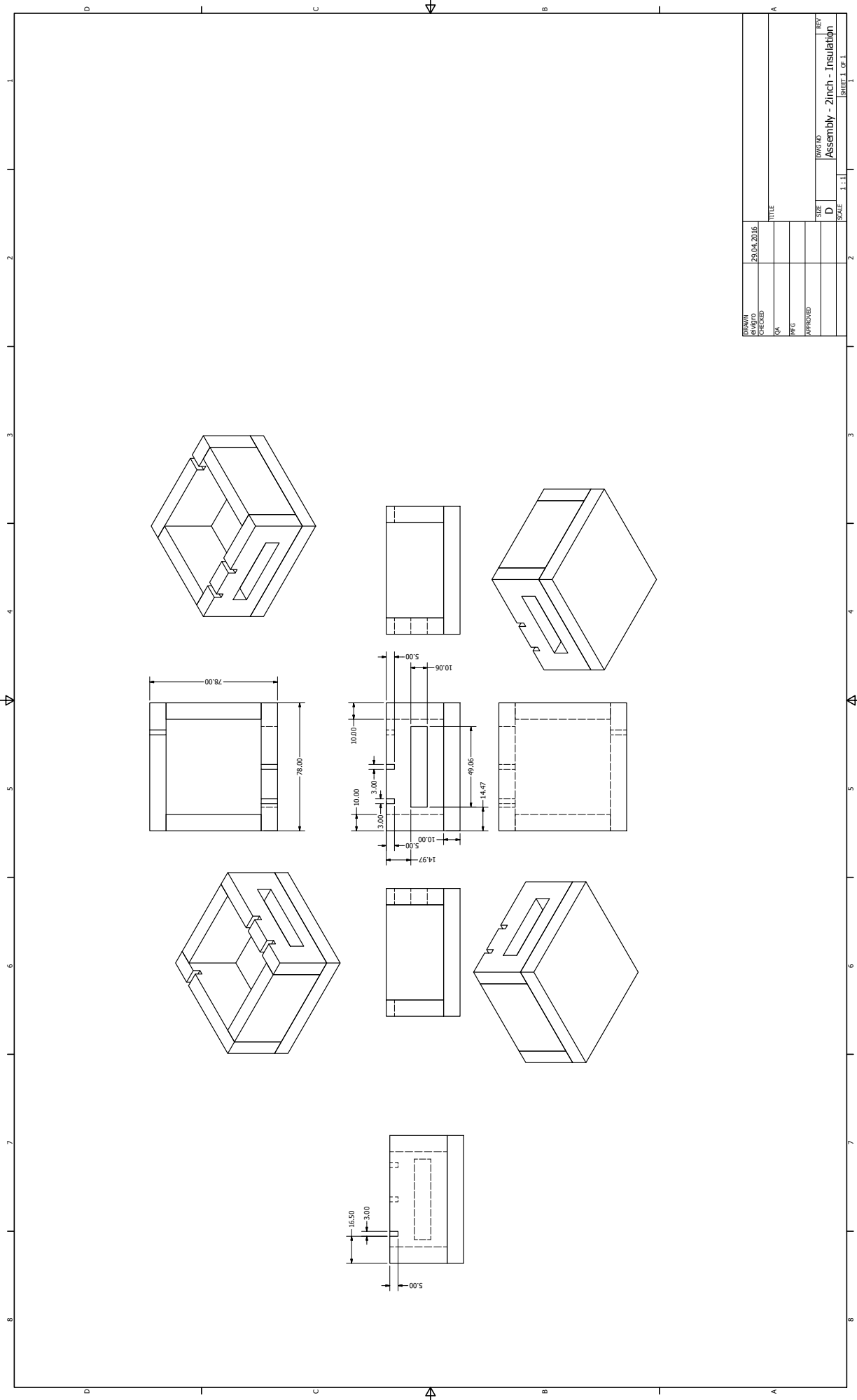
D.   Drawings

90.18
14.94
90.99
73.41
15.22
31.61
89.82
73.41
31.61
15.22
73.34
90.18
14.83
31.64
31.64

Ø3.00 � 6.00

105.00
27.00
52.50
105.00
27.00

M3x0.5 - 6H

3.00
Ø3.00
105.00
105.00
72.00
85.00
98.00
52.50
33.00
46.00
59.00
20.00
7.00
27.50
2.00

40.00
27.50
2.00
Ø1.00
Ø1.00
29.50
2.00
Ø10.06

DWG NO

TITLE

31.03.2016

DRAWN
elvigro
CHECKED
QA
MFG
APPROVED

SIZE
D

SCALE
1 : 1

127.00

10.00

5.04

6.51

6.47

40.00

12.00

39.00

61.00

39.00

3.00

3.00

126.99

3.00

5.00

103.00

61.00

3.00

39.00

12.00

10.00

12.00

5.00

107.00

SECTION A-A
SCALE 1 : 1

Bakside

Ø1.00 ⊽ 7.00

Ø10.06 THRU

7.00

2.00

28.00

7.00

7.00

Ø1.00 ⊽ 28.00

2.00

Ø1.00 ⊽ 7.00

49.00

28.00

7.00

8.50

21.50

34.50

47.50

15.00

20.00

2.00

56.00

56.00

A

A

78.00

78.00

5.00
10.06
10.00
49.06
14.47
10.00
3.00
3.00
5.00
10.00
14.97

16.50
3.00
5.00

E.   Fotomask

Figure E.1: 4" photomask used in this work. Drawings from CleWin. W = width/diameter, P = pitch, SQ = square pattern, geometry = circles.

F.   Datasheets

PRODUCT DATA SHEET

BAGGES SFC-2

RoHSII: The material is in compliance with
EU directive 2011/65/EU (RoHS II)
Components: Fiber/cement
Color: Grey

Mechanical Properties		Testmethods	Value	Unit
Flexural strength at RT		BS 2782	30	MPa
Flexural strength at 350°C/500°C		BS 2782	16/13	MPa
Flexural strength at 700°C			13	MPa
Modulus of elasticity		-	-	MPa
Compressive strength at RT/350°C		BS 2782	90/38	MPa
Compressive strength at 500/700°C			31/29	MPa
Izod impact strength, parallel at RT/700°C		BS 2782	4/2.4	kJ/m²
Linear shrink at 350°C		BS 2782	0,36	%
Tensile strength		-	-	MPa
Electrical properties				
Electric strength in oil at 90°C		BS2782	2.1	kV/mm
Electric strength in oil at 90°C		-	-	kV/25mm
Permittivity 50 Hz		-	-	
Permittivity 1 MHz		-	-	
Dissipation factor 50 Hz		-	-	
Insulation resistance after immersion in water		-	-	M Ω
Physical and thermal properties				
Temperature continuous		BS 2782	700	°C
Flammability		Not flammable	-	
Density		BS 2782	1.6	g/cm3
Water absorption		BS 2782	15	%

The data mentioned in this data sheet is after our knowledge correct, but we reserve the right to make changes without notice.

Rev. 11/2015

3M

Fluorinert™
Electronic Liquid
FC-72

Introduction

3M™ Fluorinert™ Electronic Liquid FC-72 is a clear, colorless, fully-fluorinated liquid. Like other Fluorinert electronic liquids, Fluorinert liquid FC-72 is thermally and chemically stable, compatible with sensitive materials, nonflammable, practically non-toxic and leaves essentially no residue upon evaporation. This unique combination of properties makes Fluorinert liquid FC-72 ideal for many electronics applications, including quality and reliability testing.

Fluorinert liquid FC-72 conforms to Military Specification 883 as a detector fluid in a vacuum/pressure vessel used in gross leak testing. Its inert nature makes FC-72 liquid a useful reaction medium.

Physical Properties

Not for specification purposes

All values determined at 25°C unless otherwise specified

Properties	FC-72
Appearance	Clear, colorless
Average Molecular Weight	338
Boiling Point (1 atm)	56°C
Pour Point	-90°C
Estimated Critical Temperature	449 K
Estimated Critical Pressure	1.83×10^6 pascals
Vapor Pressure	30.9×10^3 pascals
Latent Heat of Vaporization (at normal boiling point)	88 J/g
Liquid Density	1680 kg/m^3
Kinematic Viscosity	0.38 centistokes
Absolute Viscosity	0.64 centipoise
Liquid Specific Heat	1100 J kg^{-1} C^{-1}
Liquid Thermal Conductivity	0.057 W m^{-1}°C^{-1}
Coefficient of Expansion	0.00156 °C^{-1}
Surface Tension	10 dynes/cm
Refractive Index	1.251
Water Solubility	10 ppmw
Solubility in Water	<5 ppmw
Ozone Depletion Potential	0

3M™ Fluorinert™ Electronic Liquid FC-72 Electrical Properties

Properties	FC-72
Dielectric Strength	38 kV, 0.1" gap
Dielectric Constant	1.75
Electrical Resistivity	1.0×10^{15} ohm cm

Heat Transfer Properties

The following formulas can be used to calculate the specific heat, thermal conductivity and density of 3M™ Fluorinert™ Electronic Liquid FC-72 at various temperatures.
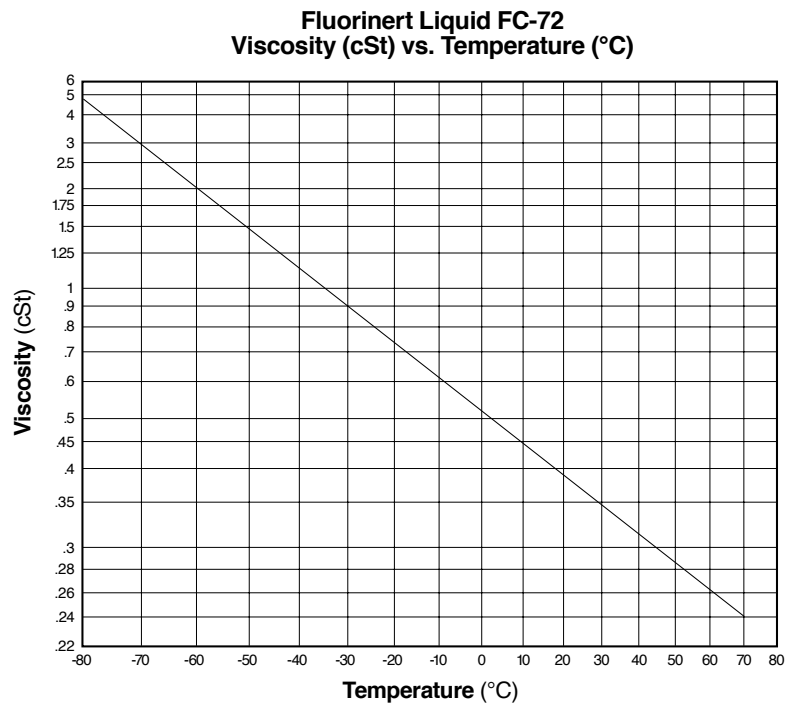
Specific Heat $(J \, kg^{-1} \, C^{-1}) = 1014 + 1.554 \, (T, °C)$

Thermal Conductivity $(W \, m^{-1} \, °C^{-1}) = 0.060 - 0.00011 \, (T, °C)$

Density $(kg/m^3) = 1740 - 2.61 \, (T, °C)$

$Log_{10}(Vapor Pressure (pascals)) = 9.729 - (1562/(T, K))$

The following graph can be used to determine the viscosity of Fluorinert liquid FC-72 over the indicated temperature range.

Fluorinert Liquid FC-72
Viscosity (cSt) vs. Temperature (°C)

2

3M™ Fluorinert™ Electronic Liquid FC-72 Materials Compatibility

3M™ Fluorinert™ Electronic Liquid FC-72 is compatible with most metals, plastics and elastomers.

Toxicity Profile

Fluorinert liquid FC-72 is non-irritating to the eyes and skin, and is practically non-toxic orally. The product also demonstrates very low acute and sub-chronic inhalation toxicity. It is not a mutagen (ames) or a cardiac sensitizer. A Material Safety Data Sheet is available upon request.

Safety and Handling

Before using this product, please read the current product Material Safety Data Sheet (available through your 3M sales or technical service representative) and the precautionary statement on the product package. Follow all applicable precautions and directions. Fluorinert liquid FC-72 is nonflammable, and is highly resistant to thermal breakdown and hydrolysis in storage and during use. Recommended handling procedures are given in the Material Safety Data Sheet.

Environmental Properties

Fluorinert liquid FC-72 has zero ozone depletion potential. The material is exempt from the U.S. EPA and most State definitions of a volatile organic compound (VOC), and does not contribute to ground-level smog formation.

Fluorinert liquid FC-72, a perfluorocarbon (PFC), has a high global warming potential and a long atmospheric lifetime. As such, it should be carefully managed so as to minimize emissions.

3M recommends that users of FC-72 liquid further limit emissions by employing good conservation practices, and by implementing recovery, recycling and/or proper disposal procedures. 3M offers a program for used fluid return.

Environmental Policy

3M will recognize and exercise its responsibility to:

• prevent pollution at the source wherever and whenever possible

• develop products that will have a minimal effect on the environment

• conserve natural resources through the use of reclamation and other appropriate methods

• assure that its facilities and products meet and sustain the regulations of all Federal, State and local environmental agencies

• assist, wherever possible, governmental agencies and other official organizations engaged in environmental activities

3M™ Fluorinert™ Electronic Liquid FC-72 Used Fluid Return Program

3M offers a program for free pickup and return of used 3M Specialty Materials in the U.S. through Safety-Kleen Corporation. A pre-negotiated handling agreement between users and this service provider offers users broad protection against future liability for used 3M product. The fluid return program is covered by independent third-party financial and environmental audits of treatment, storage and disposal facilities. Necessary documentation is provided. A minimum of 30 gallons of used 3M Specialty Materials is required for participation in this free program.

Safety-Kleen Corporation has a network of 156 branch service centers in the U.S. This large fleet will provide timely, economical fluid disposal service.

For additional information on the 3M Used Fluid Return Program, contact Safety-Kleen Corporation at this toll-free line: 1.888.932.2731.

Resources

3M™ Fluorinert™ Electronic Liquid FC-72 customers are supported by global sales, technical and customer sales resources, with fully staffed technical service laboratories in the U.S., Europe, Japan, Latin America and Southeast Asia. Users benefit from 3M's broad technology base and continuing attention to product development, performance, safety and environmental issues.

For other 3M global offices and additional information on Fluorinert electronic liquid FC-72 in the U.S., call 3M Performance Materials, 800.833.5045, or visit our web site at: www.3m.com/fluids

3M

Specialty Materials

3M Center, Building 223-6S-04
St. Paul, MN 55144-1000

Issued: 05/00   © 2000 3M IPC   98-0212-2308-0 (HB)